CDF/ANAL/BOTTOM/CDFR/10628
Version 1.4 – September 18, 2011

Measurement of Upsilon Decay Angular Distributions

Matthew Jones

Purdue University

1 Introduction

In the rest frame of the $\Upsilon \to \mu^+\mu^-$ decay, the angular distribution of the μ^+ can be expressed

$$\frac{d\Gamma}{d\Omega} \propto 1 + \lambda_\theta \cos^2\theta + \lambda_\varphi \sin^2\theta \cos 2\varphi + \lambda_{\theta\varphi} \sin 2\theta \cos\varphi + \lambda_\varphi^\perp \sin^2\theta \sin 2\varphi + \lambda_{\theta\varphi}^\perp \sin 2\theta \sin\varphi \tag{1}$$

which reduces to

$$\frac{d\Gamma}{d\Omega} \propto 1 + \lambda_\theta \cos^2\theta + \lambda_\varphi \sin^2\theta \cos 2\varphi + \lambda_{\theta\varphi} \sin 2\theta \cos\varphi \tag{2}$$

when combining the angular interval (θ, φ) with $(\theta, -\varphi)$ and (θ, φ) with $(\pi - \theta, \pi - \varphi)$. The polar angles, θ and φ are defined in terms of the coordinate axes of a particular reference frame which is, in general, not uniquely defined. Popular choices are the S-channel helicity frame and the Collins-Soper frame, but others like the Gottfried-Jackson frame could also be used.

Previous polarization analyses carried out at CDF have attempted to measure λ_θ, but this has only been performed in the S-channel helicity frame. In addition to measuring the cross section, the goal of this analysis is to measure λ_θ, λ_φ and $\lambda_{\theta\varphi}$ simultaneously in both the S-channel helicity frame and the Collins-Soper frame, which provides the ability to quantify the self-consistency of the results.

The underlying angular distribution is determined by fitting the observed angular distribution to the parametrization in Equation 2 multiplied by the detector acceptance, which is calculated as a function of $(\cos\theta, \varphi)$ using an un-polarized sample of $\Upsilon(nS)$ decays processed using the full detector simulation and with trigger and reconstruction efficiencies that were measured and parameterized using independent control samples.

2 Data samples and candidate selection

This analysis uses data recorded with the UPSILON_CMUP_CMU and UPSILON_CMUP_CMX trigger paths. Most of the data was recorded using DPS versions of these triggers, but un-prescaled versions are available from trigger tables prior to `PHYSICS_3_07_v-1`. The reconstructed events are selected from the `jbmm0d`, `jbmm0h`, `jbmm0i`, `jbmm0j`, `jbmm0k` and `jbmm0m` data sets and include all data recorded in periods 0 through 28. This corresponds to an integrated luminosity of 6726 pb^{-1}, although the dynamic prescales applied to the trigger paths reduces the effective integrated luminosity to about 70% of this. Using the complete CDF dataset, which up to period 36 contains

Table	first run	$\int \mathcal{L}dt$ [pb^{-1}]	comments
PHYSICS_1_01_v-4	141544	0	initial instance, no L2
PHYSICS_2_05_v-1	182843	246	L2 CMUP/CMU XFT p_T 3.04/1.52 GeV/c
PHYSICS_3_06_v-1	202771	681	$\lvert\Delta x_{\mathrm{CMP}}\rvert < 40$ cm
PHYSICS_3_07_v-1	202972	685	DPS 10 at L2
PHYSICS_4_02_v-3	238981	1662	DPS 40 at L2
PHYSICS_5_03_v-1	276600	4003	LUMI_280 at L1

Table 1: Trigger table changes for the CMUP+CMU trigger.

9695 pb^{-1}, may result in approximately 7000 pb^{-1} of equivalent luminosity. Good runs were selected using the `goodrun_em_mu_nosi_cmxignored` file prepared for version 34 of the good run list, which excludes the period of data taken with compromised COT gain.

2.1 Trigger requirements

Initially introduced with the `PHYSICS_1_01` trigger table, the CMUP+CMU trigger required two low-p_T (1.5 GeV/c) CMU stubs matched to XFT tracks with a minimum p_T threshold of 1.5 GeV/c. At that time, there was no level 2 trigger selection, but the level 3 trigger imposed the 3 GeV/c threshold on the CMU muon and the 4 GeV/c threshold on the muon in CMP. Furthermore, the CMU muon was required to have $|\Delta x_{\mathrm{CMU}}| < 30$ cm, while the muon in CMP was required to have $|\Delta x_{\mathrm{CMU}}| < 15$ cm and $|\Delta x_{\mathrm{CMP}}| < 20$ cm. Finally, in level 3, the two muons were required to have opposite charge and to have invariant mass between 8 and 12 GeV/c^2. Table 1 summarizes the major changes in the evolution of the CMUP+CMU trigger with subsequent trigger tables.

2.2 Off-line event selection

The events analyzed are required to be in the expected trigger path by checking the Level 3 trigger bits. The runs analyzed are required to be in the `goodrun_em_mu_nosi_cmxignored` good run list and to have equivalent integrated luminosity estimates obtained from the `DFCLuminosityTool` utility.

2.3 Candidate selection

The $\Upsilon(nS) \to \mu^+\mu^-$ candidates were selected using criteria similar to those used in the CDF $B_s \to \mu^+\mu^-$ search[1]. First, a loose $\Upsilon \to \mu^+\mu^-$ candidate selection was performed using CharmMods to select oppositely charged muon candidates. This selection imposed the following requirements on the muon and di-muon candidates:

- Tracks associated with a `CdfMuon` object
- At least 25 hits on axial COT super-layers
- At least 25 hits on stereo COT super-layers
- $p_T(\mu) > 1$ GeV/c
- $|\eta| < 2$
- $p_T(\mu^+) + p_T(\mu^-) > 3$ GeV/c
- $8 < m(\mu^+\mu^-) < 12$ GeV/c^2
- $|z_0(\mu^+) - z_0(\mu^-)| < 8$ cm

- Successful vertex fit

The candidates selected for the cross section and spin alignment analysis are obtained by imposing the following additional requirements:

- $8.4 < m(\mu^+\mu^-) < 11.6$ GeV/c^2
- $|z_0(\mu^\pm)| < 60$ cm
- $|z_0(\mu^+) - z_0(\mu^-)| < 5$ cm
- $\Delta\phi_0 > 2.25°$
- $|z(R_{SL})| > 1.5$ cm at radius of axial super-layers
- $|z(R = 136 \text{ cm})| < 155$ cm
- $\Delta\phi_{SL6} > 1.5°$
- muon candidates must be derived from COT tracks
- muon candidates matched with XFT track based on $\delta 1/C$ and $\delta\phi_6$.

In both the `UPSILON_CMUP_CMU` and `UPSILON_CMUP_CMX` trigger paths, the candidates were required to consist of one CMUP muon that satisfied:

- $|\Delta x_{\text{CMU}}| < 15$ cm
- $|\Delta x_{\text{CMP}}| < 40$ cm (< 20 cm prior to `PHYSICS_3_06_v-1`)
- $p_T(\mu^\mp_{\text{CMUP}}) > 4.05$ GeV/c

and, depending on which of the two trigger paths was used to select the event, an additional CMU muon that satisfied

- $|\Delta x_{\text{CMU}}| < 30$ cm
- $p_T(\mu^\pm_{\text{CMU}}) > 3.05$ GeV/c

or a CMX muon that satisfied

- $|\Delta x_{CMX}| < 50$ cm
- $p_T(\mu^\mp_{\text{CMX}}) > 3.05$ GeV/c.

The p_T thresholds were increased slightly from the nominal values of 3 and 4 GeV/c used in the Level 3 triggers.

2.4 Restricted detector acceptance

There are two small regions in CMU that are not instrumented:

- 1/3 of wedge 8W
- $z > 200$ cm of wedge 6E.

and muons in these regions are vetoed. In fact, only one third of wedge 6E has been shortened, but the Monte Carlo treats all chambers in this wedge as being short, so the data is treated likewise.

Muons in the following regions of CMX were dropped from further analysis:

- wedges 15W and 20W
- wedges 5E and 6E (solenoid cryo stuff)
- wedges 15-20 prior to run 227704 (mini-skirts)
- wedges 5W and 6W prior to run 233112 (keystone)
- wedge 14W for runs numbers between 190695 and 210009.

In general, however, the fiducial acceptance of CMX remains unchanged after run 233112, which roughly corresponds to the first 1440 pb^{-1} of integrated luminosity.

3 Trigger and reconstruction efficiency

Monte Carlo samples are primarily used to calculate the detector acceptance. $\Upsilon(nS) \rightarrow \mu^+\mu^-$ decays are generated with a distribution of p_T and rapidity tuned to match the data and are analyzed separately in restricted ranges of the candidate's p_T and rapidity. In addition, the generated events are required to have a z-vertex that satisfies $|z| < 60$ cm. Simulated events that are classified as being within the detector acceptance are those that are reconstructed as `CdfMuon` objects and are not located in regions of CMU and CMX identified as inefficient or are otherwise excluded from analysis in data. Furthermore, the `CdfTrack` objects associated with the muon candidates must satisfy the XFT fiducial requirements. The simulated muons must also have reconstructed p_T that exceeds the thresholds imposed by level 3 trigger and the pair must satisfy $\Delta\phi_0$ and $\Delta\phi_{SL6}$ requirements to ensure that they would pass the Level-1 di-muon trigger.

The $\Upsilon(nS)$ production cross section is calculated from the usual expression

$$\frac{d\sigma}{dp_T dy} = \frac{N_\Upsilon}{\mathcal{A}\epsilon \int \mathcal{L}dt \Delta p_T \Delta y} \tag{3}$$

in which N_Υ is the fitted Υ yield, determined from the sideband subtracted di-muon invariant mass distribution, $\mathcal{A}$ is the detector acceptance, ϵ is the efficiency for reconstructing Υ decays that are within the detector acceptance, $\int \mathcal{L}dt$ is the integrated luminosity of the data sample analyzed, and Δp_T and Δy are the widths of the transverse momentum and rapidity intervals. The acceptance depends on the $\Upsilon(nS)$ polarization since this influences the angular distribution of the final state muons.

In Equation 3, the product $\mathcal{A}\epsilon$ represents the probability that an $\Upsilon(nS)$, produced with p_T and y in the specified range, will decay to $\mu^+\mu^-$ which then satisfy the trigger and reconstruction criteria. This product can be expressed in terms of the joint probability for the final state to fulfill the specific criteria required by the analysis:

$$\mathcal{A}\epsilon = \mathcal{A}(\mu^+\mu^-)\epsilon_{vtx}\epsilon(\mu^+)\epsilon(\mu^-) \tag{4}$$

The acceptance $\mathcal{A}(\mu^+\mu^-)$ defines the probability that the decay products satisfy the fiducial requirements of the tracker and the muon chambers, ϵ_{vtx} is the efficiency for the event to satisfy requirements imposed on the primary vertex and $\epsilon(\mu^+)$ and $\epsilon(\mu^-)$ are the for the two muons to satisfy the trigger and reconstruction criteria.

In practice, the muons reconstructed in the Monte Carlo are required to be `CdfMuon` objects. Thus, the acceptance calculated by counting simulated events that contain reconstructed Υ decays is

$$\mathcal{A}'(\mu^+\mu^-) = \mathcal{A}(\mu^+\mu^-)P(\texttt{CdfMuon}|\text{fiducial } \mu^+)P(\texttt{CdfMuon}|\text{fiducial } \mu^-) \tag{5}$$

where

$$P(\texttt{CdfMuon}|\text{fiducial } \mu^\pm) \approx P(\texttt{CdfMuon}|\text{fiducial track})P(\text{track}|\text{fiducial } \mu^\pm) \tag{6}$$

Because the signal in the data is also reconstructed from `CdfMuon` objects, the acceptance is calculated using

$$\mathcal{A}(\mu^+\mu^-) = \mathcal{A}'(\mu^+\mu^-)S(\mu^+)S(\mu^-) \tag{7}$$

where $S(\mu^\pm)$ is a scale factor define by

$$S(\mu^\pm) = \frac{P_{\rm data}(\texttt{CdfMuon}|\text{fiducial track})P_{\rm data}(\text{track}|\text{fiducial }\mu^\pm)}{P_{\rm MC}(\texttt{CdfMuon}|\text{fiducial track})P_{\rm MC}(\text{track}|\text{fiducial }\mu^\pm)} \tag{8}$$

3.1 Muon scale factors

In this analysis we can use the track reconstruction efficiency determined from hit embedding[4]:

$$P_{\rm data}(\text{track}|\text{fiducial }\mu^\pm) = 99.61 \pm 0.02\text{ (stat.)}^{+0.34}_{-0.91}\text{ (syst.) }\% \tag{9}$$

which is a constant when defined for tracks with $p_T > 1.5$ GeV/c that are fiducial in all 8 layers of the COT. The probability that a `CdfTrack` that is fiducial in the muon chambers is reconstructed as a `CdfMuon` object is measured in data using the μ+SVT trigger sample which provides a relatively high statistics sample of $J/\psi \to \mu^+\mu^-$ for which one muon leg is unbiased by any muon trigger or identification requirements. However, to pass the SVT trigger, the unbiased leg is required to satisfy the XFT trigger at level 1 so we actually measure $P_{\rm data}(\texttt{CdfMuon}|\text{fiducial track} \cap \text{XFT match})$ from which we can calculate

$$P_{\rm data}(\texttt{CdfMuon}|\text{fiducial track}) = \frac{P_{\rm data}(\text{CdfMuon}|\text{fiducial track} \cap \text{XFT match})}{P_{\rm data}(\text{XFT match}|\text{fiducial track})} \tag{10}$$

The numerator is calculated by selecting J/ψ candidates from the `B_SEMI_CMUP4_TRACK2_D120` trigger path, requiring one leg to be fiducial in CMUP and have $p_T > 4$ GeV/c. Figure 1 shows the $J/\psi \to \mu^+\mu^-$ signal yields from events with unbiased muons that are fiducial in CMU or CMX which either are, or are not associated with muon stubs in CMU or CMX. Assuming that the efficiency plateaus for $p_T > 3$ GeV/c, the fitted J/ψ yields give

$$P_{\rm data}(\text{CdfMuon}|\text{fiducial track} \cap \text{XFT match}) = \begin{cases} 0.9562 \pm 0.0035 & \text{CMU} \\ 0.9094 \pm 0.0118 & \text{CMX} \end{cases} \tag{11}$$

The denominator in Equation 10 is measured using the unbiased sample of tracks provided by the kaon in $B^\pm \to J/\psi K^\pm$ decays reconstructed in the `jpmm` dataset. The $J/\psi \to \mu^+\mu^-$ candidates are required to satisfy trigger criteria and to have a 2D decay length significance exceeding 5σ. The $J/\psi K^\pm$ candidates are required to have $3.050 < m(\mu^+\mu^-) < 3.135$ GeV/c^2. Kaon candidates are selected from the `defTracks` collection and are only required to satisfy the XFT fiducial cuts. Figure 2 shows the invariant mass distribution of candidates that are matched or fail to be matched with XFT tracks. The XFT efficiency, calculated from the measured $B^\pm$ signal yields in each case, is

$$P_{\rm data}(\text{XFT match}|\text{fiducial track}) = 0.9648 \pm 0.0039. \tag{12}$$

From Equations 9, 11 and 12, along with

$$P_{\rm MC}(\texttt{CdfMuon}|\text{fiducialtrack}) = \begin{cases} 0.983758 & \text{CMU} \\ 0.972705 & \text{CMX} \end{cases} \tag{13}$$

$$P_{\rm MC}(\text{track}|\text{fiducial }\mu^\pm) = 0.999111 \tag{14}$$

we obtain the scale factors:

$$S(\mu) = \begin{cases} 1.0044^{+0.0066}_{-0.0108} & \text{CMU} \\ 0.9661^{+0.0131}_{-0.0155} & \text{CMX} \end{cases} \tag{15}$$

where the asymmetric error is due to the systematic uncertainties in the track reconstruction efficiency.

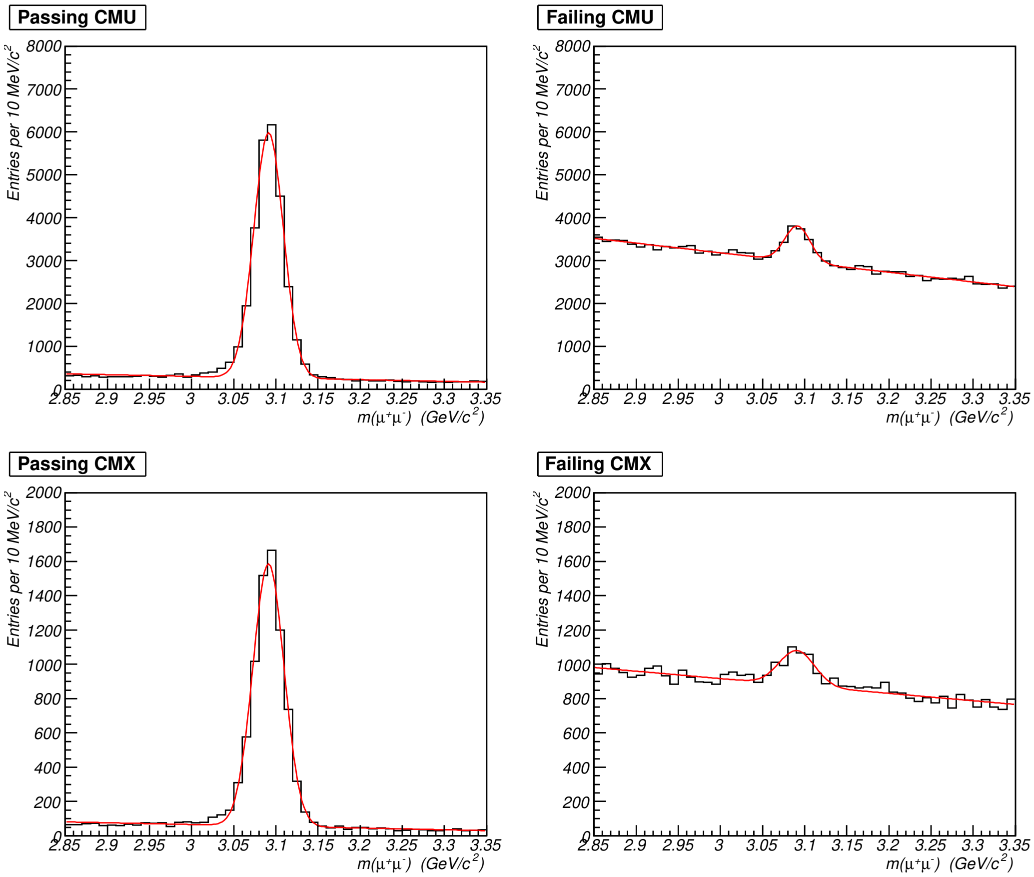

Figure 1: Fitted $J/\psi \to \mu^+\mu^-$ yields for muons fiducial in CMU (top) and in CMX (bottom).

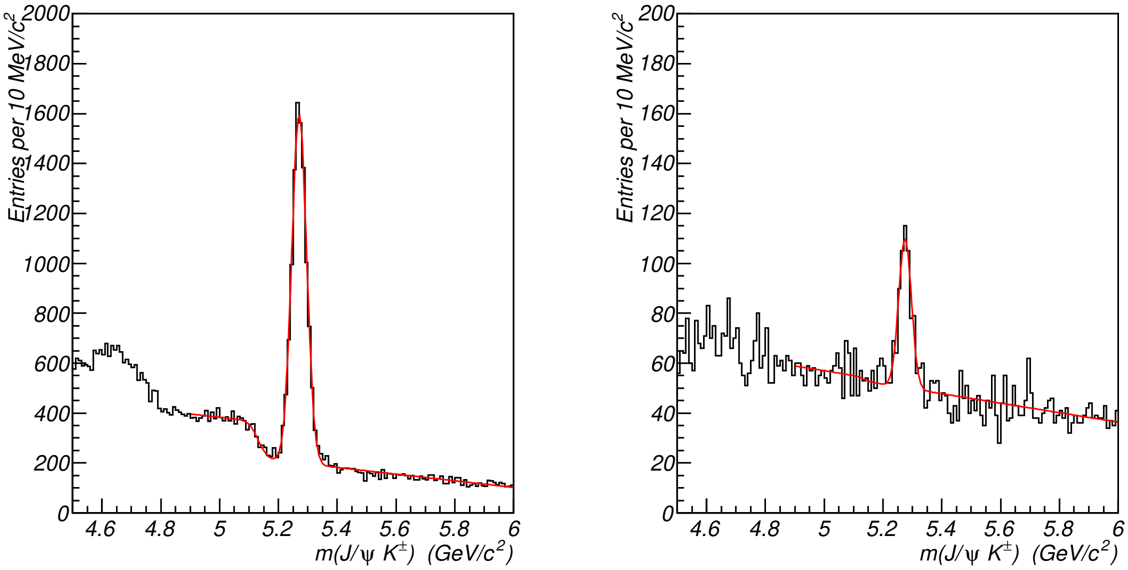

Figure 2: Invariant mass distribution of $J/\psi K^{\pm}$ candidates obtained from a triggered $J/\psi \to \mu^+\mu^-$ candidate and an unbiased track that is either matched (left) or not matched (right) with an XFT track.

3.2 Muon quality cuts

A reduction in di-muon backgrounds can be obtained by imposing requirements on the quality of the match between the track and the muon stub. The attempt to obtain a p_T independent parametrization of the match quality in terms of a χ^2 variable[5] was used in this analysis, but the implementation was found to have an efficiency that did vary as a function of p_T. The variation in the efficiency when applied to CMU and CMX muons was measured as a function of p_T using the J/ψ signal in the $\mu + SVT$ sample. Because the Level 3 trigger only imposes loose cuts on Δx, we also measure the relative efficiency for muons from $\Upsilon(nS) \to \mu^+\mu^-$ to satisfy the $\chi^2 < 9$ requirement. Figure 3 shows the efficiencies measured in this way.

It was found that although the efficiencies measured using the Υ sample and the μ+SVT sample were in reasonable agreement for CMX, they were significantly different in CMU. The cause of this disagreement is not understood, but because it is the relative Υ efficiency that is relevant in this analysis, we use do not use the CMU efficiency measured μ+SVT when deriving a p_T-dependent parameterization. The efficiencies were fit to the emperical forms

$$\epsilon(\chi^2 < 9) = \begin{cases} a + be^{-cp_T} & \text{CMU} \\ a + bp_T & \text{CMX} \end{cases} \tag{16}$$

as shown in Figure 3.

3.3 Vertex cuts

Restrictions on the z-vertex of di-muon candidates are applied to the generator level muons from which the detector acceptance is calculated, since the Monte Carlo simulation does not necessarily model accurately the tails of the luminous region in z. Muon candidates in the data are required

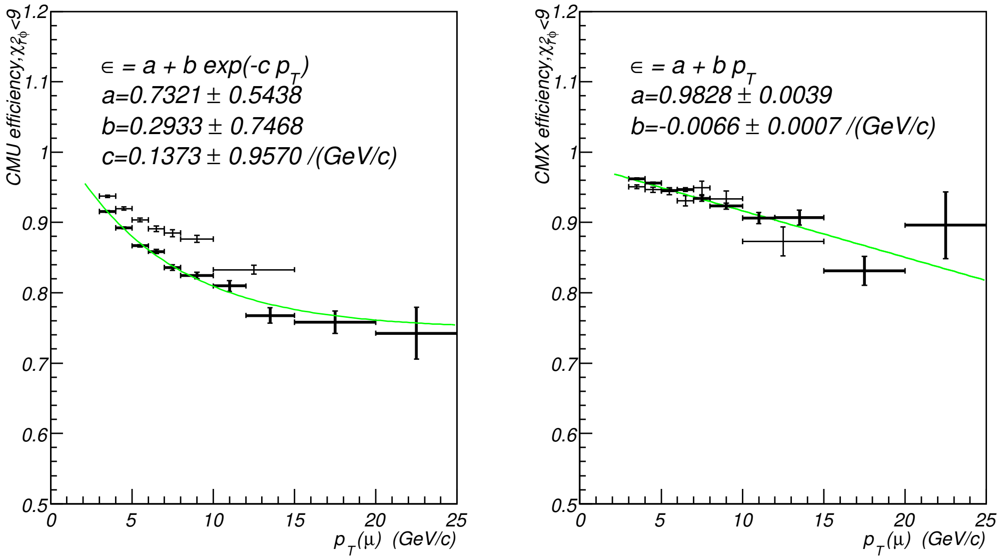

Figure 3: Muon $\chi^2_{r\phi} < 9$ efficiency for CMU (left) and CMX (right) as a function of $p_T(\mu^{\pm})$. The thick error bars correspond to the efficiencies measured using the $\Upsilon(nS)$ sample while the thin error bars correspond to the μ+SVT sample.

to have $|z_0| < 60$ cm and $|\Delta z_0| < 5$ cm. The efficiencies for these requirements have been measured and found to be $95.6 \pm 0.3\%$ and $99.9 \pm 0.2\%$, respectively[6, 7] from which we obtain

$$\epsilon_{\rm vtx} = 95.50 \pm 0.35\ \%. \tag{17}$$

The efficiency in Equation 17 was measured using minimum bias events up to September 4, 2005 (run 203799). The rest of this section describes a new measurement of this efficiency using J/ψ data as a cross check which also extends the range of applicability up to run 289182.

The luminous region is parameterized by a probability density of the form

$$f(z) \sim \frac{e^{-(z-\Delta z)^2/2\sigma_z^2}}{1 + (z - \Delta z)^2/\beta^{*2}} \tag{18}$$

but events recorded using the `JPSI_CMUCMU1.5` trigger have their acceptance restricted due to the limited fiducial coverage of both XFT and the CMU. The acceptance for CMU muons with $p_T >$ 3 GeV/c is calculated using the samples of Monte Carlo events described later in Section 4 with the XFT fiducial restrictions that reject tracks that have trajectories that lie close to the COT spacers on the axial superlayers. Figure 4 shows the calculated muon acceptance as a function of its longitudinal impact parameter and pseudorapidity. The probability density for triggering on di-muon event is expressed

$$f(z, \eta_1, \eta_2) \sim f(z) \cdot g(\eta_1) g(\eta_2) \cdot \mathcal{A}(z, \eta_1) \mathcal{A}(z, \eta_2) \tag{19}$$

where $f(z)$ is the parameterization shown in Equation 18, $g(\eta)$ is an imperical parameterization of the pseudorapidity distribution and $\mathcal{A}(z, \eta)$ is the calculated acceptance shown in Figure 4. The functions $g(\eta)$ are parameterized by a polynomial,

$$g(\eta) \sim 1 + a\eta^2 + b\eta^4 \tag{20}$$

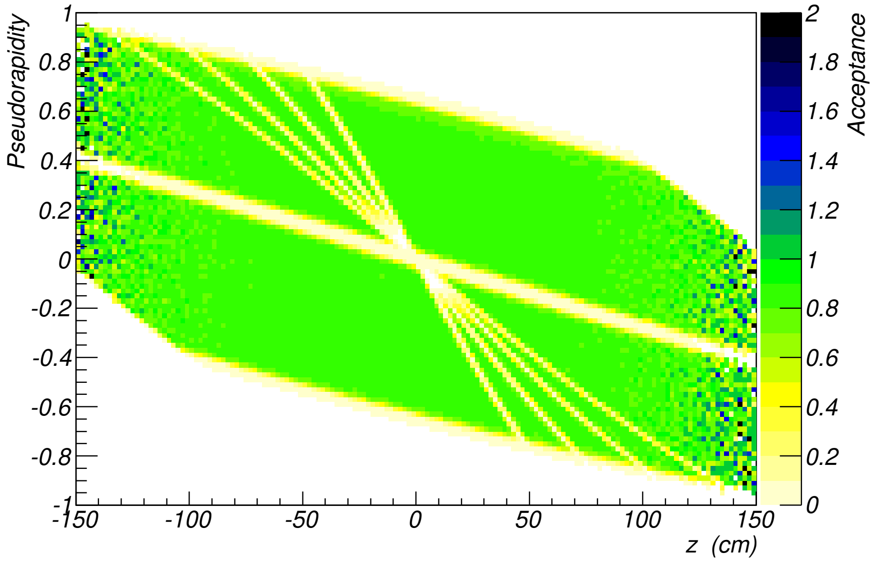

Figure 4: Single-muon XFT+CMU acceptance calculated using Monte Carlo for muons with $p_T >$ 3 GeV/c.

and any rapidity correlations between the two muons is ignored.

The observed distribution is fit using a binned likelihood fit to obtain the parameters Δz, σ_z and β^* for several sections of contiguous events. Figure 5 shows an example of one such fit projected onto the z-axis. The Monte Carlo samples are generated with a distribution of z_{vtx} that is similar to the distribution observed in data. Therefore, the fit is performed only over the range $|z| < 100$ cm to avoid the regions where the Monte Carlo statistics in the generated samples is insufficient to precisely quantify the acceptance.

The efficiency for the $|z_{\mathrm{vtx}}| < 60$ cm requirement is calculated by numerically integrating the function in Equation 18 from -60 cm to $+60$ cm. The uncertainty is calculated using Monte Carlo sampling of the fitted parameters over the 3-dimensional correlated Gaussian distribution calculated from their covariance matrix. Figure 6 shows the efficiency calculated in this way for the run ranges considered.

The luminous region is described with reasonably accurately in the Monte Carlo. Figure 7 shows the distribution of the three parameters in Equation 18 from the fits to the J/ψ samples compared with the values obtained by fitting the generated z-vertex distribution in Monte Carlo events.

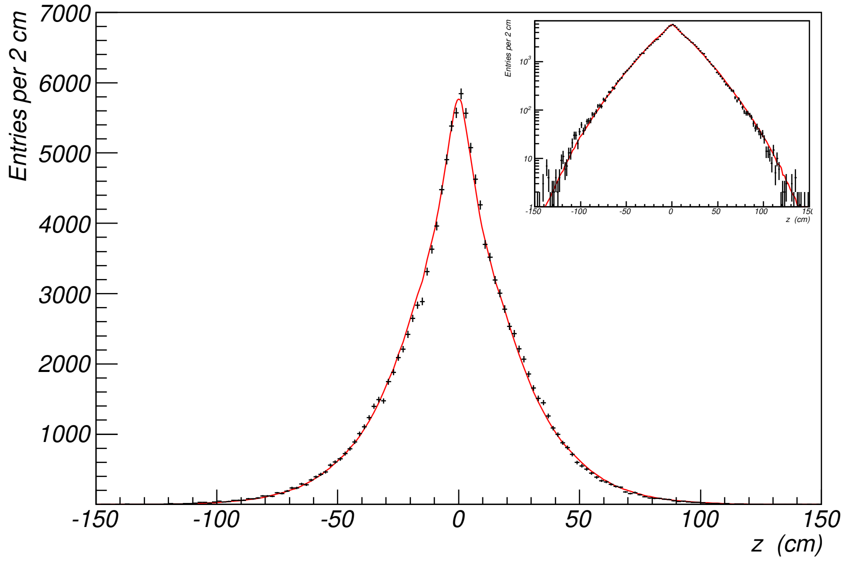

Figure 5: Example of one of the fits used to measure the shape of the luminous region using events in the jpmm dataset. Data used for this fit was from runs 271599–274196.

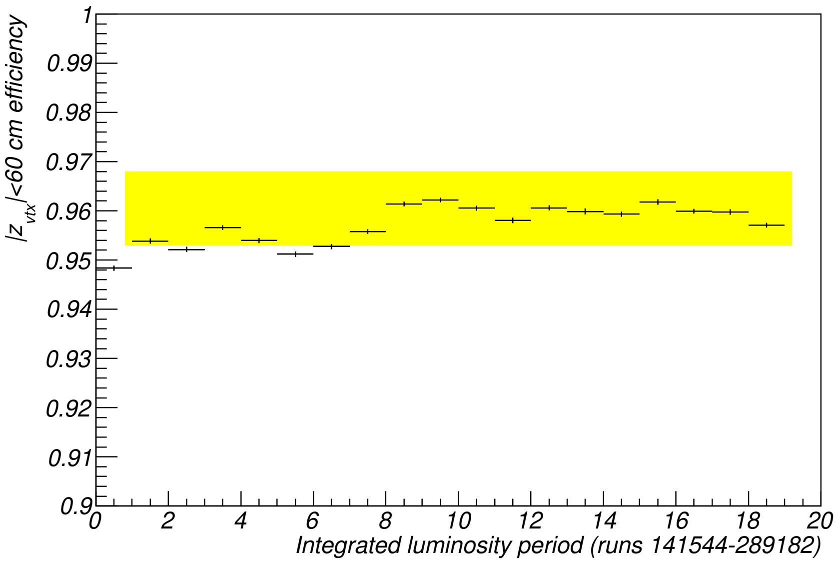

Figure 6: Efficiency for the $|z_{\mathrm{vtx}}| < 60$ cm requirement as a function of data taking interval, each of which corresponds to approximately 400 pb^{-1}. The shaded region indicates the previous measurement of the efficiency made using minimum bias events.

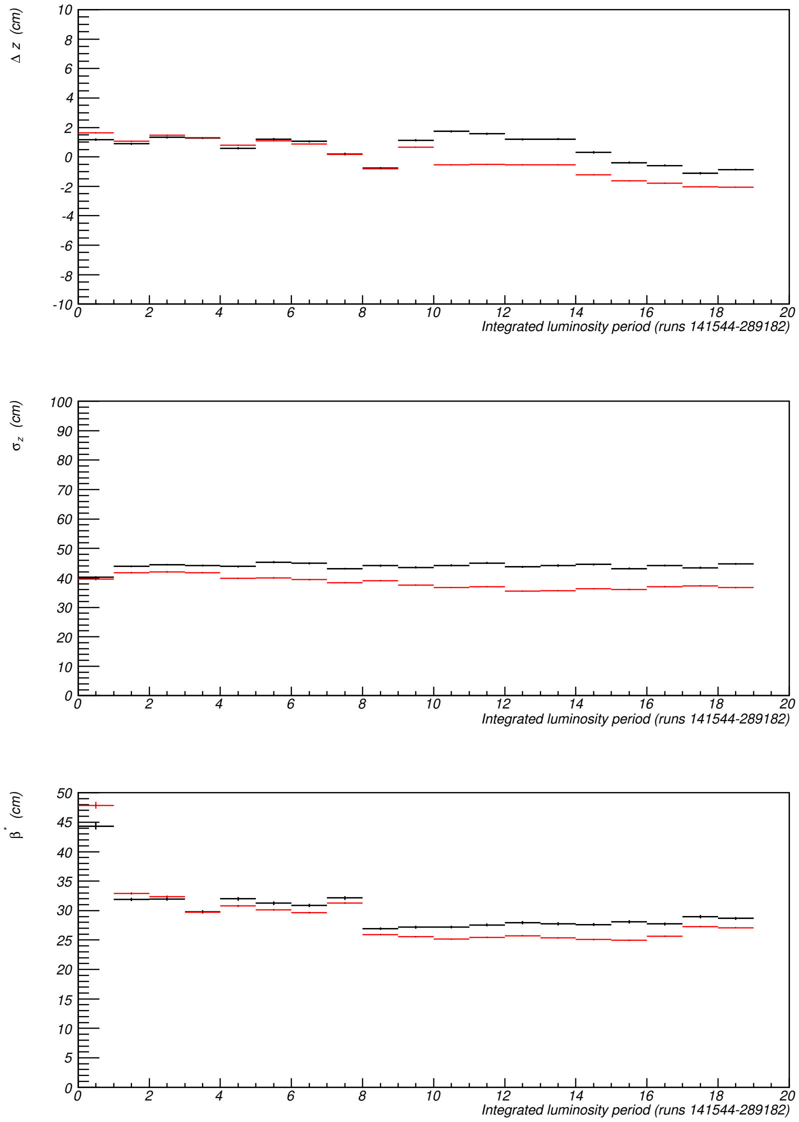

Figure 7: Fitted parameters characterizing the luminous region as a function of data taking period for data (black) and Monte Carlo (red).

3.4 Level 1 CMU/CMX trigger

Level 1 muon trigger efficiencies are calculated using version 4.4 of the `MuonLoPtEfficiency` tool. The run-dependent efficiencies for the `L1_CMU_1G5` and `L1_CMX_2G` trigger requirements are calculated using the `getL1Efficiency` method. This version does not provide efficiencies for runs greater than 261005, so the efficiency in later runs is calculated by passing a run number equal to 261005.

The level 1 trigger efficiencies calculated in this way represent the probability that an offline CdfMuon object satisfying the same selection criteria used in this analysis, will also satisfy the requirements of the Level 1 trigger. These efficiencies are parametrized as functions of run number, p_T, η and ϕ_0, so they are used to randomly reject muons reconstructed in the Monte Carlo samples.

3.5 CMP trigger efficiency

The accurate modeling of the detector acceptance requires a description of the efficiency with which muons triggered at level 1 in CMU are associated with stubs in CMP. This efficiency is measured using $J/\psi \to \mu^+\mu^-$ decays selected using CMU+CMU and CMU+CMX trigger paths which do not impose any requirement on CMP activity. The J/ψ triggers imposed the requirement that $|\Delta x_{CMU}| < 20$ cm which is looser than the 15 cm cut used in the higher p_T upsilon triggers. Thus, the muons used to study the CMP trigger efficiency are required to satisfy $|\Delta x_{CMU}| < 15$ cm for consistency but no additional efficiency correction is applied since the tighter cut has an efficiency greater than 99.8% for muons with $p_T > 4$ GeV/c.

The efficiency is analyzed separately in 24 azimuthal wedges as a function of $1/p_T$. In addition, the efficiency as a function of z within the CMP detector is examined using muons with $5 < p_T < 10$ GeV/c. In all cases, the muon efficiency is measured by performing binned likelihood fits to the di-muon mass distributions, comparing J/ψ signal yields with and without imposing the CMP stub requirement. Figure 8 shows an example of the fits to the di-muon mass distribution from which the efficiency in one bin of $1/p_T$ is determined. This figure also shows the efficiency as a function of $1/p_T$, for muons with $20 < |z| < 280$ cm, and as a function of z, for muons with $5 < p_T < 10$ GeV/c. The muon efficiency is determined from the ratio of J/ψ signal yields, while the background efficiency is obtained from the ratio of the background levels.

The muon efficiency is fitted with a function of the form

$$\epsilon(1/p_T) = \epsilon_0 \cdot (1 + \beta/p_T^q) \cdot \frac{1}{2}\mathrm{Erfc}\left(\frac{1/p_T - \mu}{\sigma\sqrt{2}}\right). \tag{21}$$

where the first term in brackets accounts for the small slope observed in the efficiency at high p_T in some wedges. Figure 9 shows an example of the fitted efficiency in two wedges, one that exhibits the typical shape and one that is unique. The complete set of plots showing fits in all wedges is included in Appendix B.

3.6 Final state radiation

A Gaussian function does not account for the radiative tail in the invariant mass distribution of the $\Upsilon(nS)$ signals. Therefore, the yields estimated using Gaussian fits will be biased and this bias must be accounted for when calculating cross sections from the fitted yields. Alternatively, a Crystal Ball function, which includes a radiative tail component, can be used but it will still be necessary to estimate the size of any possible bias that could result from other inadequacies of this parameterization.

Figures 10 and 11 show the fitted fraction of Monte Carlo $\Upsilon(1S)$ decays as a function of p_T when the signal is fitted using a single Gaussian function or a Crystal Ball function.

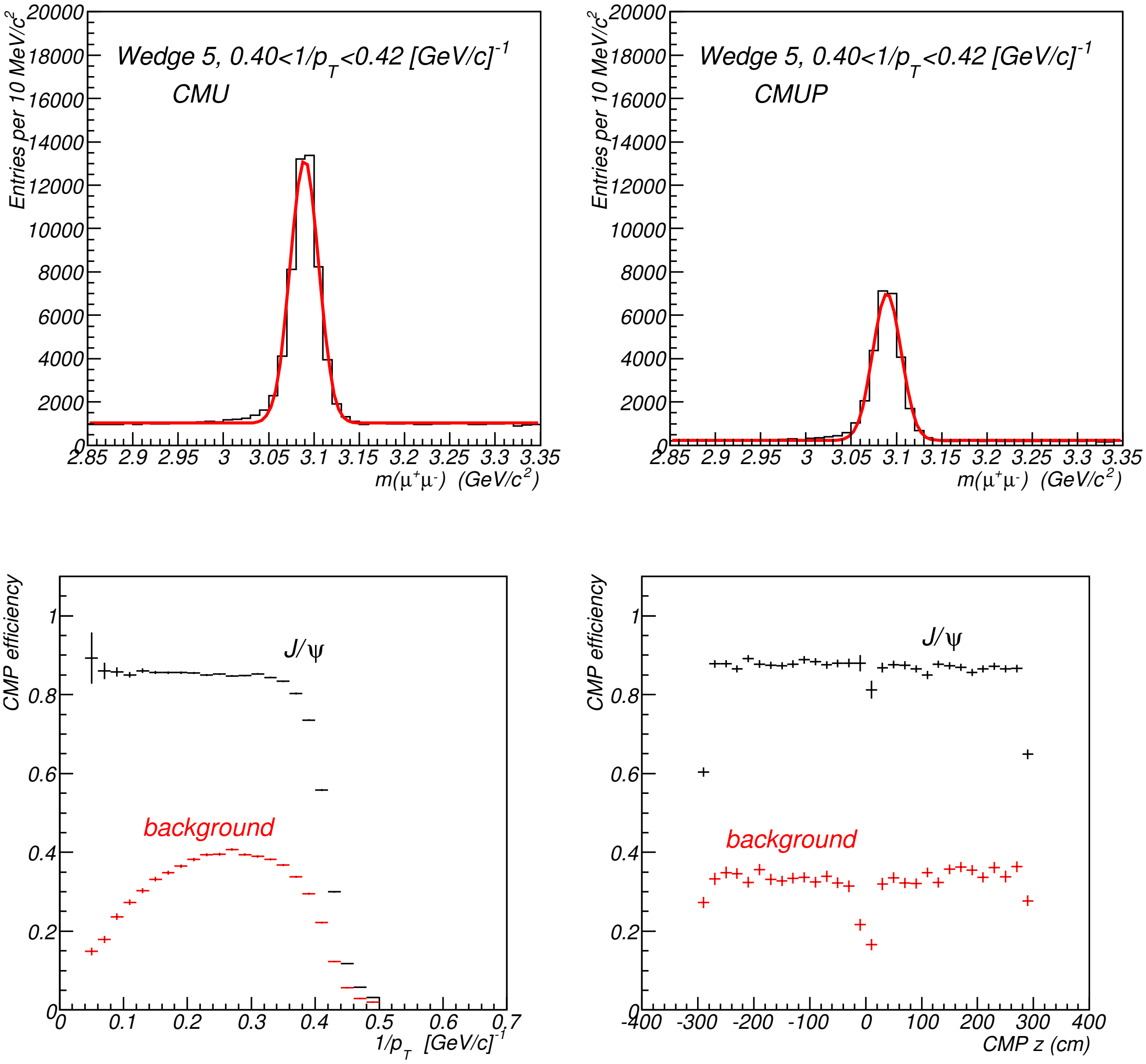

Figure 8: Fitted di-muon invariant mass distributions from which the efficiency is derived (top). The bottom plots show the calculated efficiency for muons identified in CMU to have a CMP stub as a function of $1/p_T$ and of the CMU z-coordinate.

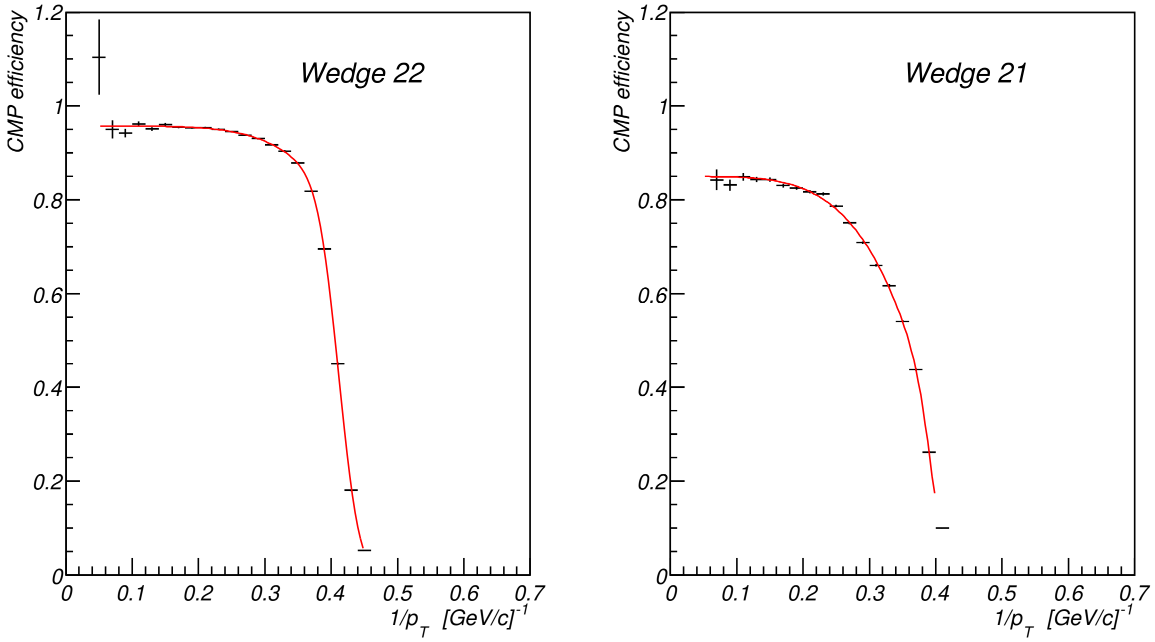

Figure 9: Examples of fits to the CMP efficiency measured as a function of $1/p_T$ in wedges 22 and 21.

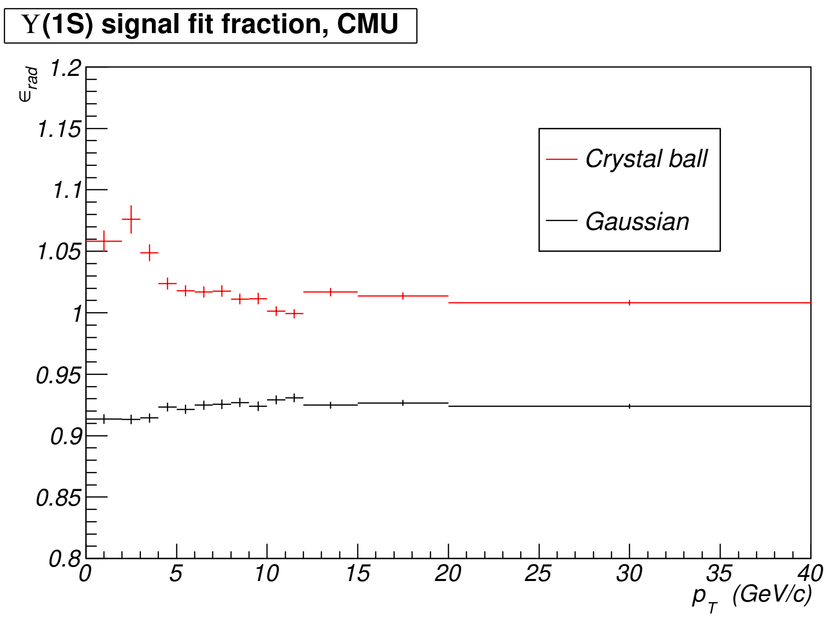

Figure 10: Ratio of fitted Gaussian area to the total number of reconstructed simulated $\Upsilon(1S)$ decays in the CMUP+CMU trigger path as a funciton of p_T.

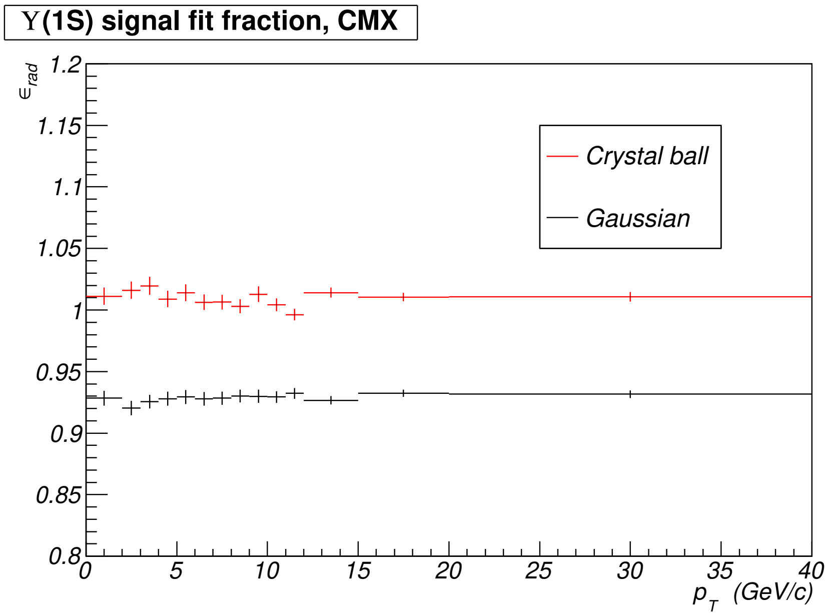

Figure 11: Ratio of fitted Gaussian area to the total number of reconstructed simulated $\Upsilon(1S)$ decays in the CMUP+CMX trigger path as a funciton of p_T.

4 Monte Carlo generation

This analysis makes use of Monte Carlo templates to describe the un-polarized distributions of $(\cos\theta, \phi)$ in the three $\Upsilon(nS)$ signals and in the background. A Monte Carlo event generator was written and interfaced with the AC++ framework to produce these samples. The simulation tar file was built using release 6.1.4mc.m patch t, updated with revision 1.17 of the file `setup_alignment_table.tcl`, which was needed to simulate run numbers greater than 277512. The list of runs to simulate was created by selecting runs in the good run list for which there were no bad run sections and had valid luminosity information. The runlist constructed in this way contained 5775 runs in the range 141544 to 289182.

4.1 Matching p_T and rapidity distributions

The acceptance to be calculated using the Monte Carlo represents the average over a range of $\Upsilon(nS)$ transverse momentum and rapidity. Because the acceptance can depend on these variables, it is important that the distribution of p_T and y in the generated events used to calculate the acceptance matches the underlying distributions in the data. This is achieved by first generating di-muon samples with flat p_T and y distributions to calculate the efficiency in smaller ranges of p_T and y, and then using these to correct the observed yields of reconstructed signal and background. The corrected distributions are fit to functions of p_T and y from which the probability density function used to generate the (p_T, y) distributions of a second Monte Carlo sample is calculated. The analysis of one range of p_T is described in detail, while the results from other ranges of p_T are treated similarly.

Consider the subset of the di-muon candidates for which $7.5 < p_T(\mu^+\mu^-) < 9.5$ GeV/c. The distribution of their invariant mass is shown in Figure 12 along with a fit from which the reconstructed yields are estimated. Figure 13 shows the yields in the four smaller ranges of p_T considered while Figure 14 shows the yields in different ranges of rapidity. The acceptance calculated for the cor-

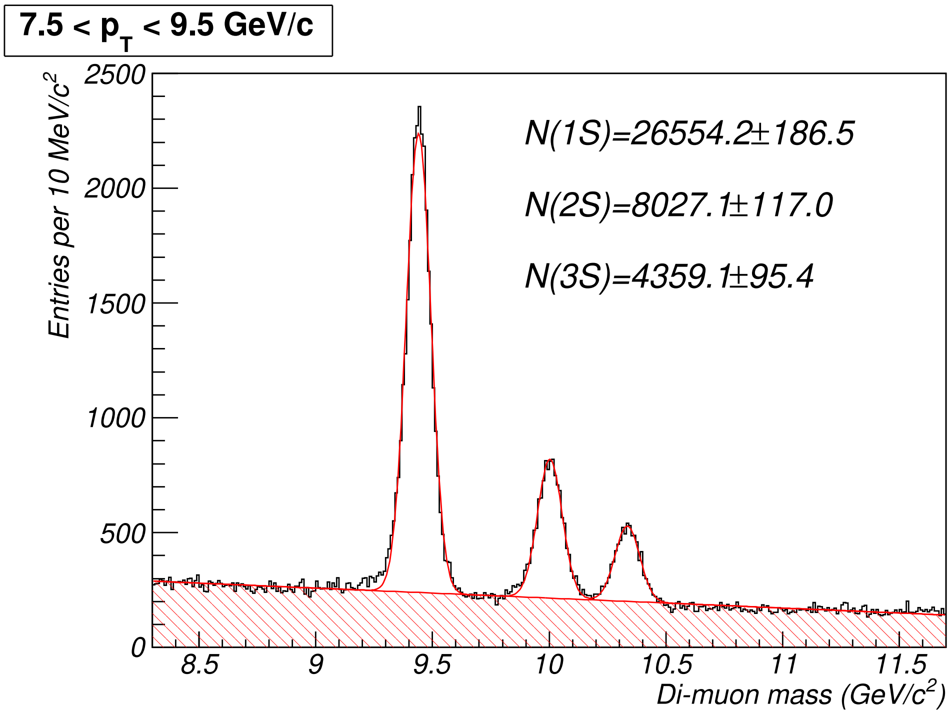

Figure 12: Signal yields in the p_T range from 7.5 to 9.5 GeV/c and rapidity $|y| < 0.8$.

responding ranges of p_T and y is used to correct these yields to obtain the differential distributions shown in Figure 15. Over these limited ranges of p_T and rapidity the efficiency corrected differential yields appear to be adequately parameterized by an exponential function for $p_T > 7$ GeV/c and by quadratic functions for smaller p_T. Figure 16 shows the distribution of corrected yields as a function of p_T with the fits to individual ranges of p_T superimposed. Within each p_T range, the dependence of the $\Upsilon(nS)$ cross section on rapidity is analyzed by fitting an exponential function to the distribution of dN/dy when $p_T > 7$ GeV/c and to a quadratic function when $p_T < 7$ GeV/c. The fractional variation in the yield is defined as $1/N dN/dy$, in which N is the efficiency corrected yield evaluated at the mean p_T of the sub-sample, and dN/dy is the slope of the corrected yield as a function of rapidity. These fractional variations are shown in Figure 17 and indicate that although there may be some evidence for systematic variation in the cross section with rapidity, this effect is generally small. For this reason, we approximate the rapidity dependence in the templates using just a uniform distribution.

The background is parameterized by a function of the form

$$f(m, p_T, y) \propto (1 + \alpha m)(1 + \beta|y|)e^{\gamma p_T} \tag{22}$$

when $p_T > 7$ GeV/c and

$$f(m, p_T, y) \propto (1 + \alpha m)(1 + \beta|y|)(1 + \gamma p_T + \delta p_T^2) \tag{23}$$

for $p_T < 7$ GeV/c.

4.2 CMU fiducial coverage

The Monte Carlo does not model the dead chamber in wedge 8W, and shortens all chambers in wedge 6E. To accommodate these differences, muons in the dead region of wedge 8W and those in wedge 6E

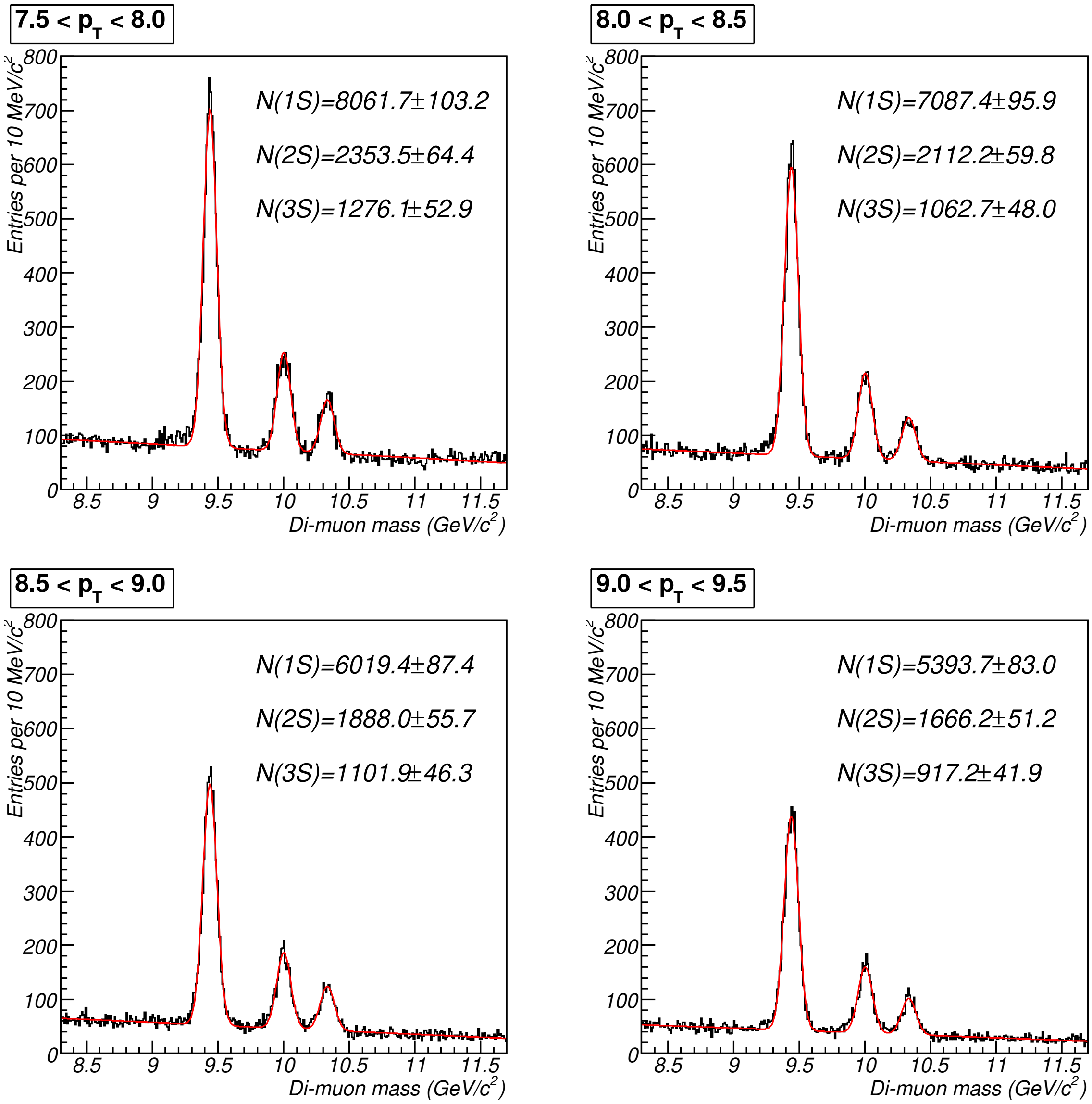

Figure 13: Signal yields in four p_T ranges from 7.5 to 9.5 GeV/c with $|y| < 0.8$.

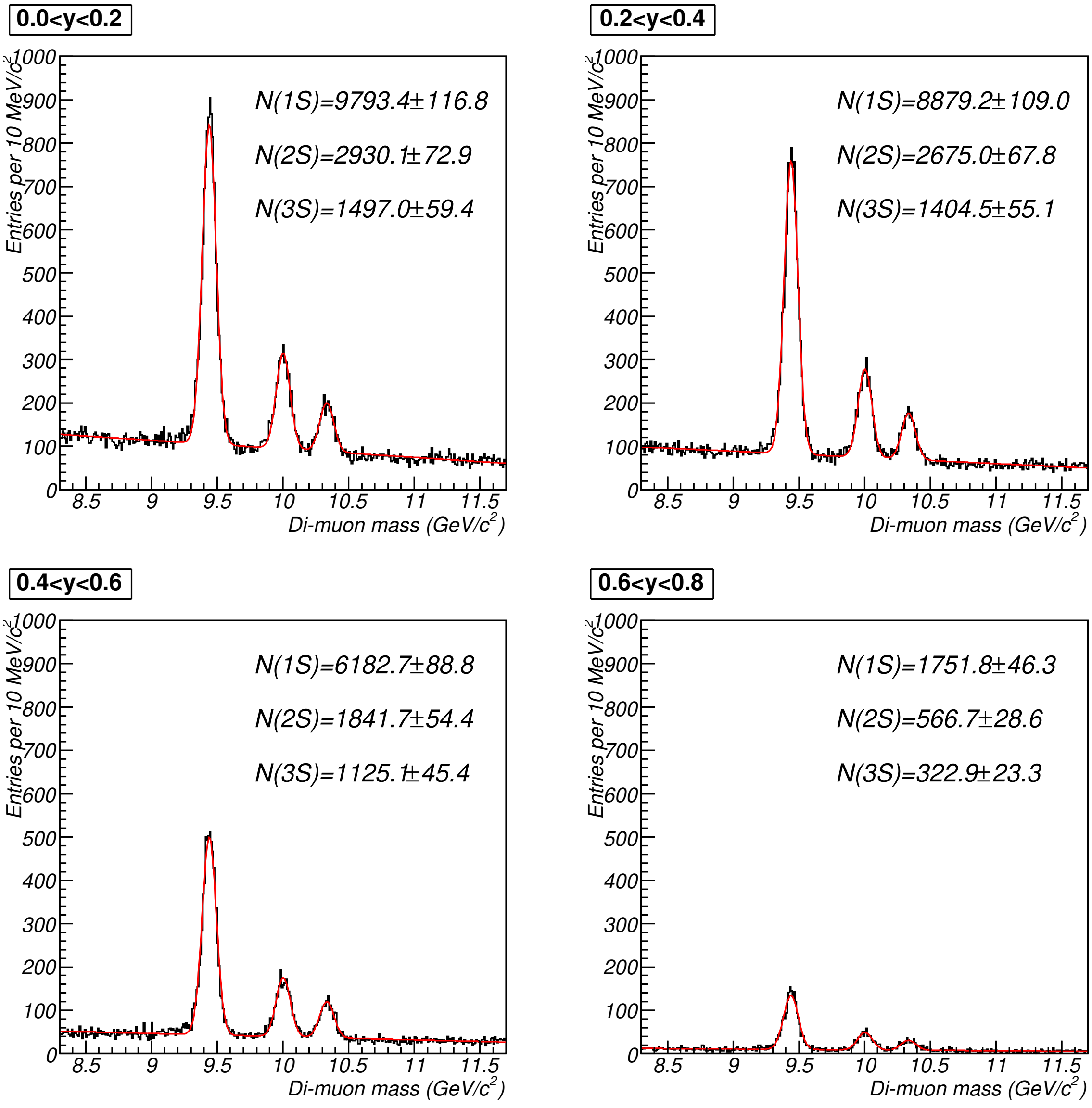

Figure 14: Signal yields in four rapidity ranges for di-muon candidates with p_T in the range 7.5 to 9.5 GeV/c.

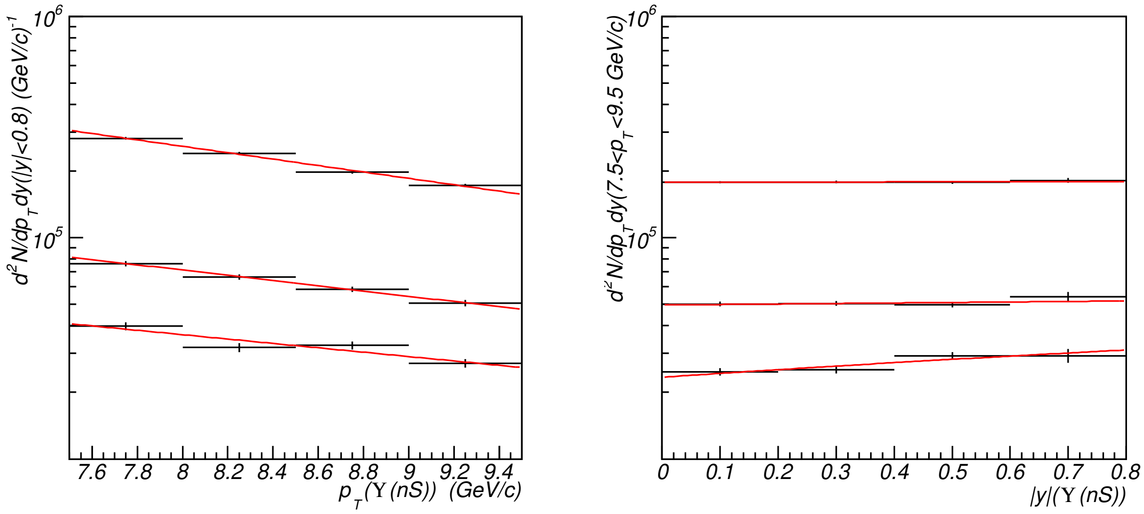

Figure 15: Acceptance and efficiency corrected $\Upsilon(nS)$ yields with p_T in the range 7.5 to 9.5 GeV/c. The fitted curves, from top to bottom, correspond to the $\Upsilon(1S)$, $\Upsilon(2S)$ and $\Upsilon(3S)$ yields, respectively.

with $|z| > 200$ cm are rejected in both data and Monte Carlo. The resulting agreement is illustrated by Figure 18 which shows the distribution of coordinates at which tracks intersect the CMU chambers in a plane at a nominal radius of 347 cm. Figure 19 shows the data/MC comparisons of the normalized distributions of v-coordinate within individual wedges and the longitudinal coordinate in the nominal plane of the CMU chambers. The agreement is reasonably good, although there are minor differences in the kinematics of the reconstructed and simulated events.

4.3 CMP fiducial coverage

Figure 20 illustrates the agreement between the CMP acceptance in data and simulated in the Monte Carlo. Figures 21 and 22 show the data/MC comparison of the distributions of $\phi_0(\mu^{\pm})$ and $\eta(\mu^{\pm})$ from $\mu^+\mu^-$ candidates selected with similar kinematics. Again, the level of agreement suggests that no gross features have been omitted from the simulation.

4.4 CMX fiducial coverage

Figure 23 illustrates the agreement between the CMX acceptance in data and simulated in the Monte Carlo. Figures 24 and 25 show the data/MC comparison of the distributions of $\phi_0(\mu^{\pm})$ and $\eta(\mu^{\pm})$ from $\mu^+\mu^-$ candidates selected with similar kinematics. This comparison includes the periods when the CMX mini-skirt installation was not yet completed.

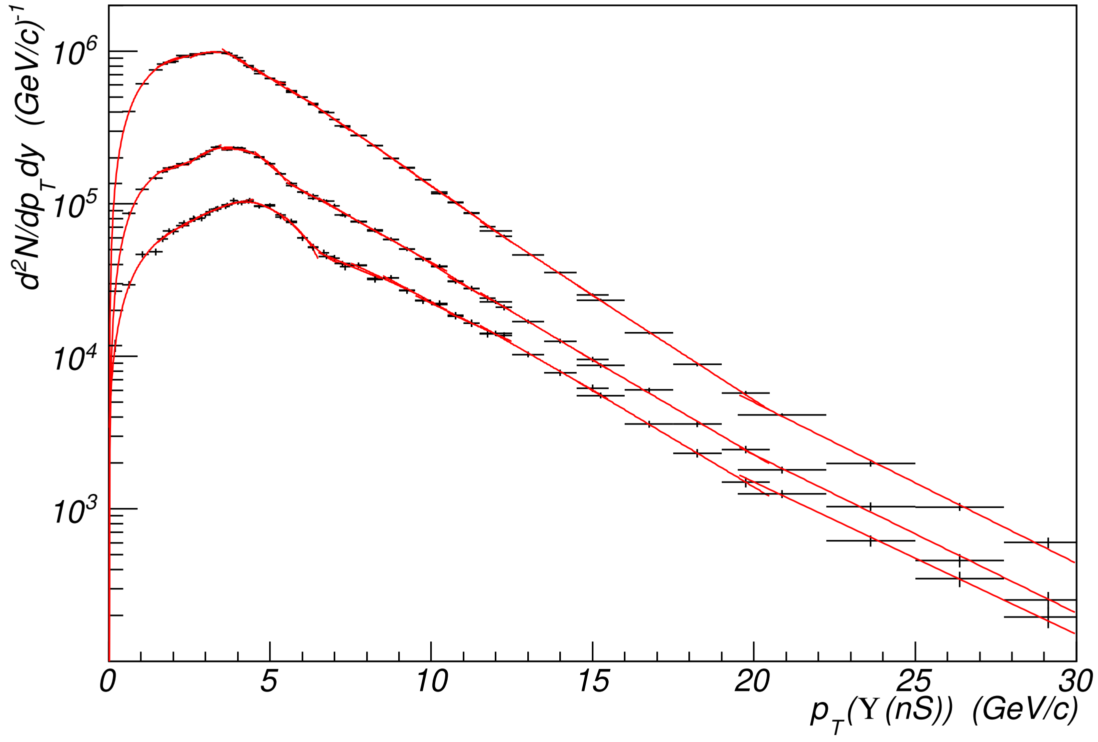

Figure 16: Acceptance and efficiency corrected $\Upsilon(nS)$ yields as a function of p_T with quadratic and exponential fits to smaller p_T ranges superimposed. From top to bottom, the three curves correspond to the $\Upsilon(1S)$, $\Upsilon(2S)$ and $\Upsilon(3S)$ yields, respectively.

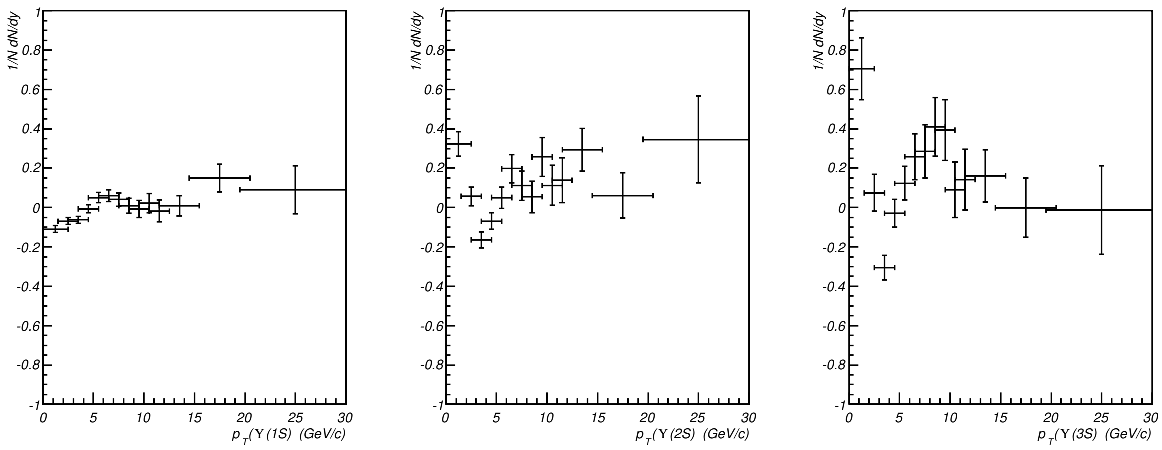

Figure 17: Fractional variation in the acceptance and efficiency corrected $\Upsilon(nS)$ yields with rapidity as a functions of $p_T(\Upsilon)$.

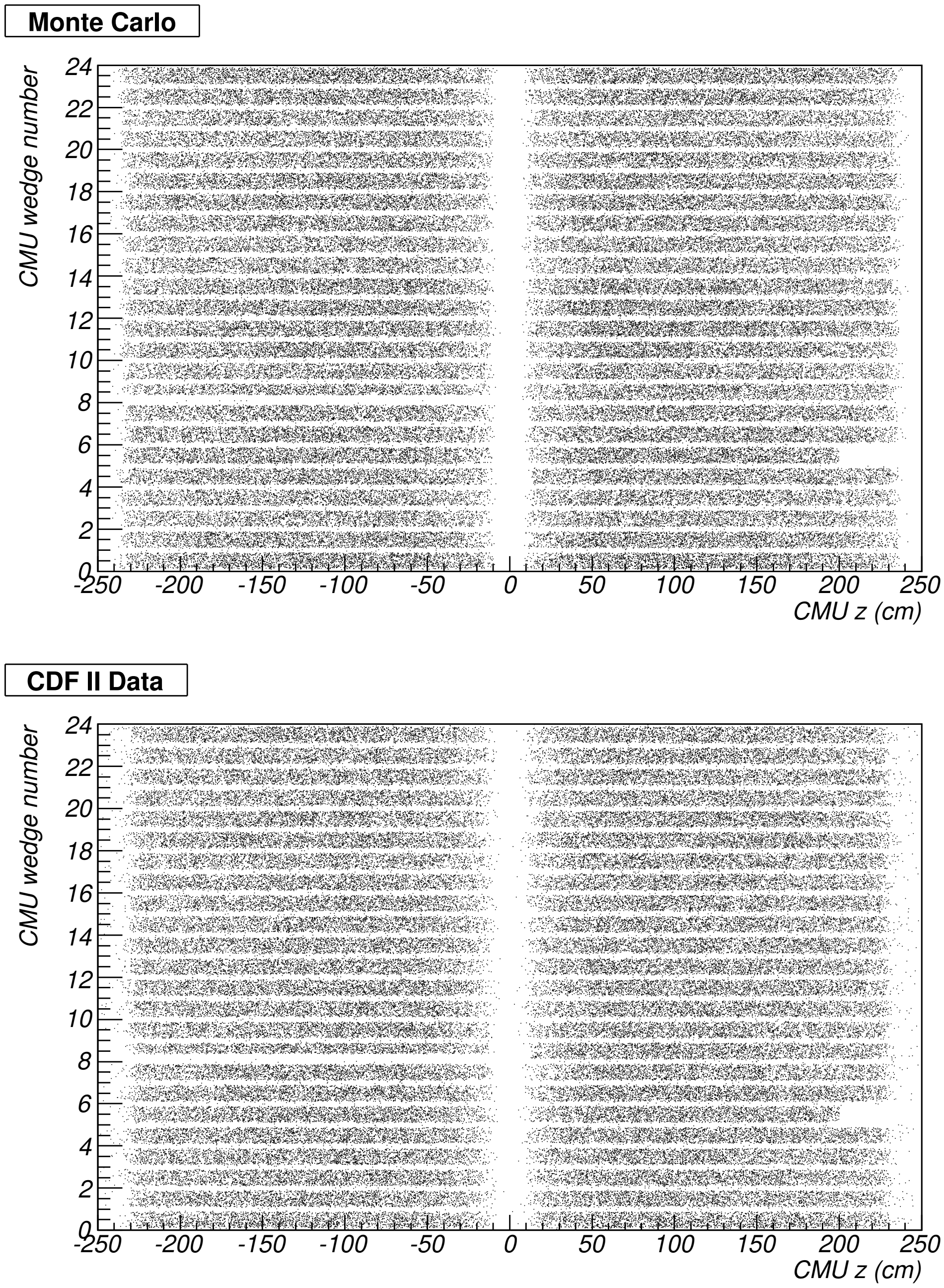

Figure 18: Comparison between CMU fiducial acceptance in Monte Carlo (top) and in data (bottom).

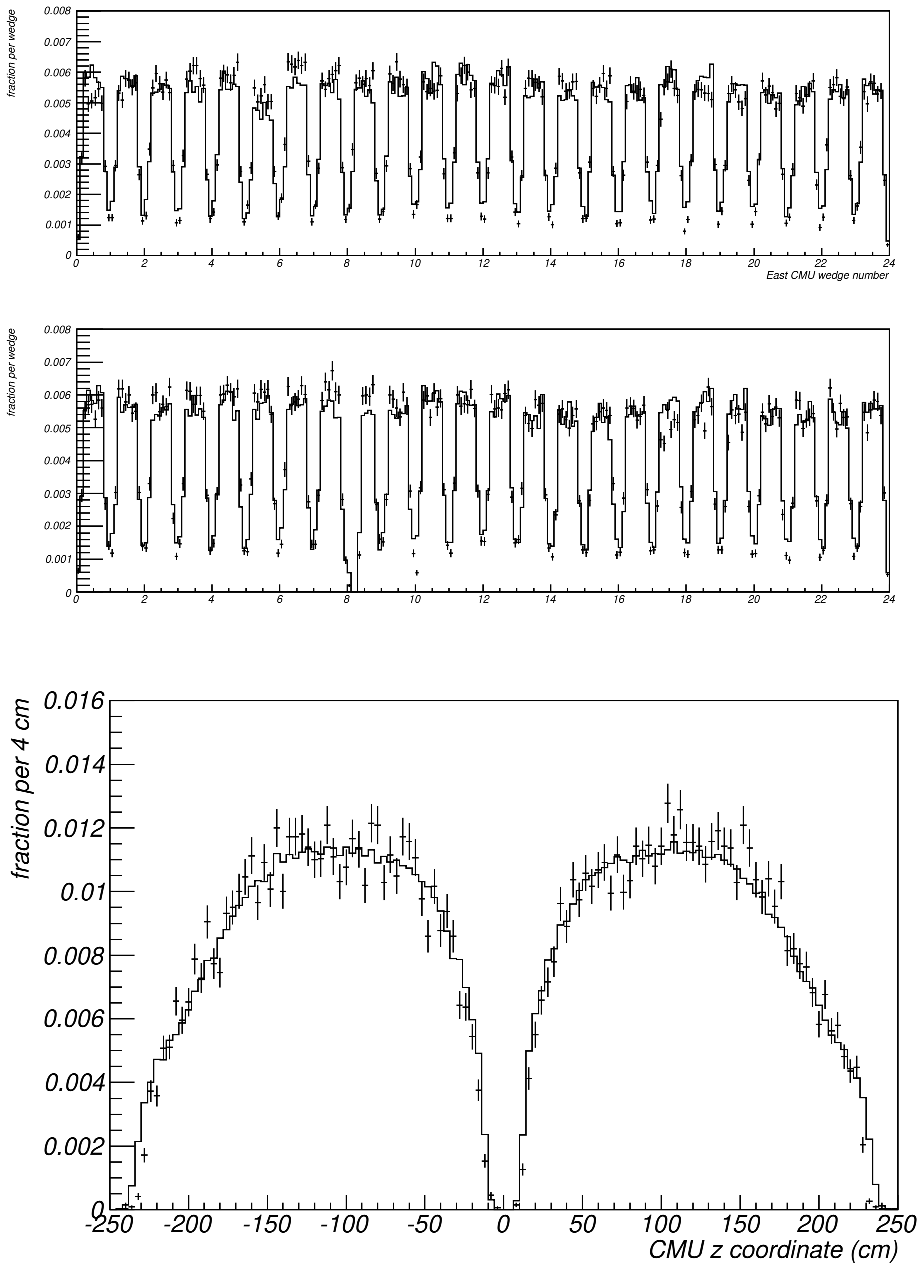

Figure 19: Comparison between transverse (top) and longitudinal (bottom) coordinates of muons in the plane of the CMU chambers. The histograms show the distribution in Monte Carlo, while the data is shown with error bars.

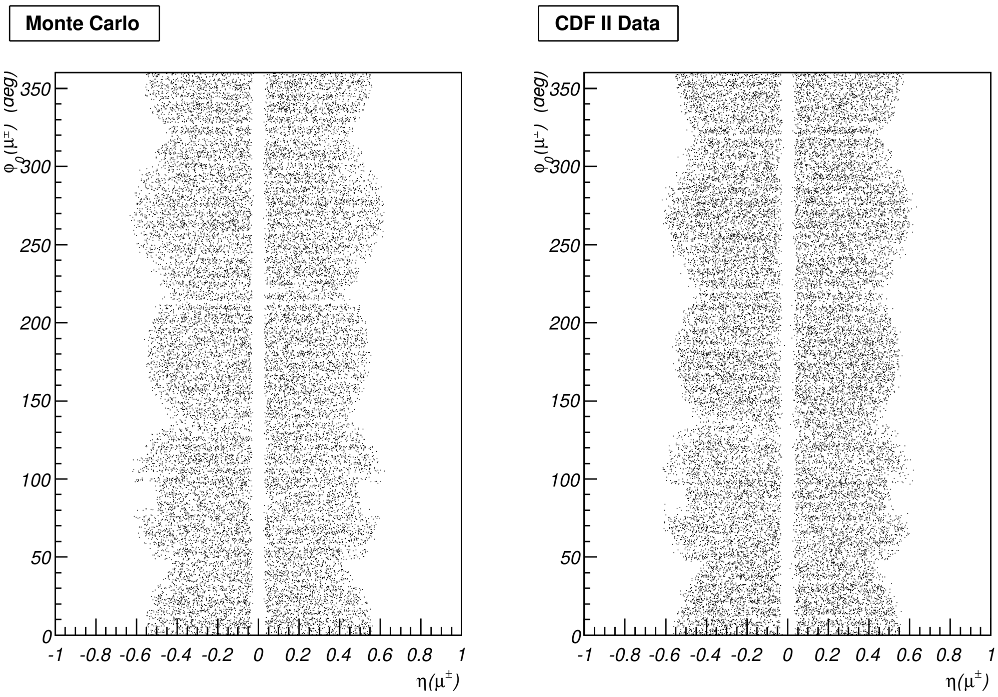

Figure 20: Comparison of CMP fiducial acceptance in Monte Carlo and in data. In this comparison, tracks were selected with $|z_0(\mu^{\pm})| < 1$ cm to identify the restriction on the fiducial acceptance imposed by the additional CMU requirement.

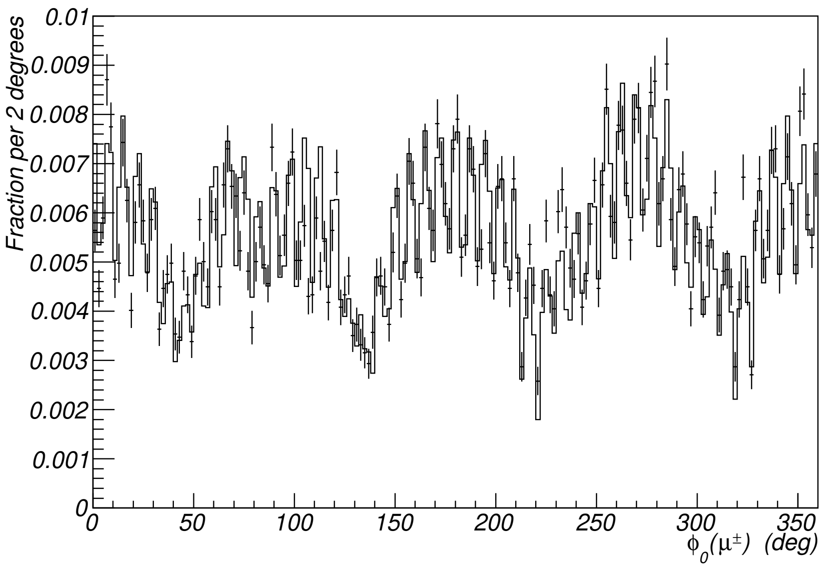

Figure 21: Comparison of the distribution of $\phi_0(\mu^{\pm})$ for CMP muons in data (error bars) and Monte Carlo (histogram).

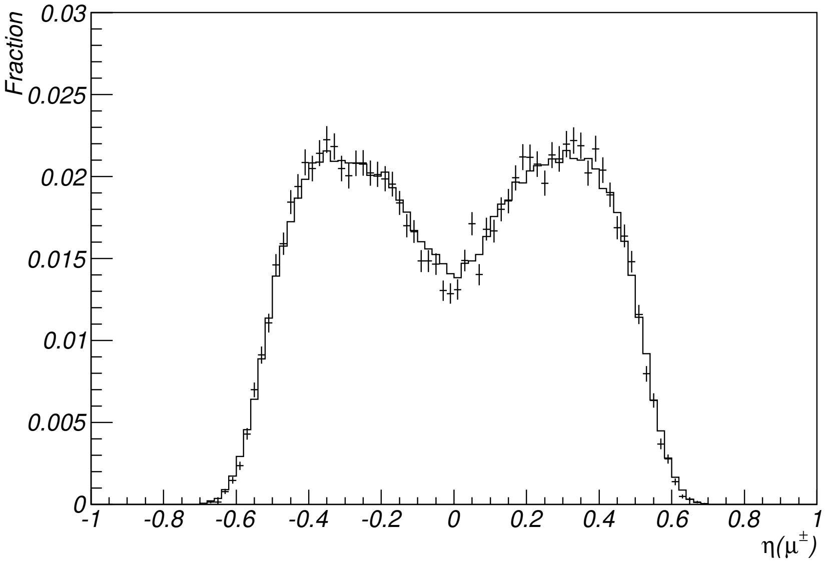

Figure 22: Comparison of the distribution of $\eta(\mu^{\pm})$ for CMP muons in data (error bars) and Monte Carlo (histogram).

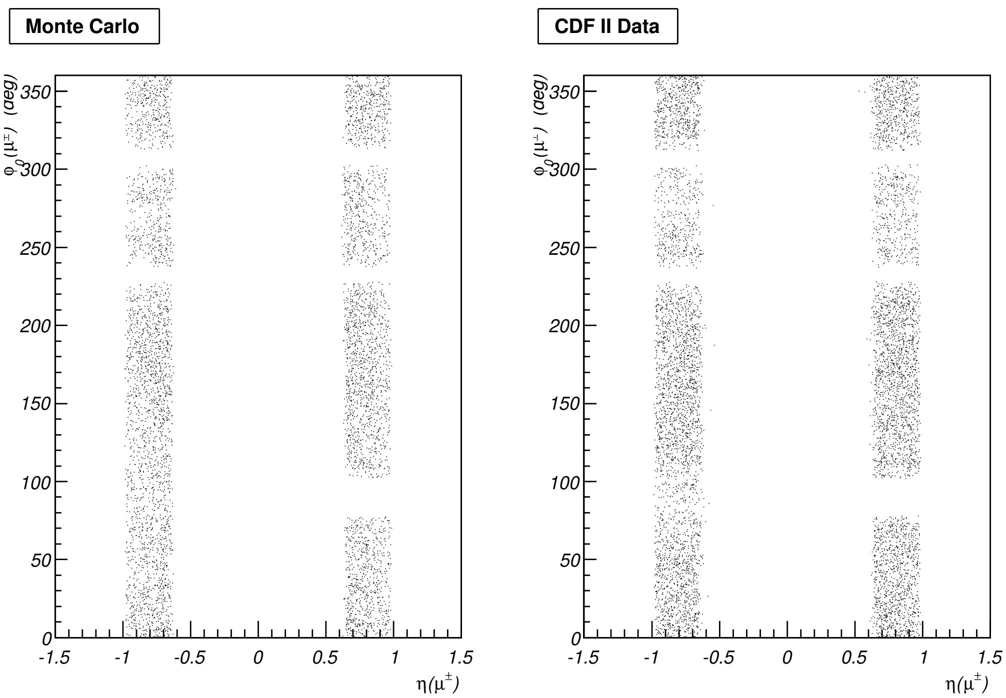

Figure 23: Comparison of CMX fiducial acceptance in Monte Carlo and in data.

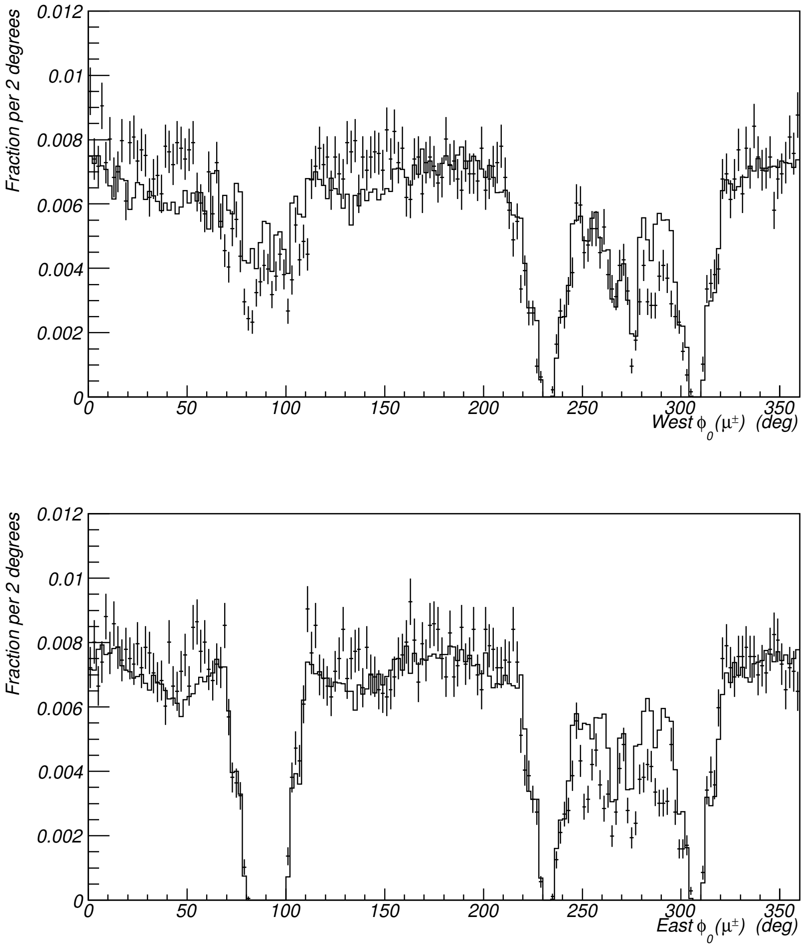

Figure 24: Comparison of the distribution of $\phi_0(\mu^{\pm})$ for CMX muons in data (error bars) and Monte Carlo (histogram).

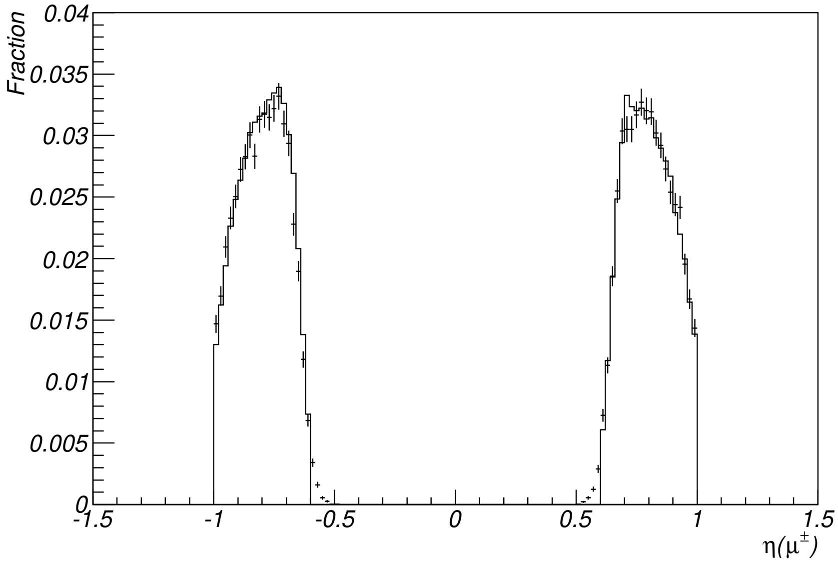

Figure 25: Comparison of the distribution of $\eta(\mu^{\pm})$ for CMX muons in data (error bars) and Monte Carlo (histogram).

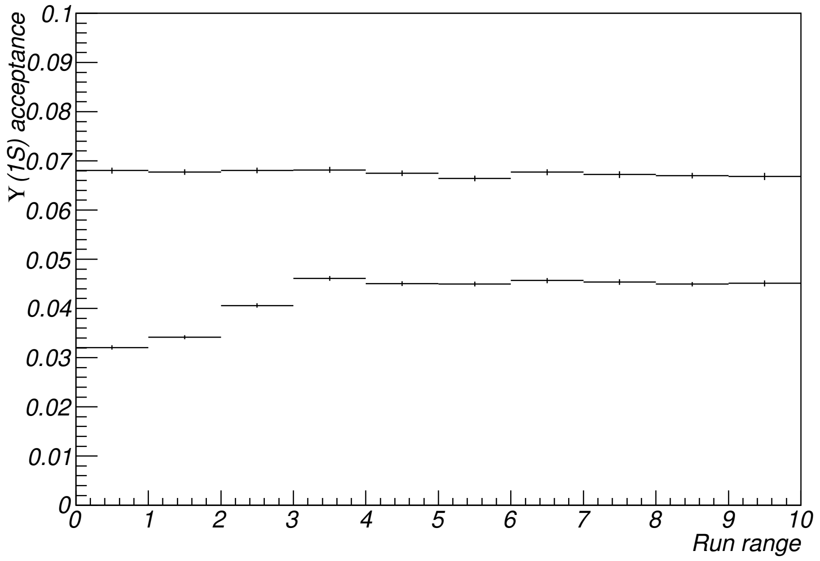

Figure 26: Detector acceptance calculated for $\Upsilon(1S)$ decays with $8.5 < p_T < 10.5$ GeV/c and $|y| < 0.6$ that are fiducial in CMUP+CMU (upper points) and in CMUP+CMX (lower points).

5 Search for time dependent effects

In low-statistics samples, such as $B^+ \to J/\psi K^+$, comparisons are made between the `0d-0k` data sets and the `0m` dataset. Samples with higher statistics allow comparisons to be made on shorter time scales, but these generally suffer from trigger biases that require careful interpretation.

5.1 Monte Carlo acceptance calculation

Figure 26 shows the $\Upsilon(1S)$ acceptance as a function of run range, calculated using a Monte Carlo sample for which the simulation of level 1 and level 2 trigger efficiencies was skipped. Thus, it represents the geometric acceptance of the CMU and CMX muon systems as a function of time and does not include time-dependent trigger effects. A constant function fit to the CMU acceptnace yields an average acceptance of 0.0675 ± 0.0002 with a χ^2/dof of 8.56/9 which has a P-value of 0.48. A fit the CMUP+CMX acceptance for run periods 3..10 yields an average acceptance of 0.0453 ± 0.0002 with $\chi^2/dof = 4.36/6$ which has a P-value of 0.63. Significant variation in the acceptance is evident for run periods 0, 1 and 2, but this is due to the acceptance changes described in section 2.4 that account for the incremental instrumentation of the components of CMX.

5.2 Absolute track reconstruction efficiency

Changes in the absolute track reconstruction efficiency are studied by measuring the ratio of the $J/\psi K^+$ yield to the yield of $J/\psi \to \mu^+\mu^-$ in specific trigger paths. Figure 27 shows invariant mass distributions containing the J/ψ and $J/\psi K^+$ signals reconstructed in the `jpmm0d`, `jpmm0h` and `jpmm0j` datasets, compared with those reconstructed in the `jpmm0m` dataset. The J/ψ signals are fit with a single Gaussian and a linear background while the $J/\psi K^\pm$ signals are fit with a single Gaussian and a linear background with a step function that turns off one pion mass below the mass of the $B^\pm$ signal peak, convoluted with the $B^\pm$ signal resolution parameter.

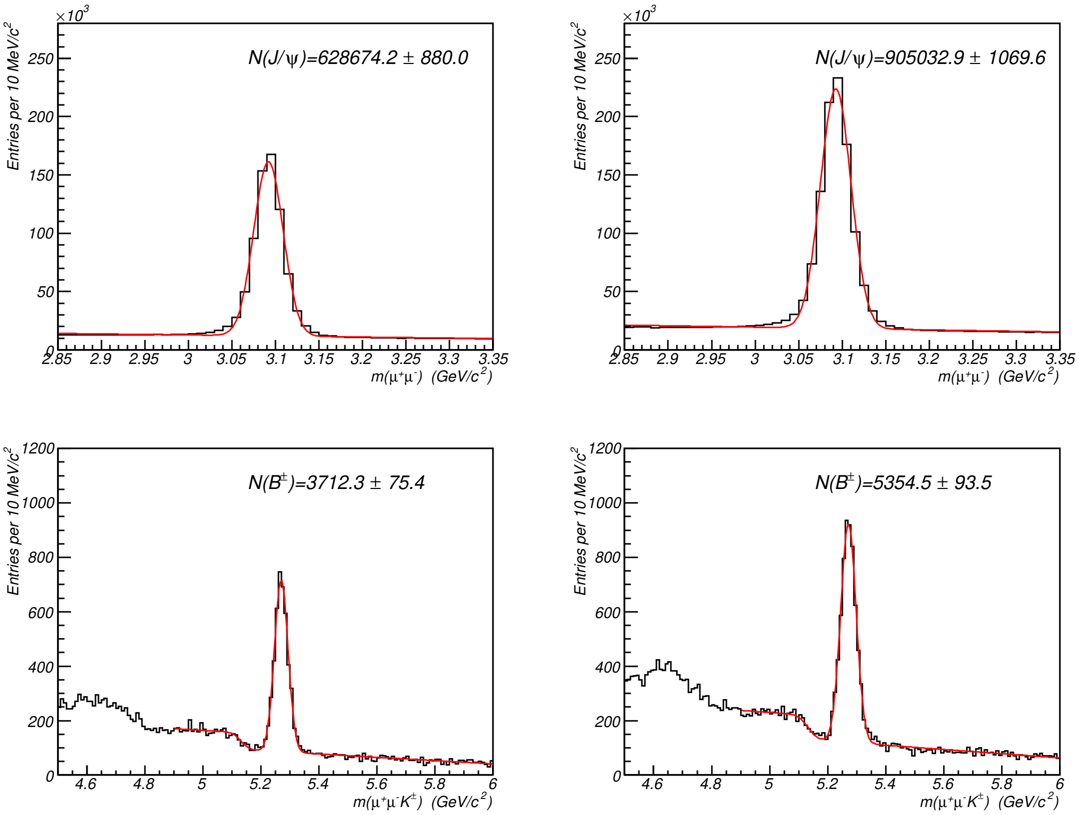

Figure 27: Invariant mass distributions containing $J/\psi \to \mu^+\mu^-$ (top) and $B^+ \to J/\psi K^\pm$ signals (bottom) reconstructed in `jpmm0d,0h,0j` (left) and in `jpmm0m` datasets (right).

Equations 24 and 25 enumerate the ratios of $J/\psi K^{\pm}$ to J/ψ yields in the two datasets and the ratio these two ratios.

$$\frac{N(J/\psi K^{\pm})}{N(J/\psi)} = \begin{cases} 0.005905 \pm 0.000120 & \texttt{jpmm0d,0h,0j} \\ 0.005916 \pm 0.000103 & \texttt{jpmm0m} \end{cases} \quad (24)$$

$$\frac{N_{\texttt{0m}}(J/\psi K^{\pm})/N_{\texttt{0m}}(J/\psi)}{N_{\texttt{0d,0h,0j}}(J/\psi K^{\pm})/N_{\texttt{0d,0h,0j}}(J/\psi)} = 1.002 \pm 0.027 \quad (25)$$

Given the limited statistics, there appears to be no evidence that the track reconstruction efficiency is lower in recent data.

5.3 Absolute XFT track finding efficiency

The kaon from $B^+ \to J/\psi K^+$ decays, selected with no restrictions beyond those used to form the `defTracks` collection, is used to measure the probability that an unbiased track that satisfies p_T and geometric selection cuts, will be associated with an XFT track. For compatibility with the muon triggers, the kaon is required to have $p_T > 3$ GeV/c and to satisfy the XFT fiducial cuts

$$\begin{aligned} |z(R_{SL})| &> 1.5 \text{ cm} \quad \text{at radii of axial superlayers} \\ |z(R = 136 \text{ cm})| &< 155 \text{ cm.} \end{aligned}$$

Figure 28 shows the fitted signals from $B^{\pm} \to J/\psi K^{\pm}$ when the kaon fails to be matched with an XFT track (left) or when it does satisfy the matching criteria (right). The XFT matching efficiency is calculated from these yields and is found to be[1]

$$\epsilon_{\mathrm{XFT}} = 0.9648 \pm 0.0039. \quad (26)$$

The efficiencies measured in earlier data (`jpmm0d,0h,0j`) and in later data (`jpmm0m`) are also seen to be consistent:

$$\epsilon_{\mathrm{XFT}} = \begin{cases} 0.9649 \pm 0.0049 & \texttt{jpmm0d,0h,0j} \\ 0.9646 \pm 0.0055 & \texttt{jpmm0m} \end{cases} \quad (27)$$

[1]This result is actually identical to Equation 12.

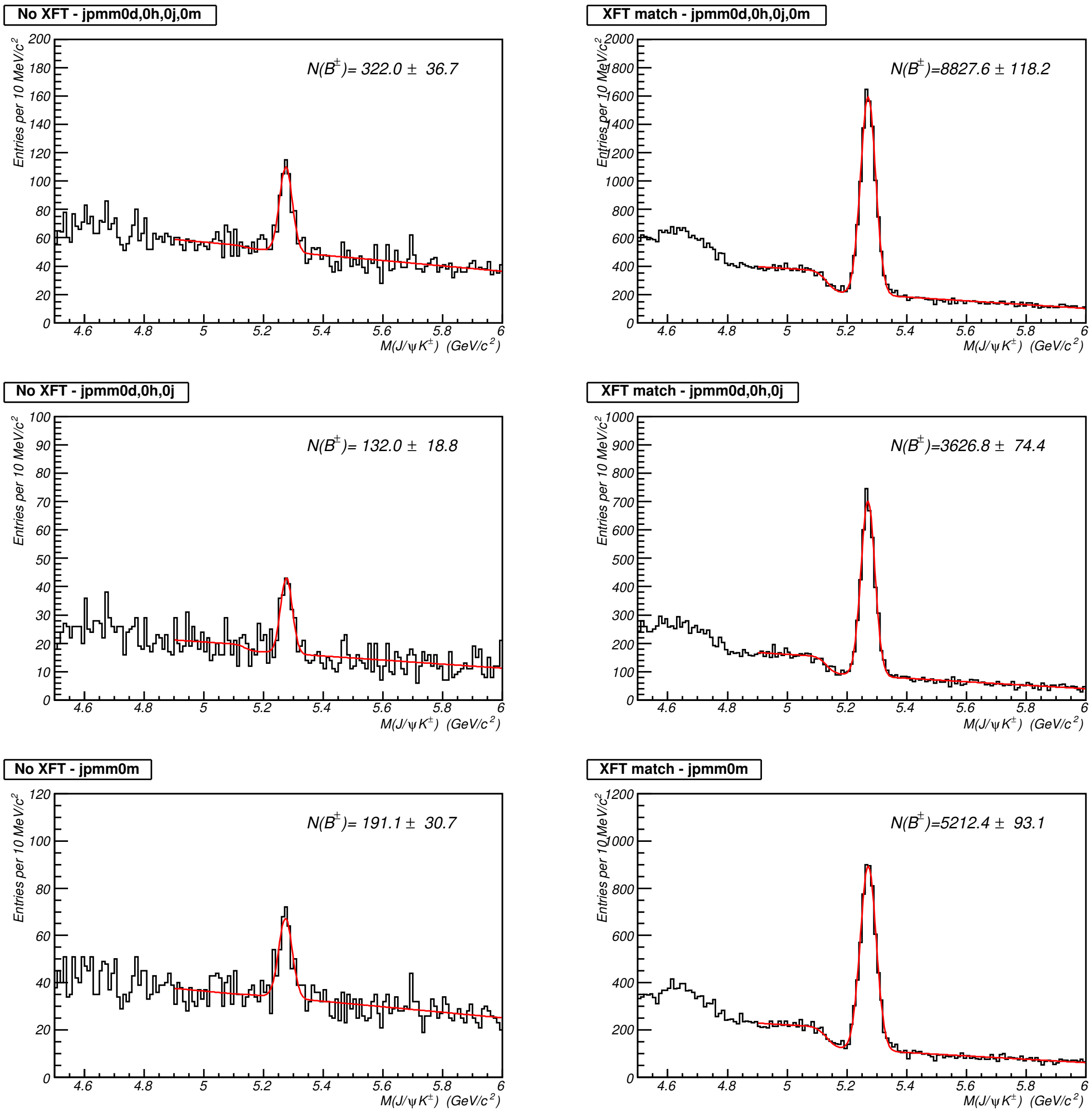

Figure 28: Invariant mass distributions of $J/\psi K^{\pm}$ candidates in which the kaon either fails to be matched with an XFT track (left) or is matched (right).

6 Angular Distribution Analysis

The analysis of the angular distribution of the final state muons is carried out in the rest-frame of the di-muon system where the polar angles, θ and φ, are defined with respect to a suitable coordinate system. The shape of the underlying angular distribution is parameterized and the Monte Carlo samples are used to calculate the mapping of this underlying distribution to the measured distribution, which is modified by the fiducial and kinematic acceptance as well as the trigger and reconstruction efficiencies.

In this analysis, the muon angular distribution is measured in discrete ranges of di-muon invariant mass. However, such a selection yields a sample containing both $\Upsilon(nS) \to \mu^+\mu^-$ signal events and a background component that cannot be ignored. Therefore, the analysis of $\Upsilon(nS)$ polarization relies entirely on obtaining an accurate description of the background polarization in mass regions containing the signals of interest. This is complicated by the fact that the kinematic properties of the background vary with invariant mass and with the di-muon p_T which makes it difficult to extrapolate background properties from the signal sidebands into the signal regions themselves.

The following sections describe some of the general properties of the continuum di-muon background followed by a description of a toy model that simulates correlated $b\bar{b}$ production and is shown to reproduce the features observed in the background. The suggestion that the background is dominated by semi-leptonic decays of b-hadrons motivates the selection of a sub-sample of events that is dominated by $b\bar{b}$ production and which is shown to have very similar polarization to the inclusive di-muon sample in the same range of invariant mass. Thus, the $\Upsilon(nS)$ polarization analysis is carried out by performing a simultaneous fit to the signal and background samples so as to accurately account for the polarization properties of the background.

6.1 Background properties

Figure 29 shows the ranges of di-muon invariant mass that are analyzed independently. Their boundaries are chosen so as to be of approximately equal width, while containing the $\Upsilon(nS)$ signals within individual bins. Figure 30 shows an example of the angular distribution projected onto the $\cos\theta$ axis in the S-channel helicity frame for the first mass bin, the mass bin containing the $\Upsilon(1S)$ signal and the last mass bin. If all properties of the background varied linearly with invariant mass, then it would be a straight forward to constrain the functional form of the background polarization from the signal side-bands and subtract from the signal bins, or otherwise account for its presence statistically. However, in some p_T ranges, particularly at lower p_T, this is not the case.

The peaking near $\cos\theta \approx \pm 1$, seen in the highest mass bin, is a particular feature that is produced by a combination of background muon sources, trigger selection bias and kinematic restrictions used in the analysis. Figure 31 shows that at high mass, the events that contribute to the sample are sculpted by the p_T restriction and that a significant component of the sample at high mass has maximal momentum asymmetry. This feature is present in this particular p_T range mainly in the high mass region which complicates the description of the di-muon background composition.

Insight into the nature of the di-muon background can be gained by supposing that it is dominated by real muons from semi-leptonic decays of b-hadrons. The properties of events with fake muons is expected to be similar since one muon is likely to be real, produced in semi-leptonic b-decay, while a fake is likely to be a track from the b-decay on the opposite side of the event. Because the triggerable fraction of $b\bar{b}$ events generated using a NLO or LO+parton shower model is very low, it becomes problematic to generate large enough samples with which to model the background. Instead, a simple toy Monte Carlo was developed that reproduces some of the important distributions from the analysis of $b\bar{b}$ correlation[8].

The specific procedure used to generate di-muons in this way was the following:

- generate $p_T(b)$, $y(b)$, $\phi(b)$,

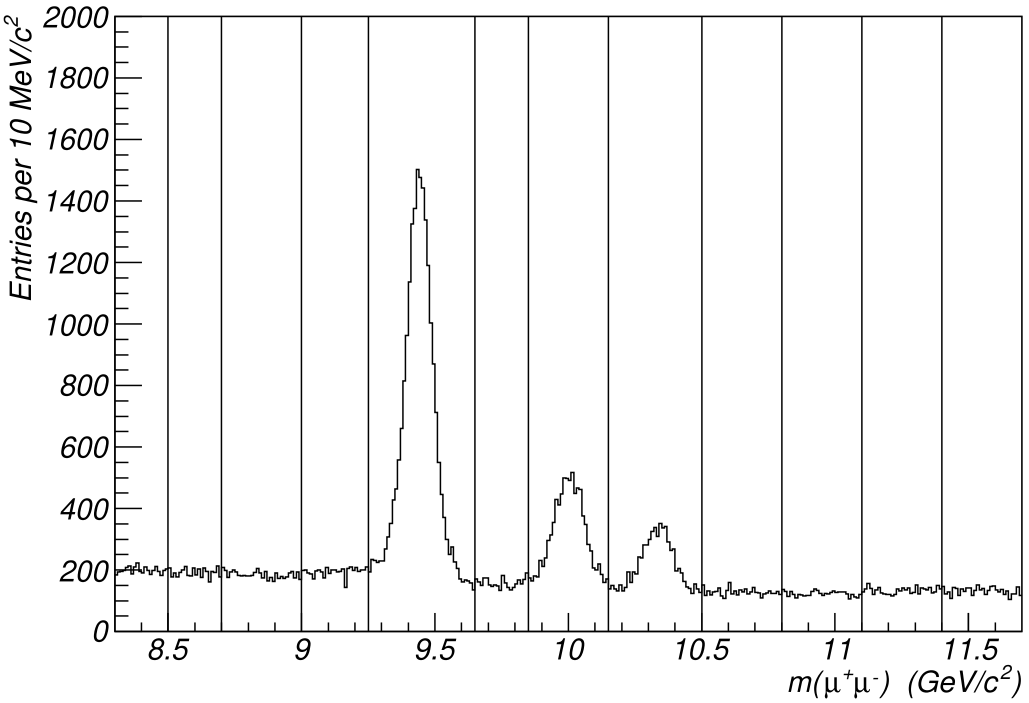

Figure 29: Example of a di-muon invariant mass distribution ($6.5 < p_T < 8.5$ GeV/c^2) showing binning used to analyze their angular distributions.

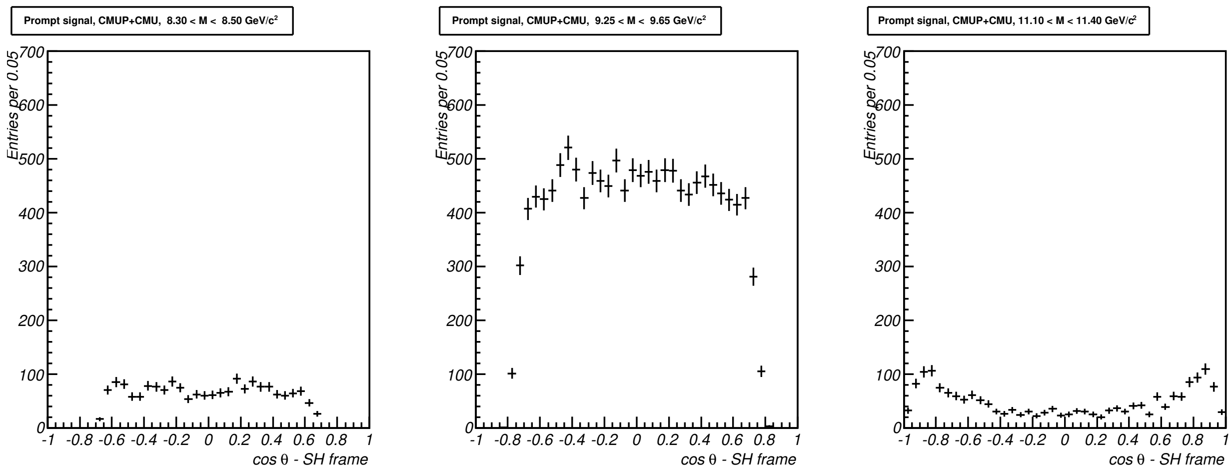

Figure 30: Examples of projected angular distributions for background (left and right) and $\Upsilon(1S)$ signal (center) mass ranges. Di-muons in this selection have $6.5 < p_T < 8.5$ GeV/c^2.

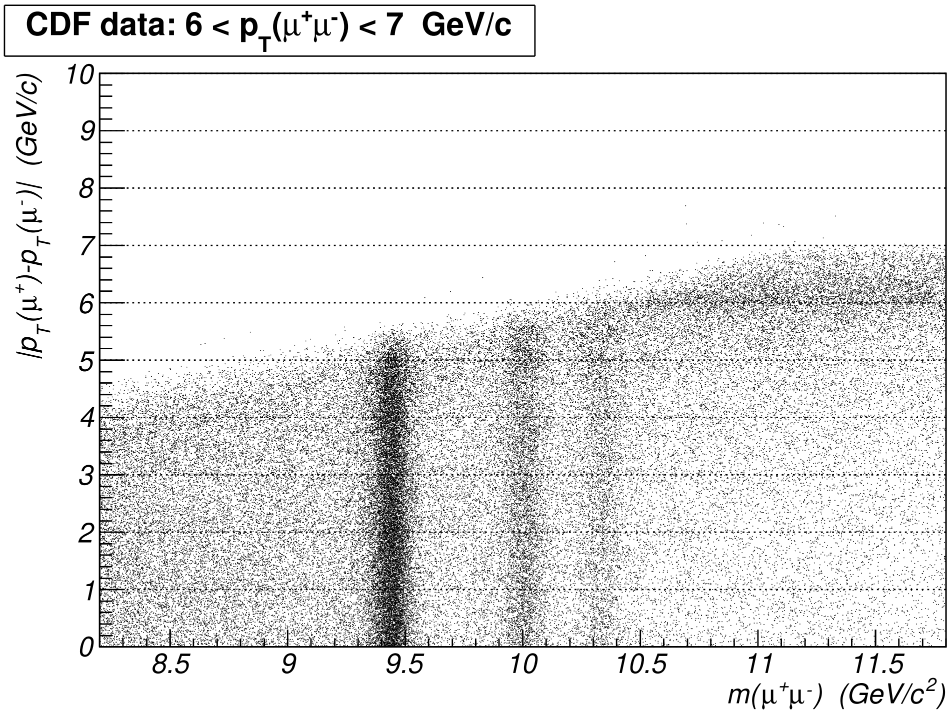

Figure 31: Muon p_T-difference as a function of di-muon invariant mass, for low-p_T di-muons.

- generate $\Delta\phi(\bar{b})$, $\Delta y(\bar{b})$, $A_{\mathrm{p_T}} = (p_T(\bar{b}) - p_T(b))/(p_T(\bar{b}) + p_T(b))$,
- generate $\vec{p}(B)$ and $\vec{p}(\overline{B})$ using Peterson fragmentation with $\epsilon_b = 0.0035$,
- generate isotropic decay angles and $E_{\mu^\pm}$ in rest frames of B and $\overline{B}$,
- boost $\mu^\pm$ to lab frame,
- apply loose cuts on $p_T(\mu^\pm)$ and $y(\mu^\pm)$,
- perform full event simulation, reconstruction and analysis.

The b-quark rapidity is generated uniformly between -1 and 1, while the distributions of $p_T(b)$, $\Delta\phi(\bar{b})$, $\Delta y(\bar{b})$, A_{p_T} and $E_{\mu^\pm}$ were generated using empirical functions that approximate those obtained using Pythia. Figure 32 shows these distributions which can be directly compared with those in the Monte Carlo study of $b\bar{b}$ correlations [8].

Figure 33 shows the distribution of the muon p_T-difference as a function of invariant mass from events from the toy Monte Carlo sample that satisfy the CMUP+CMU trigger requirements. The same structures visible in Figure 31, namely the enhancement at high mass and high Δp_T, can be seen in the toy Monte Carlo sample. This suggests that at least the qualitative behavior of the $b\bar{b}$ background component in the data can be studied using this toy Monte Carlo sample. Furthermore, it suggests that the continuum background in the di-muon sample is largely composed of muons from $b\bar{b}$ production. Because the accumulation of events with large p_T asymmetry at higher values of di-muon mass tends to peak at high values of $|\cos\theta|$ in the S-channel helicity frame, some of this component is removed by imposing the requirement that $|p_T(\mu^+) - p_T(\mu^-)| > p_T(\mu^+\mu^-) - 1/2$ GeV$/c$. This introduces some additional inefficiency for $\Upsilon(nS)$ signals at low p_T, but has no effect for $p_T > 7$ GeV$/c$.

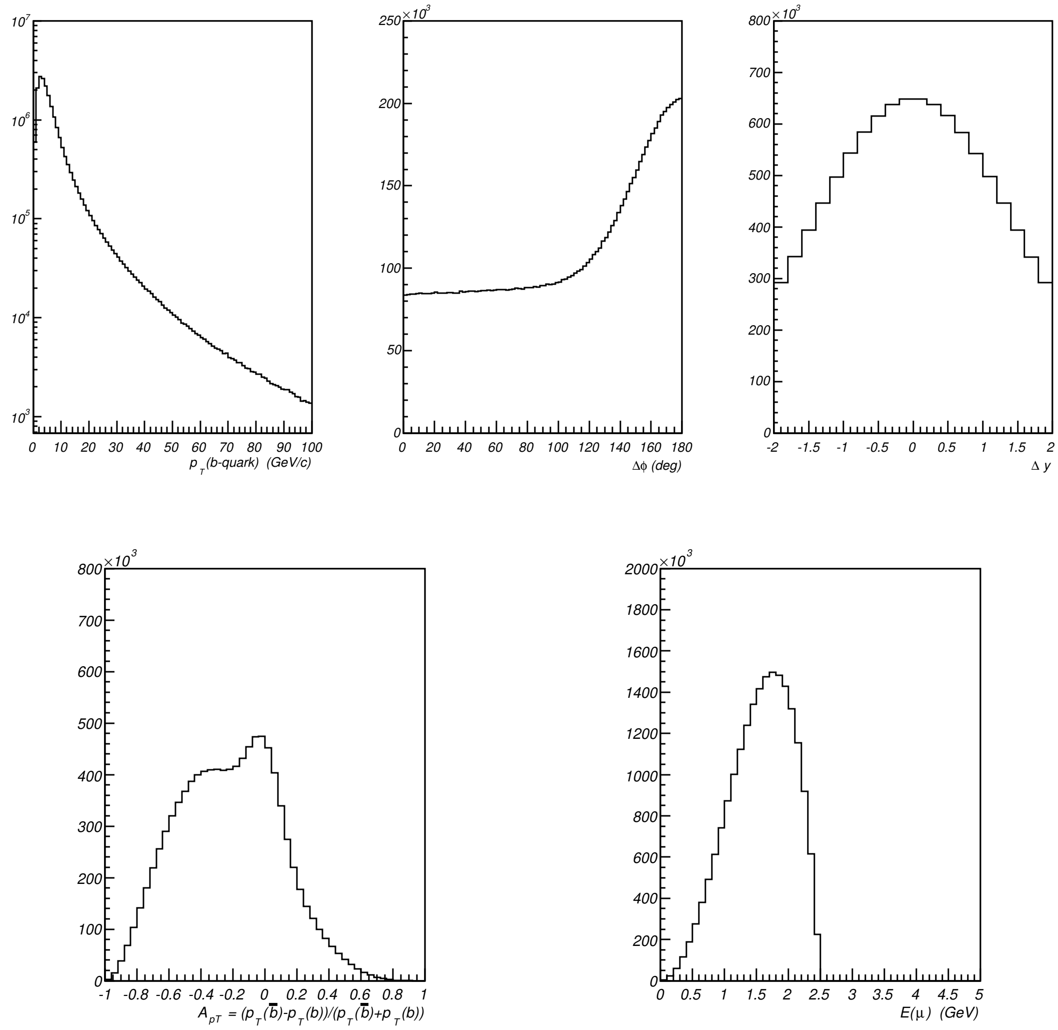

Figure 32: Distributions used to generate correlated $b\overline{b}$ toy Monte Carlo samples.

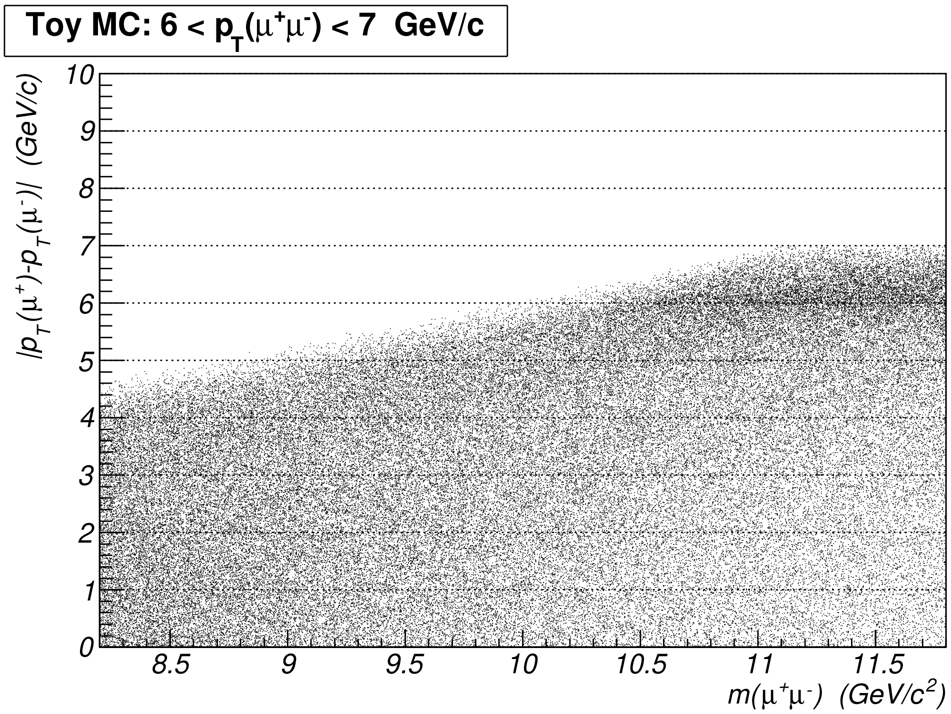

Figure 33: Toy Monte Carlo muon p_T-difference as a function of di-muon invariant mass, for low-p_T di-muons.

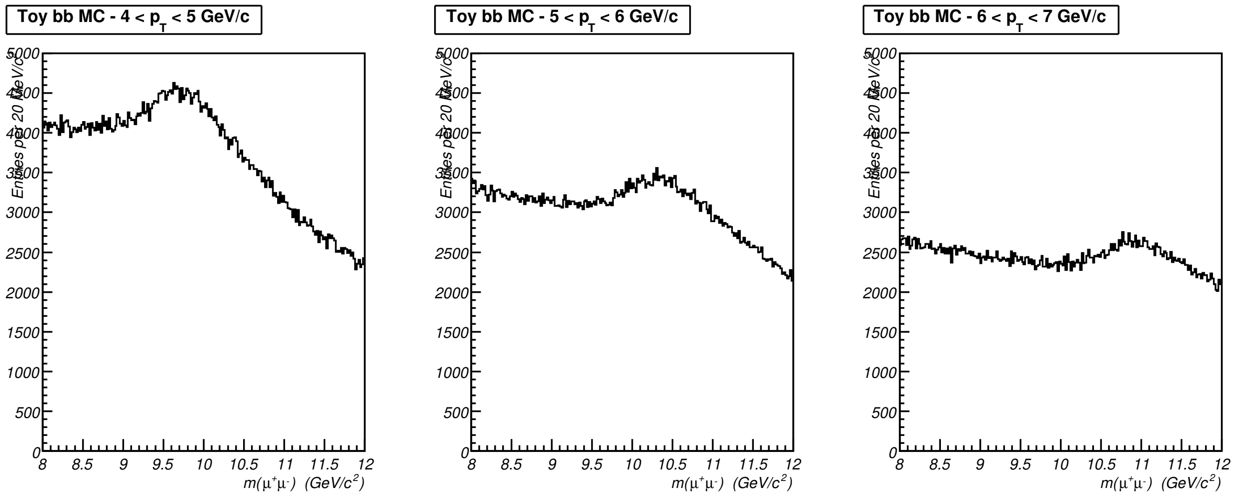

Figure 34: Toy Monte Carlo di-muon invariant mass distributions in three different p_T ranges illustrating the evolution of the mass structures with p_T.

6.2 Displaced track sub-sample

Given that correlated $b\bar{b}$ production may be the dominant source of background, a background-enhanced sample can be obtained by requiring that at least one track has at least three silicon hits and has an impact parameter larger than 150 μm, measured with respect to the average beam position. Figure 35 compares the the di-muon invariant mass distributions obtained using this requirement to the complementary sample, which contains the $\Upsilon(nS)$ signals.

In the angular distribution analysis, the displaced track sample will be treated as a background-enhanced sample, but there is still a small $\Upsilon \to \mu^+\mu^-$ component that remains. The fraction of signal that is present in the displaced track sample is assumed to be the same for the three $\Upsilon(nS)$ resonances and is measured using a simultaneous binned likelihood fit to the invariant mass distributions of the prompt and displaced track samples. In these fits, which are performed separately for the CMUP+CMU and CMUP+CMX samples, the mass splittings are constrained to the well-measured PDG values, and the signals are parameterized as a single Gaussian with common mass shift and resolution. The background is parameterized as either an exponential function or a gamma distribution at lower p_T. The ratio of the non-displaced to displaced background is parameterized as a quadratic function in the di-muon invariant mass. Based on the event yield in the displaced track sample, this ratio is used to predict the amount of background under the $\Upsilon(nS)$ signals in the prompt sample when analyzing the angular distributions. To avoid the possibility of the $\Upsilon(1S)$ radiative tail biasing the prompt scale factor, the region of invariant mass from 9.00 to 9.25 GeV/c^2 is removed from the fit to the prompt component.

The prompt scale factor is parameterized as a second-order polynomial so that it can be evaluated at the masses of $\Upsilon(nS)$ signal bins. The uncertainties in the fitted coefficients are propagated to calculate the uncertainty in the prompt scale factor as a function of invariant mass. Figure 36 shows the $\pm 1\sigma$ confidence intervals for the prompt scale factor in one $p_T(\Upsilon)$ bin.

Figure 37 shows that the displaced track sample provides a reasonable description of the angular distribution in the prompt sample in both low- and high-mass regions. The quality of the assumption that the displaced track sample provides a good description of the angular distribution of the background in the prompt sample is evaulated by calculating a goodness-of-fit statistics in each bin of p_T and invariant mass. Specifically, the agreement is quantified using

$$\hat{\chi}^2 = \frac{1}{N}\sum_{i=1}^{N}\frac{(p_i - d_i \cdot s_p(m))^2}{p_i + d_i \cdot s_p(m)^2} \tag{28}$$

which sums over bins for which $p_i > 2$ and $d_i > 2$. This is sort of like a χ^2 per degree of freedom statistic, but no attempt has been made to accurately account for the number of degrees of freedom in the comparison. Nevertheless, one expects $\hat{\chi}^2 \approx 1$ for statistically compatible samples. Figures 38 and 39 show the comparison for all p_T and mass bins analyzed, with the mass bins containing the $\Upsilon(nS)$ signals removed.

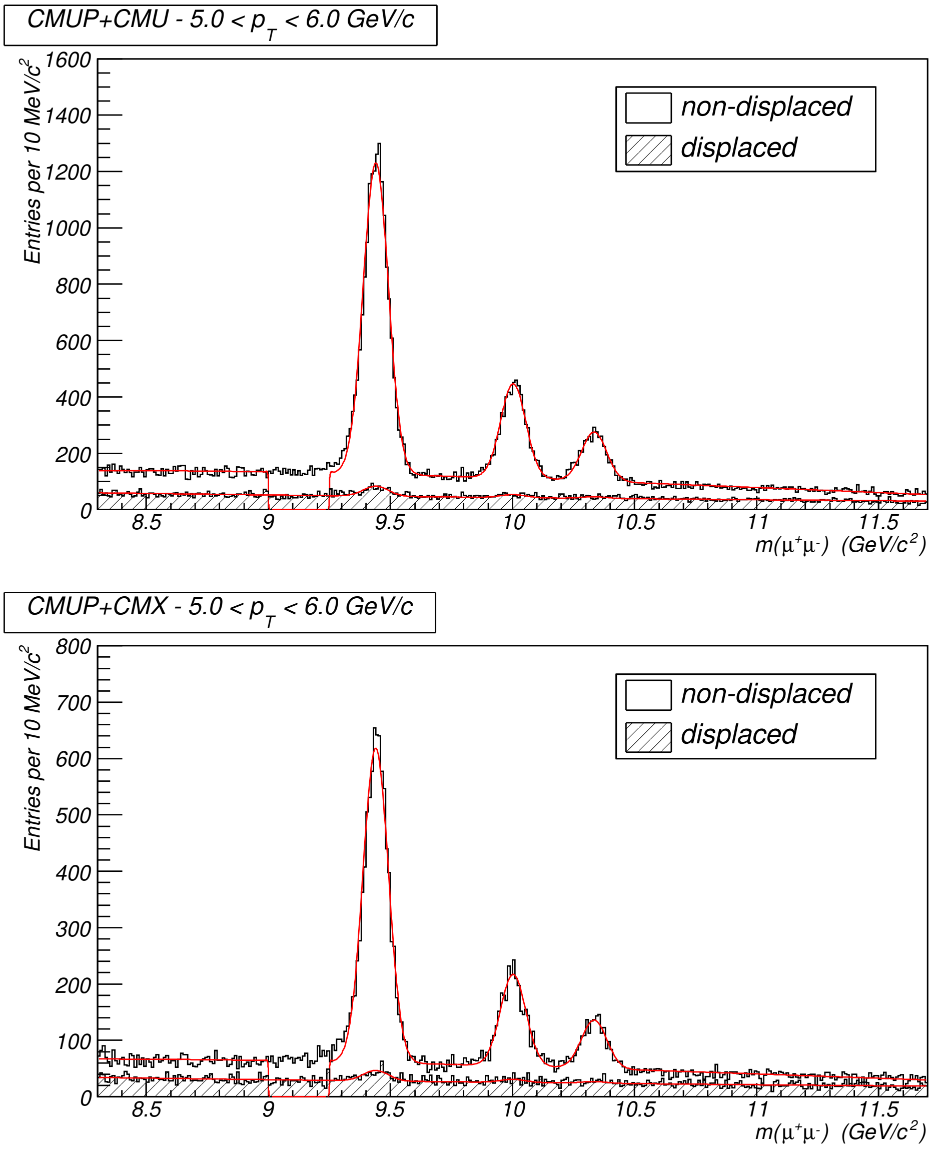

Figure 35: Example of the di-muon invariant mass distributions obtained by requiring at least one displaced track (at least 3 r-φ silicon hits, $|d_0| > 150$ μm – unhatched histogram) and the complementary sample (hatched histogram).

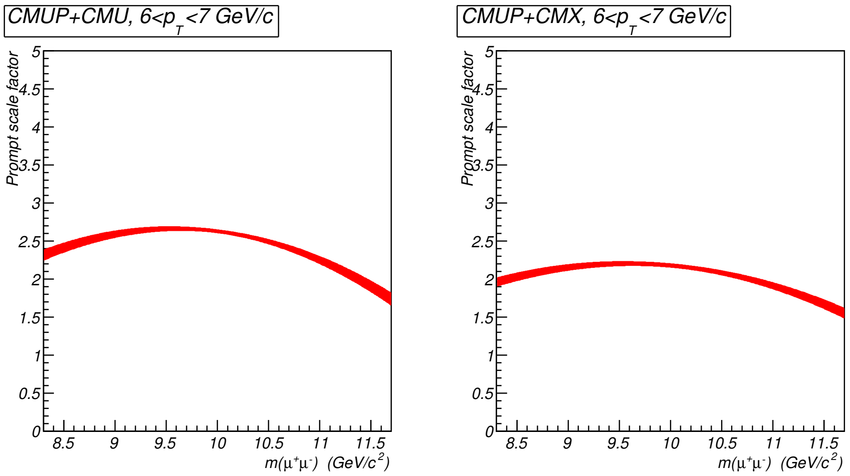

Figure 36: One-sigma confidence interval for the prompt scale factor measured for di-muon backgrounds in the CMUP+CMU (left) and CMUP+CMX (right) samples.

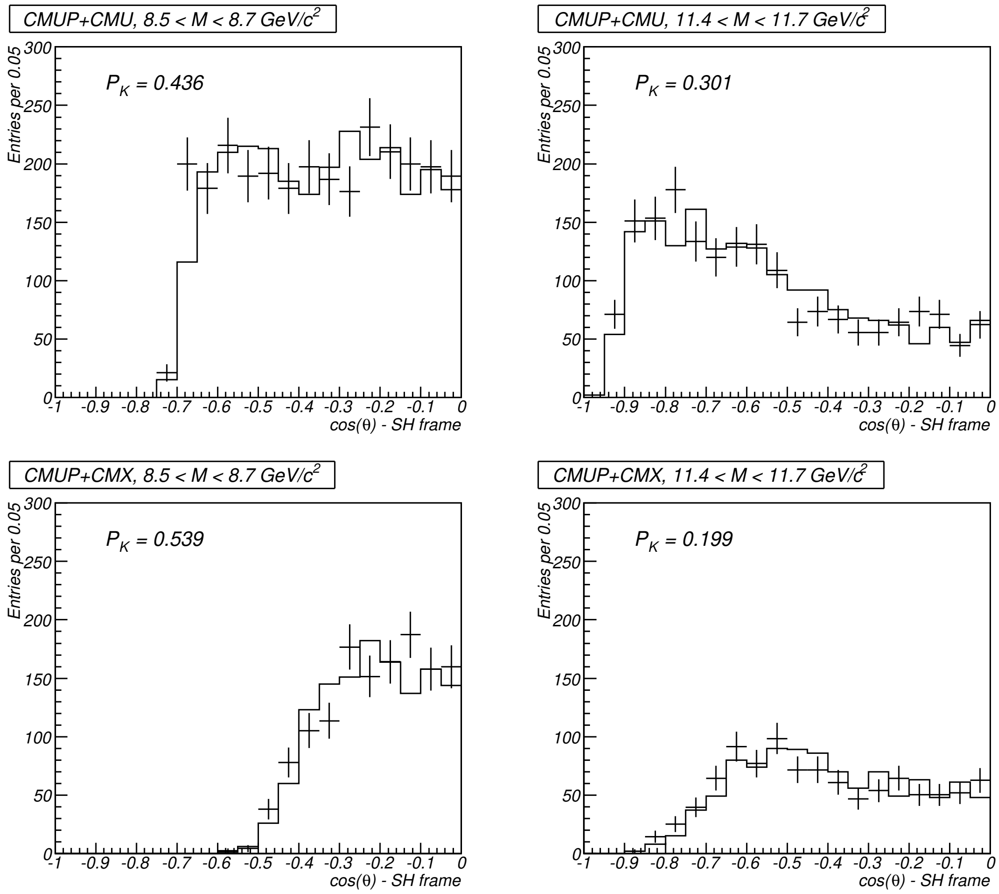

Figure 37: Distribution of $\cos\theta$, measured in the S-channel helicity frame, for the displaced track sample (error bars) and the complementary sample (histogram) in the low-mass and high-mass regions of the CMUP+CMU and CMUP+CMX trigger samples. P-values for the Kolmogorov statistic that quantifies the compatibility of each comparison are indicated on each plot. This comparison is shown for $6 < p_T < 7$ GeV/c.

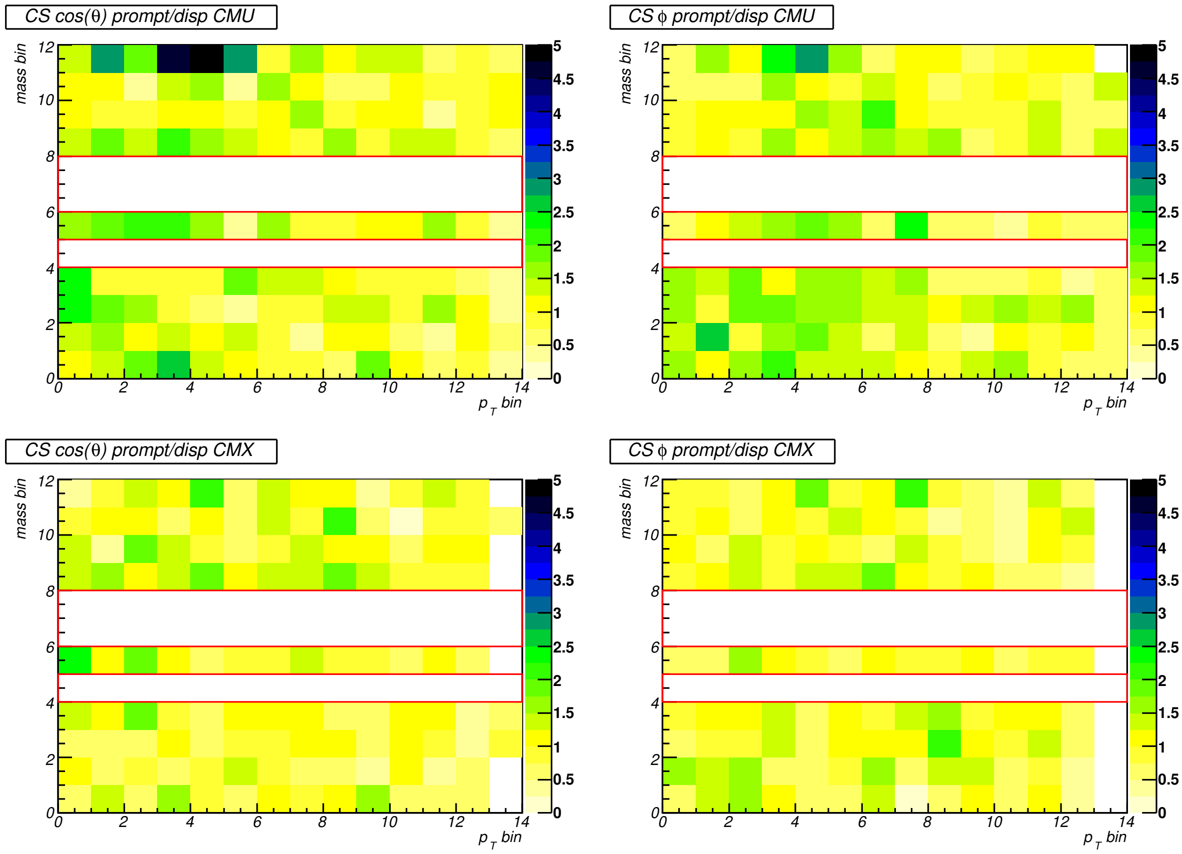

Figure 38: Goodness-of-fit statistic calculated for the $\cos\theta$ and φ projections for all p_T and mass bins in the Collins-Soper frame.

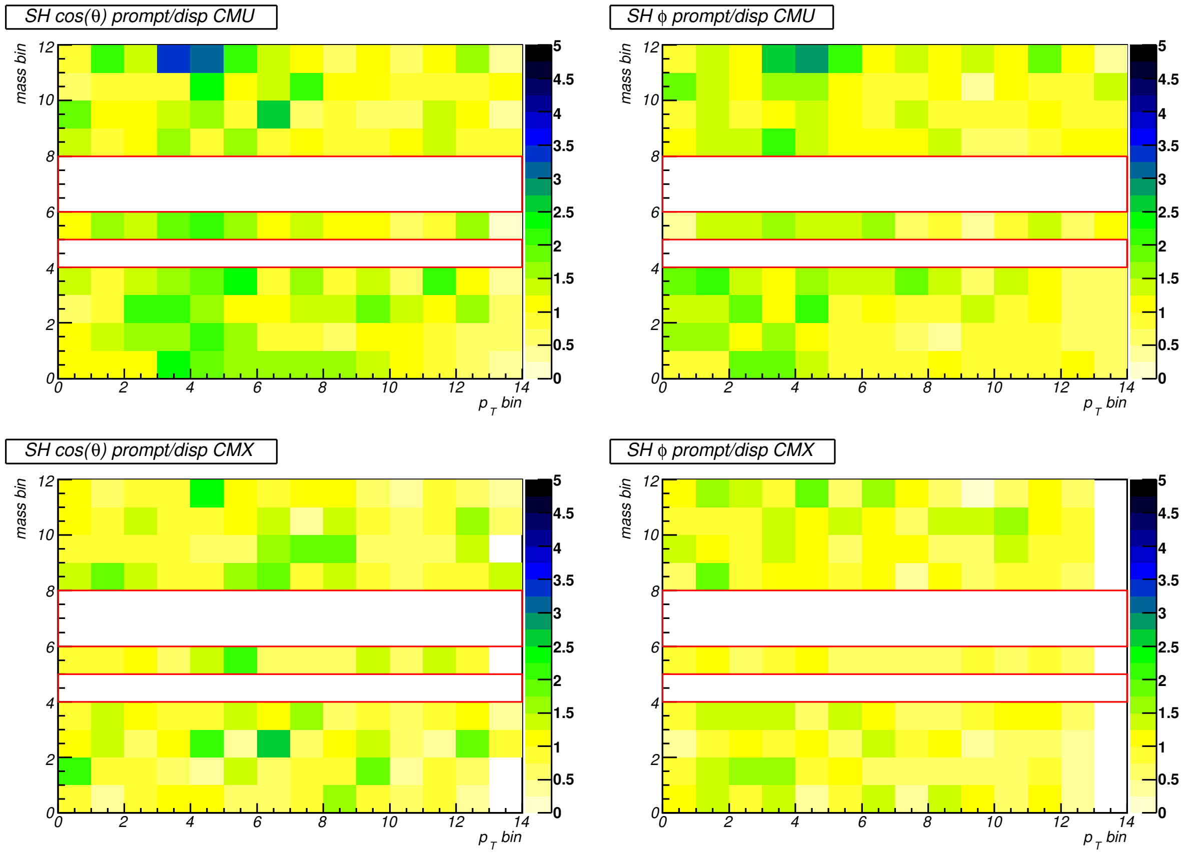

Figure 39: Goodness-of-fit statistic calculated for the $\cos\theta$ and φ projections for all p_T and mass bins in the S-channel helicity frame.

6.3 Fits to angular distributions

In this analysis, the angular distribution of the positive muon measured in a given reference frame is characterized by the coefficients in a harmonic expansion of the angles (θ, φ). For the decay of a spin-1 resonance, the angular distribution is given by Equation 1 and although other sources of di-muons might be described by a similar function, this is not necessarily the case. The effective number of events in a particular bin of $(\cos\theta, \varphi)$ can be increased by exploiting the 4-fold symmetry that leads to Equation 2. This section explores the justification for this procedure in more detail.

The number of events expected in angular bin (i, j) is a product of the cross section, the angular distribution and the acceptance:

$$\mu_{i,j} = \sigma \cdot w(\cos\theta_i, \varphi_j) \cdot \mathcal{A}_{i,j}. \tag{29}$$

where $w(\cos\theta_i, \varphi_j)$ is the angular distribution in Equation 1. When exploiting the expected 4-fold symmetry, we can write

$$\begin{aligned}\mu'_{i,j} \quad = \sigma \cdot \Big(\quad & w(\cos\theta_i, \varphi_j) \cdot \mathcal{A}_{i,j} + \\ & w(\cos\theta_i, \varphi_{M-j+1})\mathcal{A}_{i,M-j+1} + \\ & w(\cos\theta_{N-i+1}, \varphi_{M/2-j+1})\mathcal{A}_{N-i+1,M/2-j+1} + \\ & w(\cos\theta_{N-i+1}, \varphi_{M/2+j})\mathcal{A}_{N-i+1,M/2+j} \ \Big)\end{aligned} \tag{30}$$

where there are N bins in $\cos\theta$ and M bins in φ. Under the assumption that the acceptance satisfies

$$\mathcal{A}_{i,j} = \mathcal{A}_{i,M-j+1} = \mathcal{A}_{N-i+1,M/2-j+1} = \mathcal{A}_{N-i+1,M/2+j}, \tag{31}$$

Equation 30 will reduce to

$$\mu'_{i,j} = 4 \cdot \sigma \cdot w'(\cos\theta_i, \varphi_j) \cdot \mathcal{A}_{i,j} \tag{32}$$

where $w'(\cos\theta, \varphi)$ is the angular distribution given by Equation 2. Therefore, the justification for combining bins in this way rests on demonstrating that the acceptance does indeed satisfy these symmetry conditions.

We test this hypothesis by calculating the acceptance with binomial uncertainties for sets of four bins, fit a constant function to the set of four points and examine the distribution of χ^2. Assuming the statistics in each bin are large enough that binomial errors are appropriate, this should be a χ^2 distribution with three degrees of freedom. Figure 40 shows the distribution of the P-values for these fits with different restrictions imposed on the minimum number of events in any bin in the numerator of the acceptance. The acceptance distributions analyzed in this figure cover the 14 ranges of p_T, the background acceptances in the 12 ranges in invariant mass in both CMUP+CMU and CMUP+CMX trigger paths and the three $\Upsilon(nS)$ signal acceptances for both trigger paths. This figure supports the hypothesis that the four acceptance bins are drawn from an identical underlying distribution. The slight peaking at low P-values appears to be an artifact of approximating the Gaussian uncertainty in each bin by the binomial error, which becomes increasingly accurate as the minimum number of events in any acceptance bin is increased. A constant function fit to the distribution obtained with $n_{\min} > 50$ gives $\chi^2/\text{d.o.f.} = 21.2/19$, which has a P-value of 32.4%. Based on this analysis, we find no reason to doubt the assumption that acceptance satisfies the symmetry relations used in the analysis of the angular distributions.

6.4 Background angular distribution

Angular distributions of di-muons in the mass regions that do not contain the $\Upsilon(nS)$ signal peaks are analyzed by performing a simultaneous fit to the displaced track sample and the complimentary sample, assuming their angular distributions are the same. The angular distribution is parameterized by Equation 2. However, since the background does not arise from such a decay, no restrictions

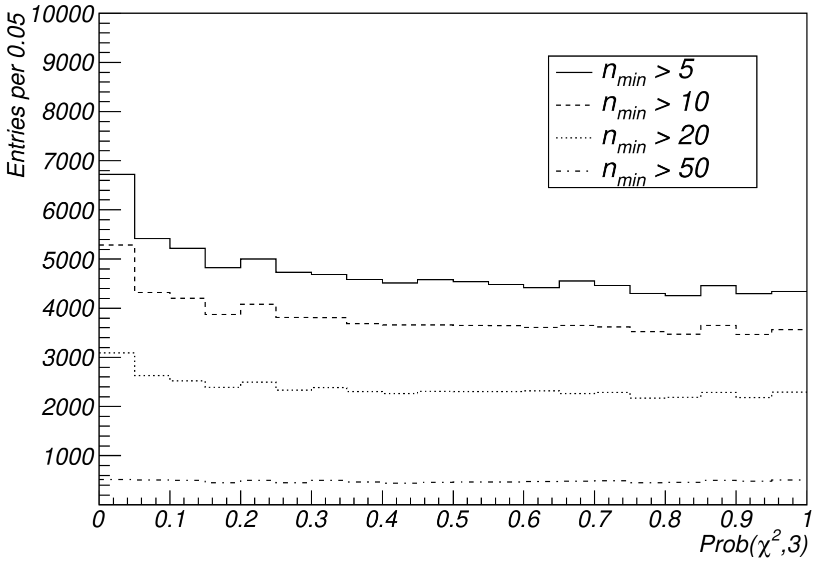

Figure 40: Distribution of the P-values of the fits to the acceptance calculated in four bins with assumed symmetry in $(\cos\theta, \varphi)$ under the hypothesis that they have a χ^2 distribution with three degrees of freedom. The four histograms correspond to different restrictions on the minimum number of events required in any of the acceptance bins analyzed.

are imposed on the parameters λ_θ, λ_φ and $\lambda_{\theta\varphi}$ and they are allowed to vary beyond the range that is physically allowed for a spin-1 decay. In addition, the event yields in the CMUP+CMU and CMUP+CMX trigger samples are effectively treated as free parameters in the fit. To be specific, for each trigger sample, the number of entries expected in a bin with angular variables $(\cos\theta_i, \varphi_j)$ is expressed

$$\mu_d(i,j) = L \cdot \sigma_d \cdot w(\cos\theta_i, \varphi_j) \cdot \epsilon_b(i,j) \quad (33)$$

$$\mu_p(i,j) = L \cdot s_p\sigma_d \cdot w(\cos\theta_i, \varphi_j) \cdot \epsilon_b(i,j) \quad (34)$$

$$(35)$$

in which L is the effective integrated luminosity, $w(\cos\theta_i, \varphi_j)$ is the angular distribution from Equation 2, $\epsilon_b(i,j)$ is the product of acceptance and efficiency for background events continuously distributed over the mass range of interest and are calculated using the Monte Carlo. The scale factor, s_p, relates the yield in the prompt sample to the displaced-track sample. The fit is performed simultaneously to the data from both CMUP+CMU and CMUP+CMX trigger paths, with a common set of parameters to describe the angular distribution. Figures 41 and 42 show a examples of the resulting fit projected onto the $\cos\theta$ axis.

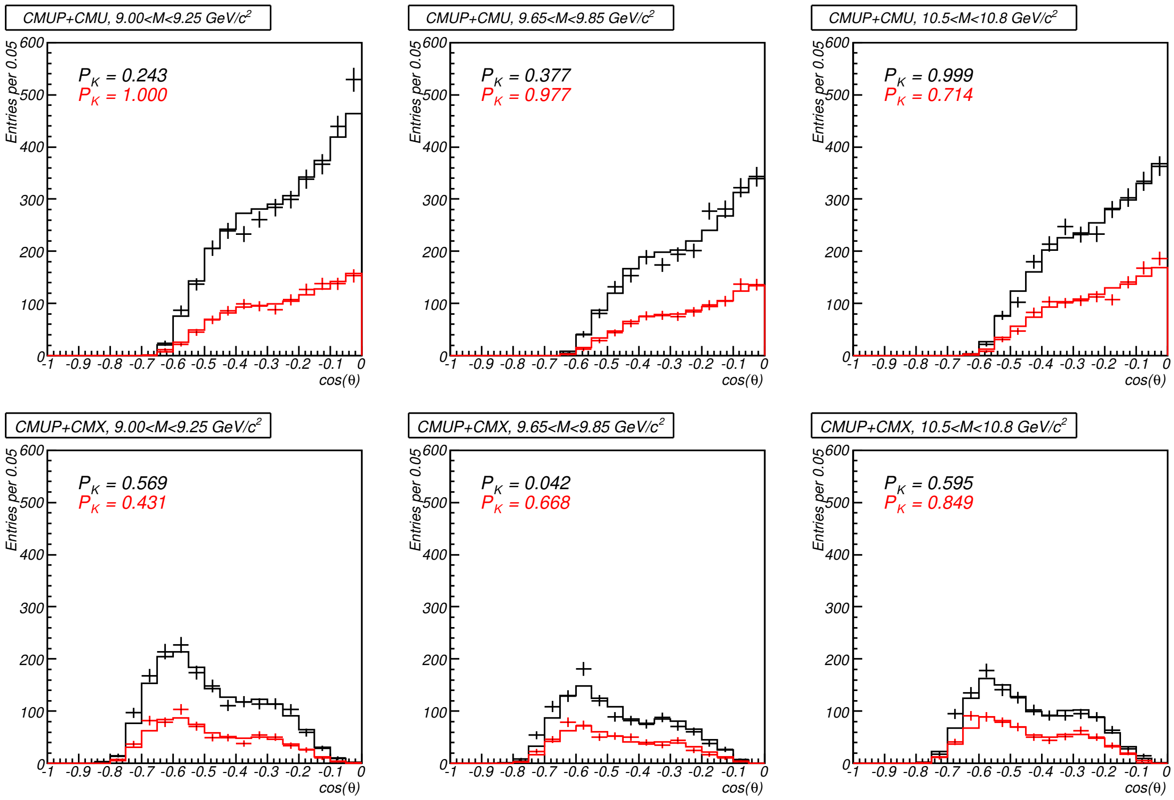

Figure 41: Angular distributions projected onto the $\cos\theta$ axis in the Collins-Soper frame for $6 < p_T < 7$ GeV/c. The displaced track sub-sample is in red and the complimentary sample is in black. The selected mass ranges correspond to the regions just below the $\Upsilon(1S)$ signal, between the $1S$ and $2S$ signals, and just above the $\Upsilon(3S)$ signal. The P-values of the Kolmogorov statistic calculated using the projected data and the best fit are shown in the corresponding color.

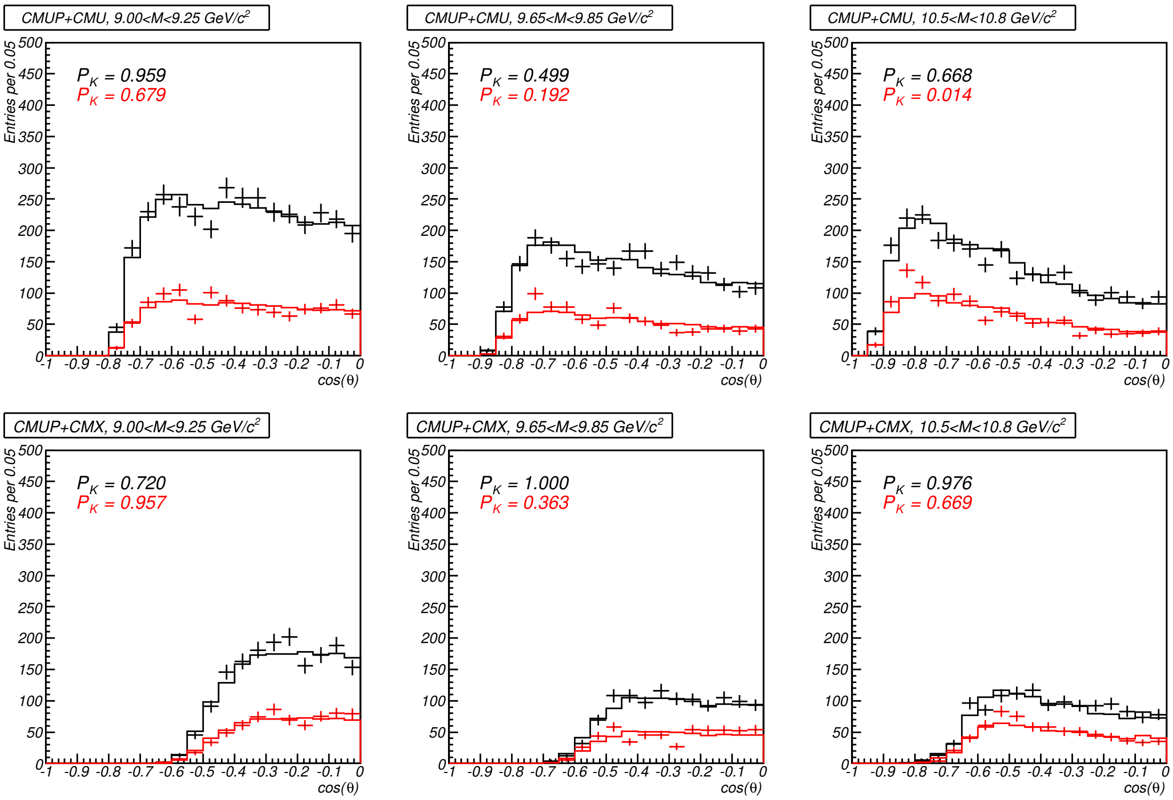

Figure 42: Angular distributions projected onto the $\cos\theta$ axis in the S-channel helicity frame for $6 < p_T < 7$ GeV/c. The displaced track sub-sample is in red and the complimentary sample is in black. The selected mass ranges correspond to the regions just below the $\Upsilon(1S)$ signal, between the $1S$ and $2S$ signals, and just above the $\Upsilon(3S)$ signal. The P-values of the Kolmogorov statistic calculated using the projected data and the best fit are shown in the corresponding color.

6.5 Fits to signal regions

The angular distribution of $\Upsilon(nS)$ signal events is determined from a simultaneous fit to the displaced-track sample, which is dominated by background, and the complementary sample, which contains most of the $\Upsilon(nS)$ signal. The background level in the non-displaced sample is constrained by the cross section of the displaced sample and the prompt scale factor which is calculated from the simultaneous fits to invariant mass distribution of the prompt- and displaced-track samples. The scale factor is parameterized as a second-order polynomial and is evaluated at the centers of the signal mass bins, along with the propagated uncertainties from the fit. This scale factor and its uncertainty is used as a Gaussian constraint when calculating the expected event yields in each angular bin. For the mass intervals containing the $\Upsilon(nS)$ signals, these expected yields are expressed

$$\mu_d(i,j) = L \cdot (\sigma_d \cdot w_b(\cos\theta_i, \varphi_j) \cdot \epsilon_b(i,j) + \sigma_{nS} \cdot (1 - f_p) \cdot w_s(\cos\theta_i, \varphi_j) \cdot \epsilon_{nS}(i,j)) \quad (36)$$
$$\mu_p(i,j) = L \cdot (s_p \sigma_d \cdot w_b(\cos\theta_i, \varphi_j) \cdot \epsilon_b(i,j) + \sigma_{nS} \cdot f_p \cdot w_s(\cos\theta_i, \varphi_j) \cdot \epsilon_{nS}(i,j)) \quad (37)$$

in which σ_d is the cross section for the displaced-track yield, $w_b(\cos\theta, \varphi)$ parametrizes the angular distribution of the background in terms of background parameters λ_θ, λ_φ and $\lambda_{\theta\varphi}$, and $\epsilon_b(i,j)$ is the product of acceptance and efficiency for background, as in Equations 33 and 34. The $\Upsilon(nS)$ signal component is parameterized using the cross section σ_{nS}, the angular distribution $w_s(\cos\theta, \varphi)$, and the product of acceptance and efficiency for the $\Upsilon(nS)$ signal in the mass range of interest. The parameter f_p represents the fraction of the $\Upsilon(nS)$ signal that is present in the prompt fraction, and is determined from the simultaneous fits to the invariant mass distributions in the prompt and displaced track samples.

The fit is performed simultaneously to the CMUP+CMU and CMUP+CMX trigger samples, with only the parameters that characterize the angular distributions in common. Separate signal cross sections accommodate the possibility of a non-uniform distribution of Υ production as a function of rapidity. The quality of the model is illustrated in Figures 44 and 43 which show the projections onto the $\cos\theta$ and φ axes for the two trigger paths in the Collins-Soper frame and the S-channel helicity frame. The quality of the fit in all p_T and mass bins is quantified by calculating a goodness-of-fit statistic

$$\hat{\chi}'^2 = \frac{1}{N} \sum_{i=1}^{N} \frac{(n_i - \mu_i)^2}{n_i + \sigma_{\mu_i}^2} \quad (38)$$

where n_i is the contents of a bin in the projected $(\cos\theta, \varphi)$ distribution, μ_i is the projection of the weighted template and σ_{μ_i} is its uncertainty. The sum is calculated using those bins for which $n_i > 4$. Figure 45 shows the goodness-of-fit statistic for projections calculated in the Collins-Soper frame, while Figure 46 shows the statistic claculated for projections in the S-channel helicity frame.

The fitted parameters in the angular distributions for the three $\Upsilon(nS)$ states in the Collins-Soper frame and the S-channel helicity frame are are listed in Tables 5–10. Their graphs, as functions of p_T are shown in Figures 47–49 in both reference frames.

Tables 11–13 show the comparisons of the derived quantity

$$\tilde{\lambda} = \frac{\lambda_\theta + 3\lambda_\varphi}{1 - \lambda_\varphi} \quad (39)$$

calculated in both reference frames for the three $\Upsilon(nS)$ states. These are plotted in Figure 50 for the three $\Upsilon(nS)$ resonances, comparing the values obtained in the Collins-Soper frame and the S-channel helicity frame.

Figure 51 shows the correlation between λ_θ and λ_φ for the three $\Upsilon(nS)$ states with $8 < p_T < 9$ GeV/c in the Collins-Soper frame, while Figure 52 shows their correlation in the S-channel helicity frame.

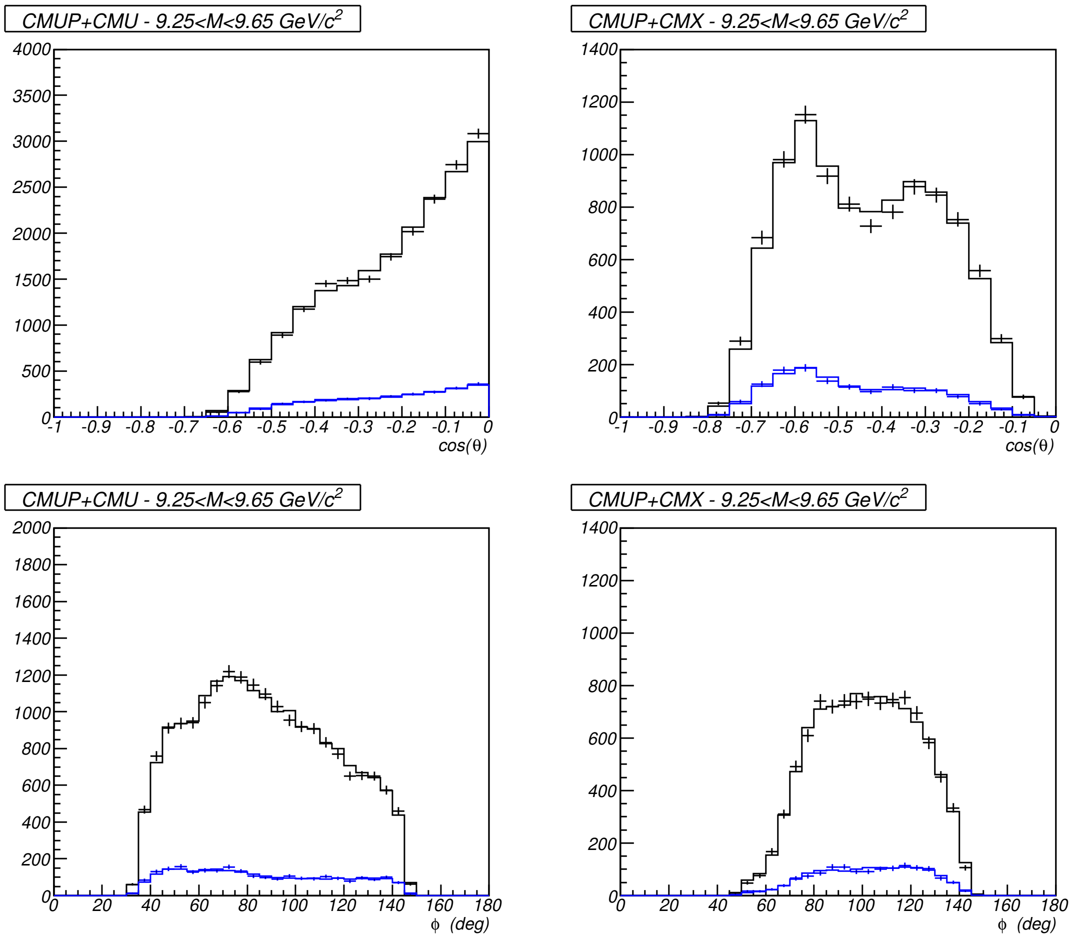

Figure 43: Projections of data (error bars) in the $\Upsilon(1S)$ signal mass range onto the $\cos\theta$ and φ axes in the Collins-Soper frame compared with the fit model (histogram) for CMUP+CMU and CMUP+CMX trigger paths. The displaced track sub-sample is shown in blue, while the complementary sample is shown in black.

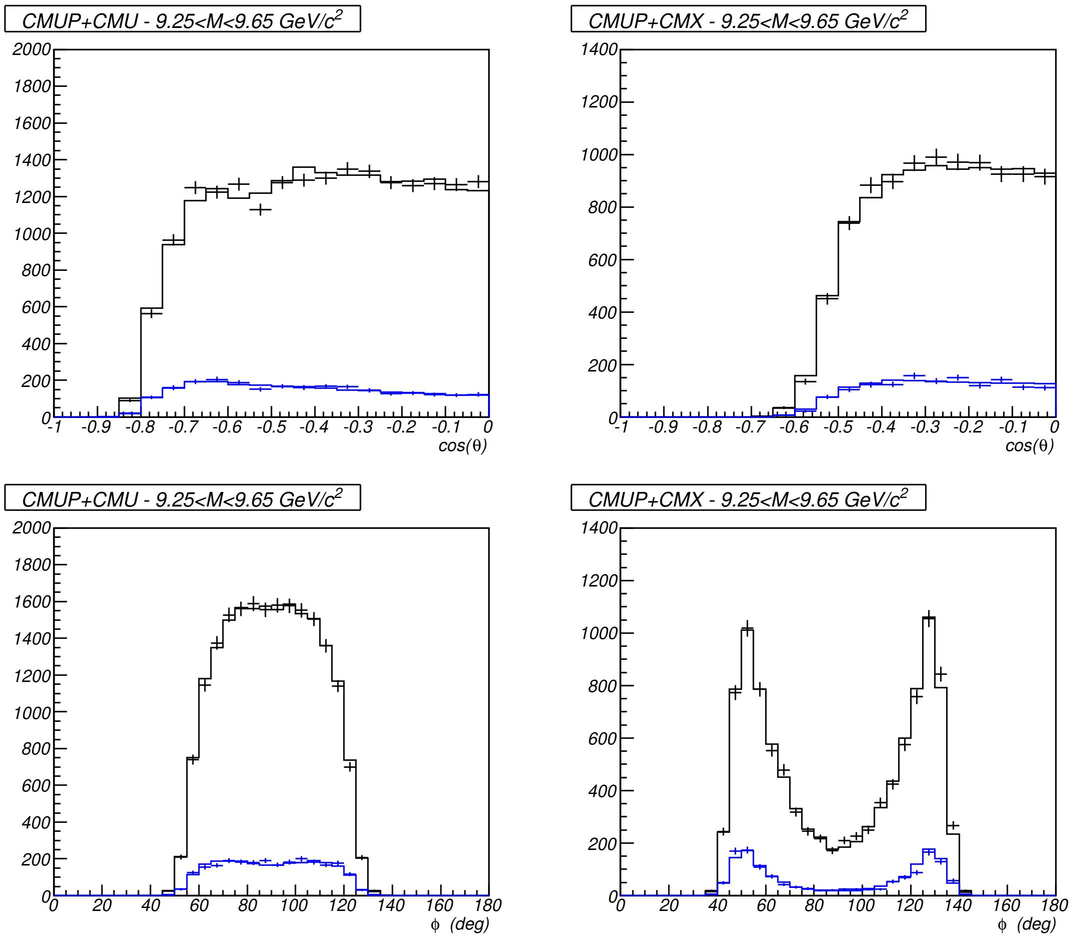

Figure 44: Projections of data (error bars) in the $\Upsilon(1S)$ signal mass range onto the $\cos\theta$ and φ axes in the S-channel helicity frame compared with the fit model (histogram) for CMUP+CMU and CMUP+CMX trigger paths. The displaced track sub-sample is shown in blue, while the complementary sample is shown in black.

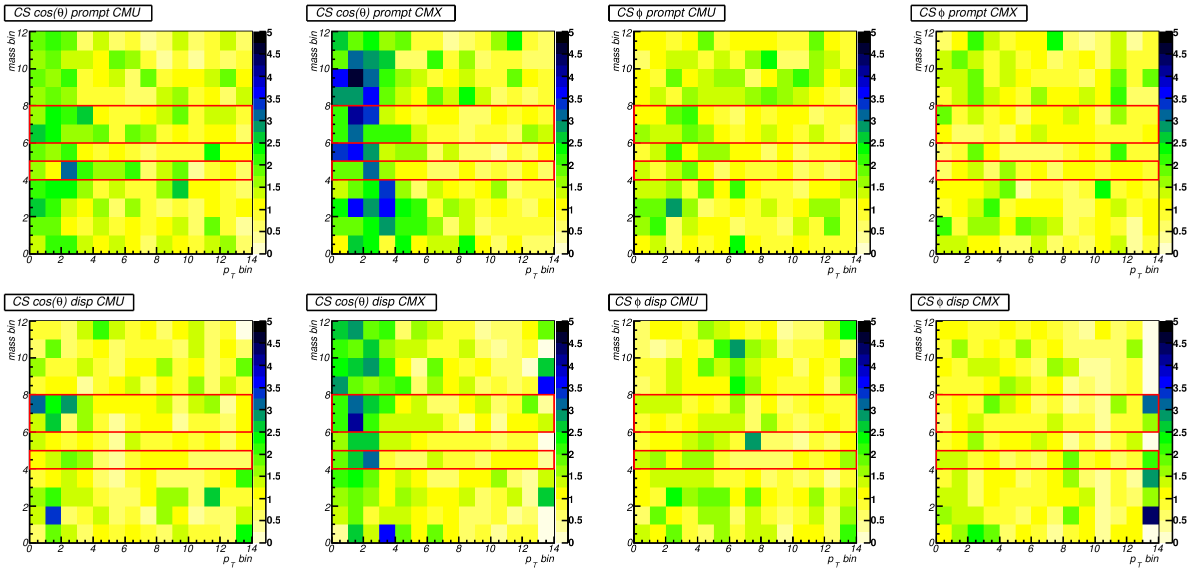

Figure 45: Normalized $\hat{\chi}'^2$ statistic calculated for projections in the Collins-Soper frame.

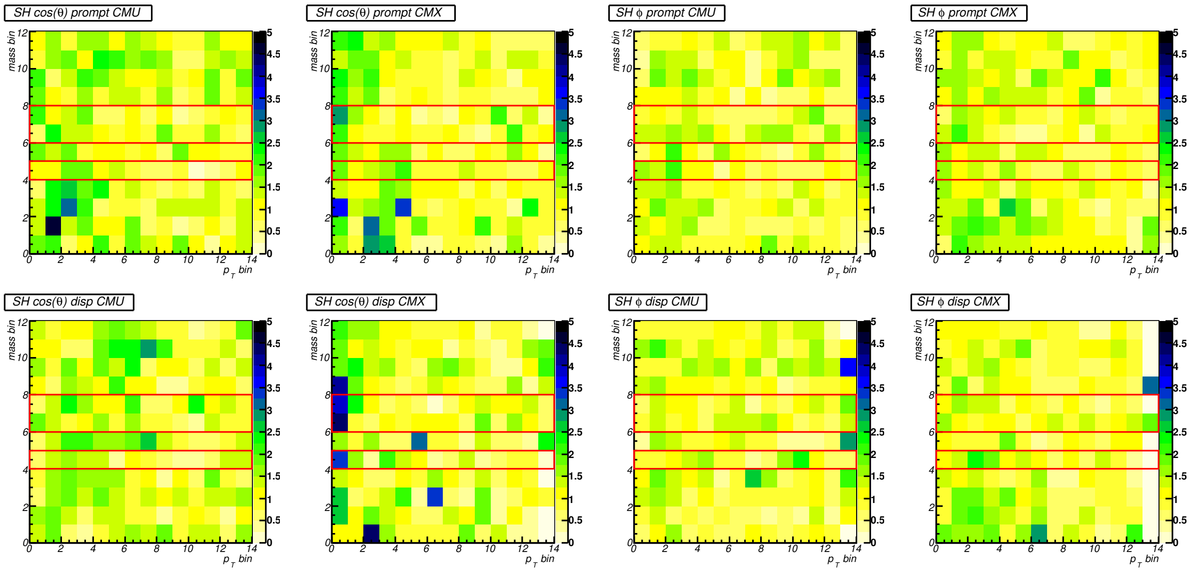

Figure 46: Normalized $\hat{\chi}'^2$ statistic calculated for projections in the S-channel helicity frame.

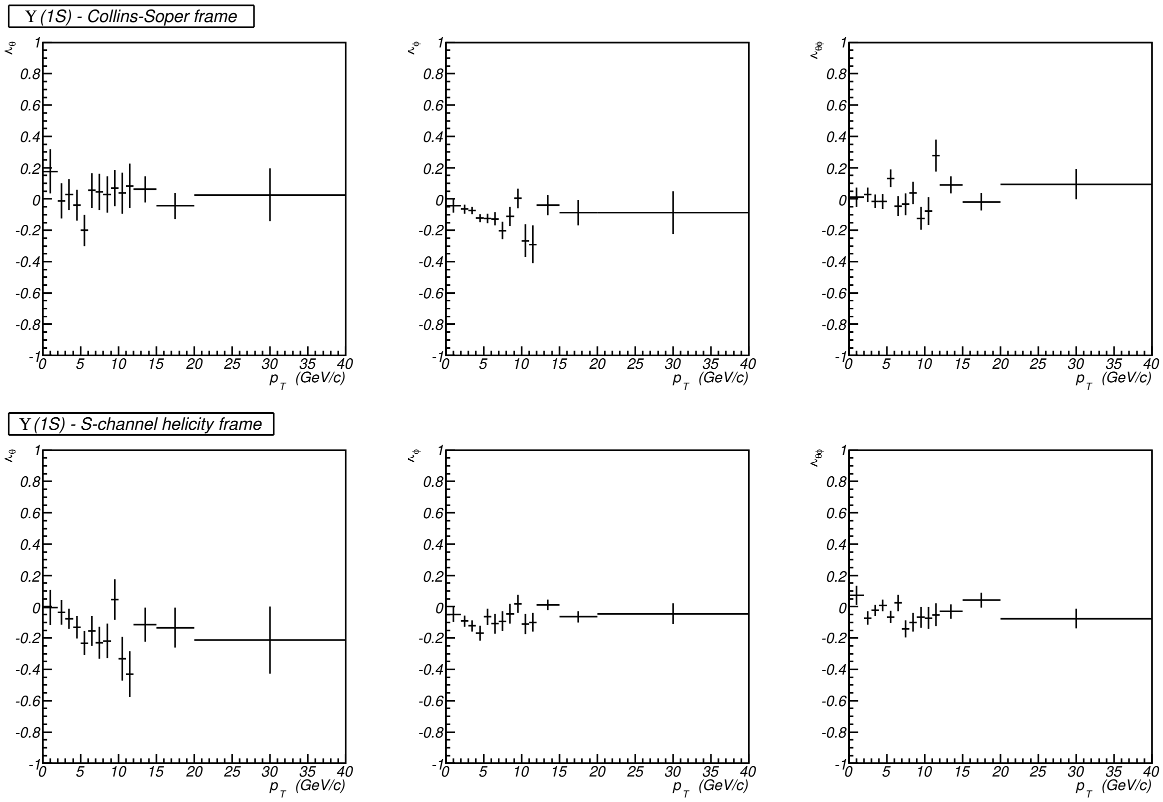

Figure 47: Values of λ_θ, λ_φ and $\lambda_{\theta\varphi}$ obtained from the fit to the $\Upsilon(1S)$ mass range.

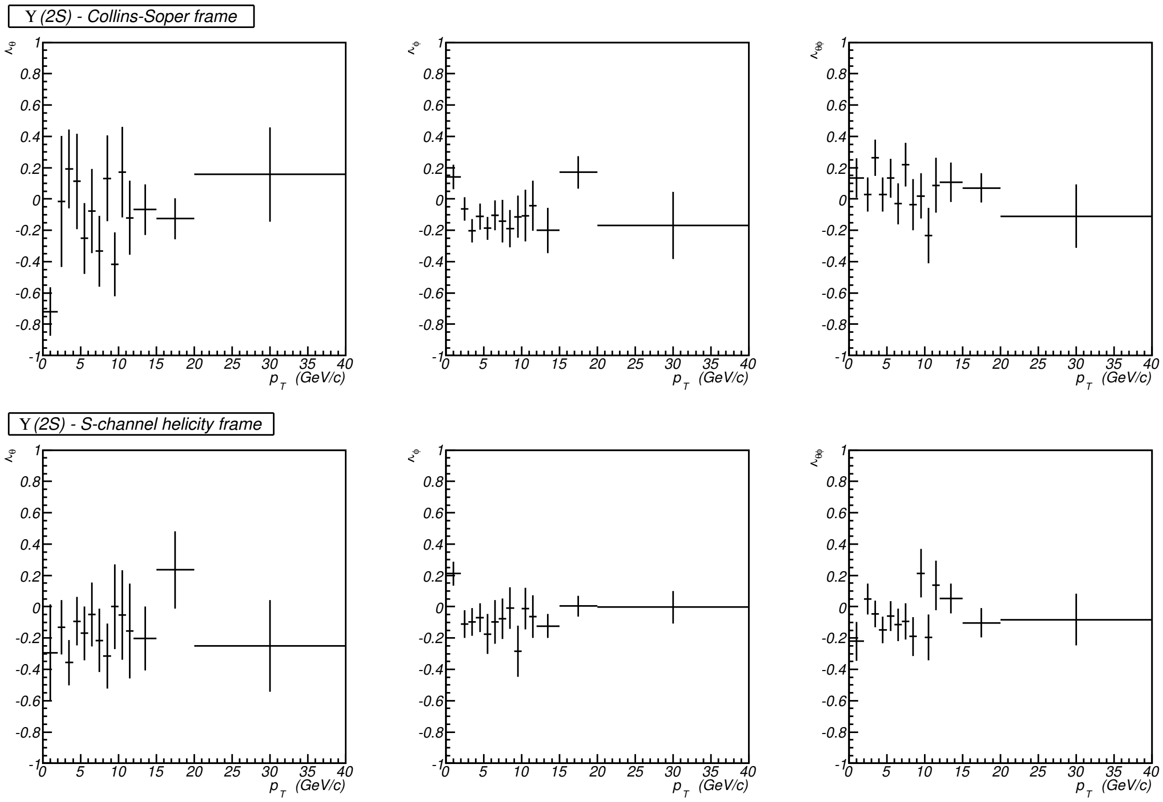

Figure 48: Values of λ_θ, λ_φ and $\lambda_{\theta\varphi}$ obtained from the fit to the $\Upsilon(2S)$ mass range.

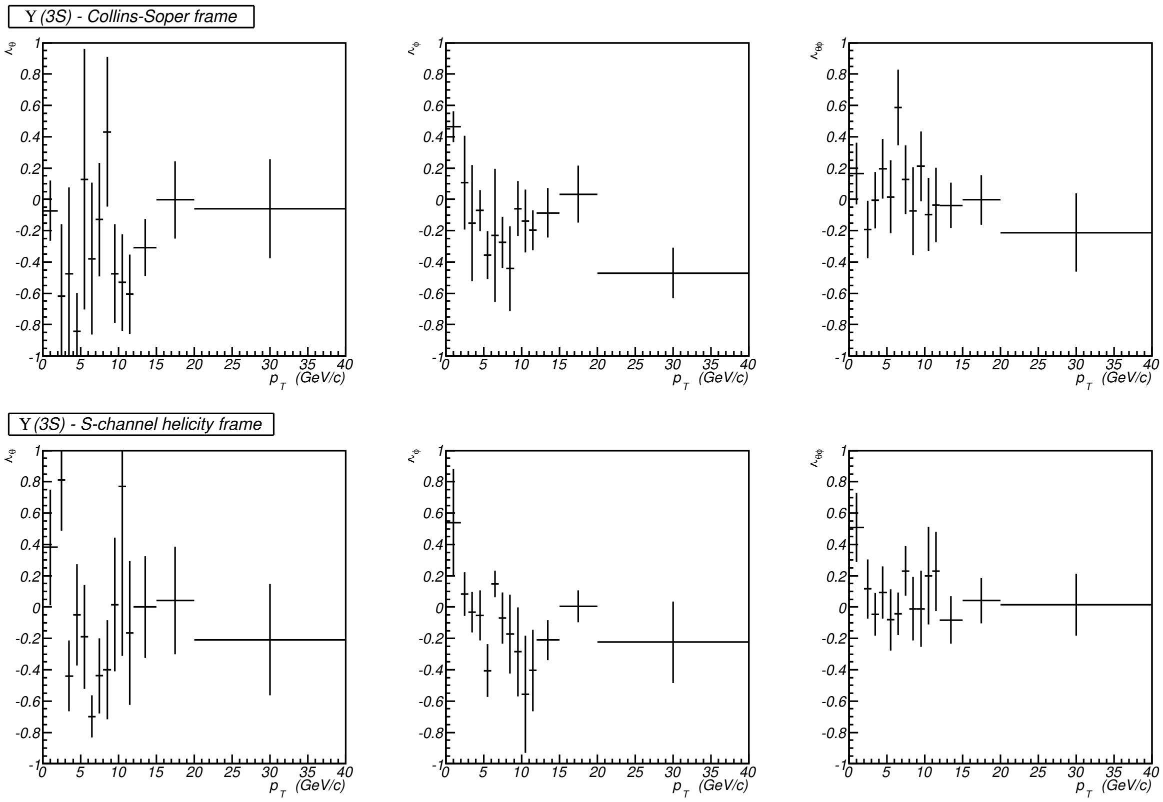

Figure 49: Values of λ_θ, λ_φ and $\lambda_{\theta\varphi}$ obtained from the fit to the $\Upsilon(3S)$ mass range.

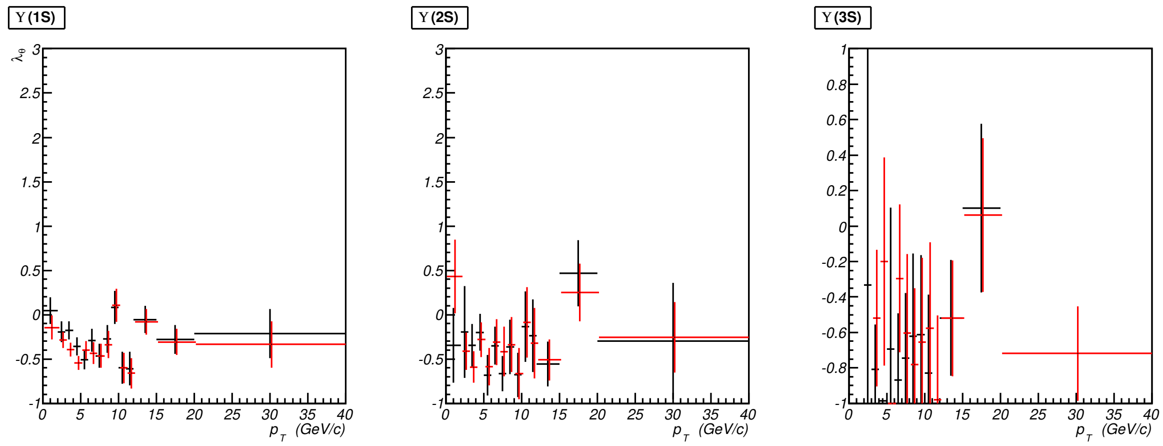

Figure 50: Values of $\tilde{\lambda}$ for the $\Upsilon(1S)$, $\Upsilon(2S)$ and $\Upsilon(3S)$ fits performed in the Collins-Soper frame (black) and the S-channel helicity frame (red). The error bars for the results in the S-channel helicity frame have been offset slightly in p_T for clarity.

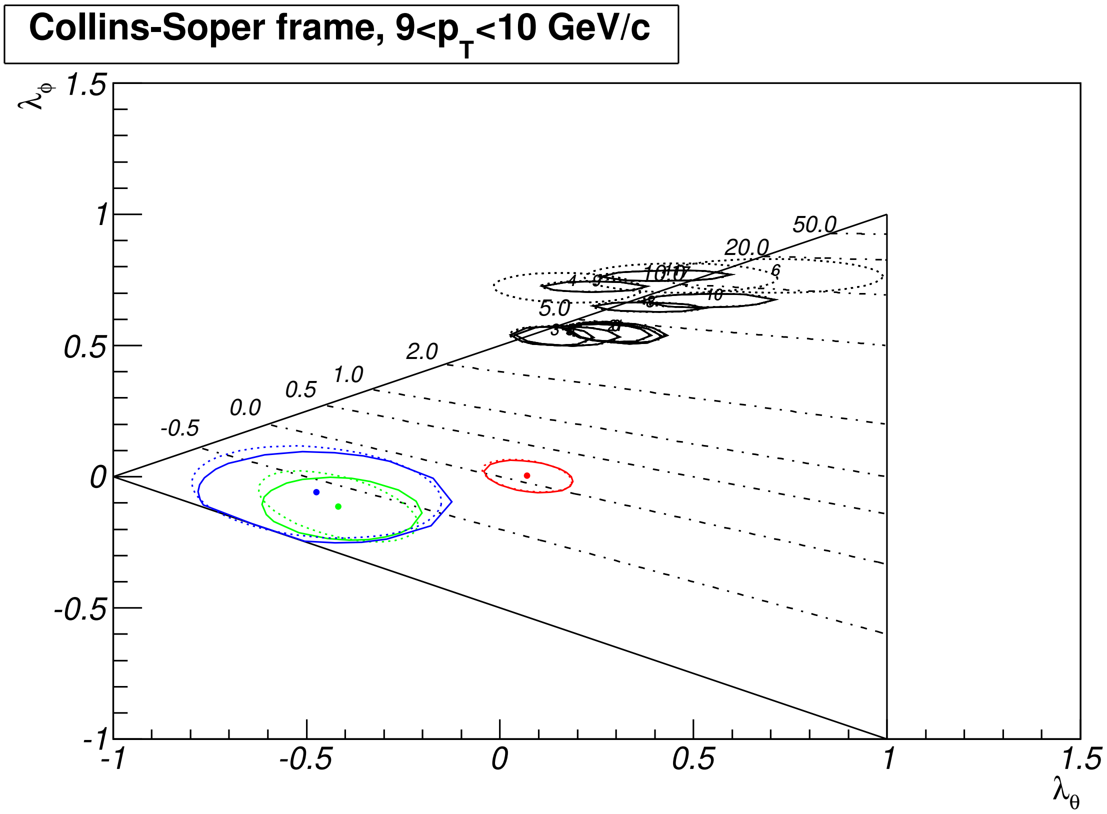

Figure 51: One-sigma confidence intervals for λ_θ and λ_φ in the Collins-Soper frame for the $\Upsilon(1S)$ (red), $\Upsilon(2S)$ (green) and $\Upsilon(3S)$ (blue) states and the background mass ranges (black). Solid contours were calculated using `mncont`, whereas the dotted ellipses are derived from the covariance matrix of the fitted parameters. Contours for background in the signal mass ranges are numbered 4, 6 and 7. The dot-dashed lines show the contours with equal values of the angular invariant quantity, $\tilde{\lambda} = (\lambda_\theta + 3\lambda_\varphi)/(1 - \lambda_\varphi)$.

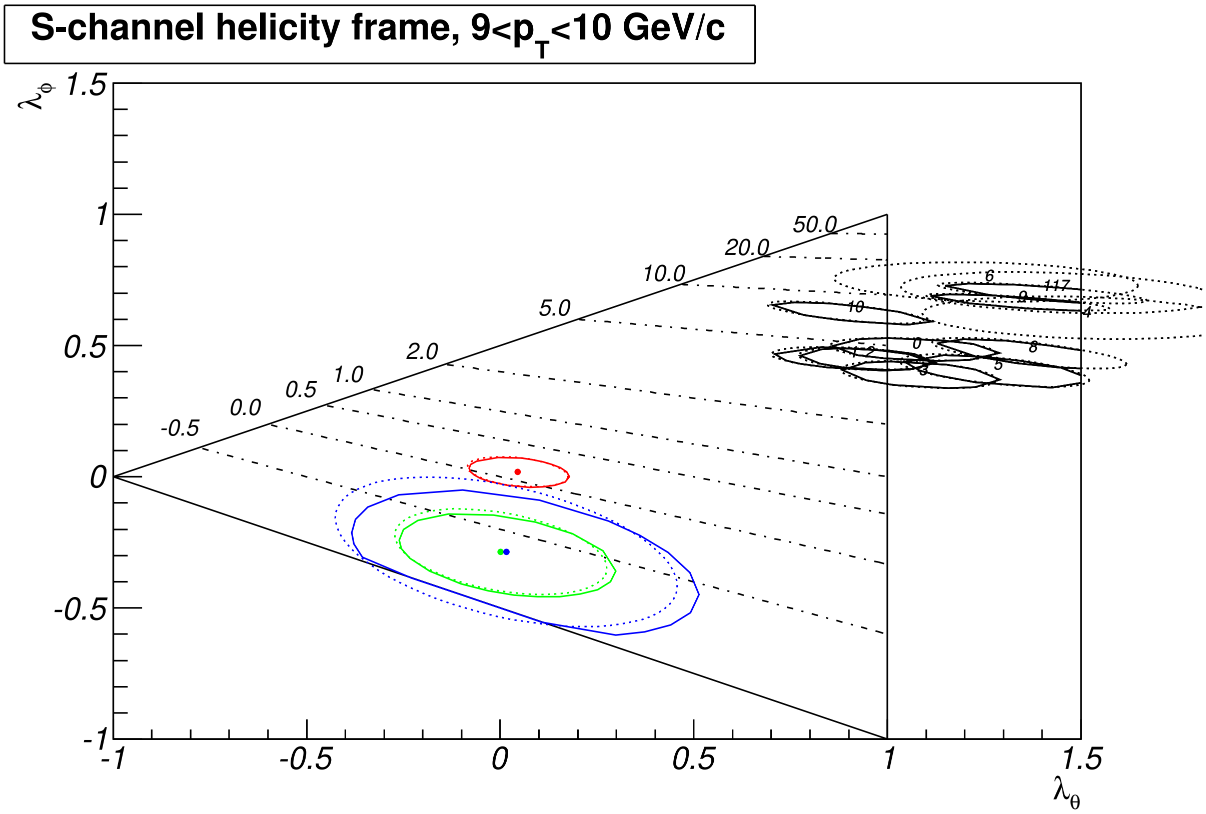

Figure 52: One-sigma confidence intervals for λ_θ and λ_φ in the S-channel helicity frame for the $\Upsilon(1S)$ (red), $\Upsilon(2S)$ (green) and $\Upsilon(3S)$ (blue) states and the background mass ranges (black). Solid contours were calculated using `mncont`, whereas the dotted ellipses are derived from the covariance matrix of the fitted parameters. Contours for background in the signal mass ranges are numbered 4, 6 and 7. The dot-dashed lines show the contours with equal values of the angular invariant quantity, $\tilde{\lambda} = (\lambda_\theta + 3\lambda_\varphi)/(1 - \lambda_\varphi)$.

6.6 Modified background parameterization

Although the angular distribution from Equation 2 is used to describe the background, there is no physical significance attributed to the coefficients. Furthermore, additional terms that improve significantly the quality of the fit to the background angular distribution are justified since there is no reason, *a priori*, to expect that this angular distribution would provide a satisfactory description.

Figure 45 shows that the quality of the fit is poorest at low mass in the $\cos\theta$ projection in the Collins-Soper frame. The quality of the fit was found to improve significantly when an additional term proportional to $\cos^4\theta$ was added to the angular distribution. Figures 53 and 54 show the normalized $\hat{\chi}'^2$ statistic in the Collins-Soper and S-channel helicity frames resulting from this alternate treatment of the background parameterization. Figures 55 and 56 show the changes in λ_θ, λ_φ and $\lambda_{\theta\varphi}$ that result from introducing the modified background parameterization.

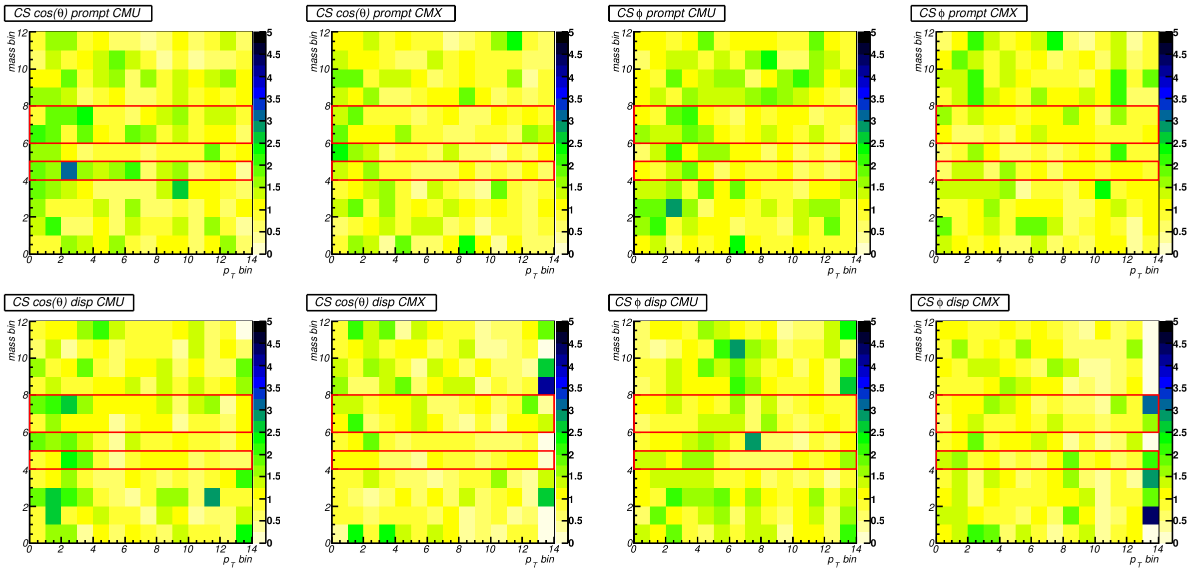

Figure 53: Normalized $\hat{\chi}'^2$ statistic calculated for projections in the Collins-Soper frame with an additional $\cos^4\theta$ term included in the background description.

7 Systematic Uncertainties

The evaluation of systematic uncertainties are divided into three categories. The first category accounts for how the uncertainties in external parameters influences the final results. This includes uncertainties in the Level 1 trigger efficiency parameterization and the uncertainties in the fitted parameters obtained from fits to the J/ψ samples. The second category assesses the uncertainty due to the finite size of the Monte Carlo samples used to calculate the acceptance which is binned in the angular variables $\cos\theta$ and φ. Although the numbers of Monte Carlo signal and background events that were generated are large, they are still finite and it is important to determine the extent to which statistical fluctuations in the acceptance affect the parameters that characterize the angular distribution. The third source of systematic uncertainty is somewhat more nebulous as it attempts to quantify the sizes of any unknown biases that might be present in the analysis. The methods used to assess these uncertainties and their influence on the final estimates of λ_θ, λ_φ and $\lambda_{\theta\varphi}$ are discussed in the following sections.

7.1 Trigger and reconstruction efficiencies

The uncertainties on the Level 1 trigger efficiency are generally very small and are not expected to significantly influence the final results. Likewise, the parameterizations of the CMP trigger efficiency and the $\chi^2 < 9$ stub-track matching cut are measured with high precision. Nevertheless, the systematic uncertainties in λ_θ, λ_φ and $\lambda_{\theta\varphi}$ due to the statistical uncertainties in the efficiency parameterizations are estimated by simultaneously adjusting each efficiency by $\pm 1\sigma$ and repeating the fits to the angular distributions. The systematic uncertainty due to the observed variation is taken as the maximum deviation from the nominal value. This is significantly smaller than the statistical uncertainty in all cases.

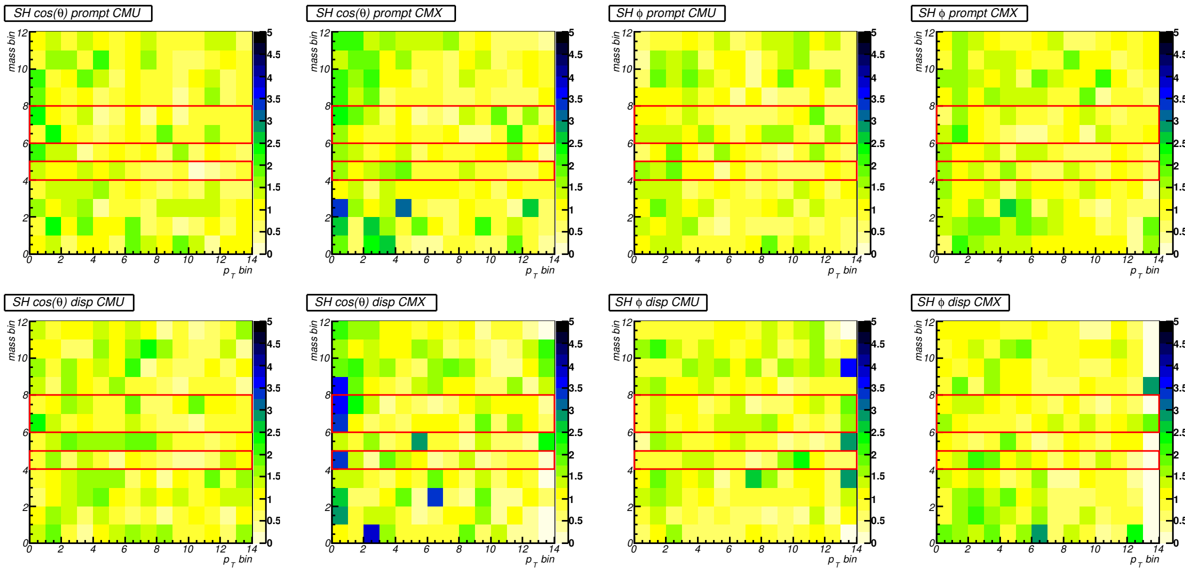

Figure 54: Normalized $\hat{\chi}'^2$ statistic calculated for projections in the S-channel helicity frame with an additinal $\cos^4\theta$ term included in the background description.

7.2 Monte Carlo statistics

Tables 2-4 list the number of events in the $\Upsilon(nS)$ signal mass bins, compared with the number of Monte Carlo events passing the trigger and reconstruction criteria that are used to calculate the acceptance for signal and background. In many cases, the Monte Carlo samples are much larger than the number of events selected in the data, but this is not true in all p_T ranges. Therefore, it is important to quantify the systematic uncertainty in any measurements that is due solely to the finite size of the Monte Carlo samples used in the analysis.

The systematic uncertainty due to the finite size of Monte Carlo samples is calculated using a toy Monte Carlo. Events in a given p_T range are randomly generated with $\cos\theta$ and φ in the S-channel helicity frame distributed according to the measured angular distribution. The acceptance in the S-channel helicity frame, calculated from the Monte Carlo samples, is sampled to simulate the effects of geometric acceptance, trigger and reconstruction criteria. The selected angular distribution is recorded for both the generated angles in the S-channel helicity frame and the angles in the corresponding Collins-Soper frame. These are then fit using the same acceptance distributions as unpolarized templates. In this way, the uncertainty in the measured angular distribution parameters, $(\delta\hat{\lambda})$ has no contribution from Monte Carlo statistics, since the same acceptance used in the generation is used in the fit. The effect of finite Monte Carlo statistics is then included by randomizing the contents in each bin of the acceptance distributions according to their binomial probability density. The resulting uncertainty in the measured angular distribution parameters $(\delta\lambda)$ now includes both statistical uncertainties from the size of the simulated data and from the acceptance. The uncertainty due to finite Monte Carlo statistics is then calculated using $\delta\lambda^2_{MC} = \delta\lambda^2 - \delta\hat{\lambda}^2$.

Figure 57 shows an example of the distributions of differences between generated and fitted parameters from the toy Monte Carlo with and without randomization of the acceptances with binomial statistics. The systematic uncertainty due to finite Monte Carlo statistics are found to be much smaller than the statistical uncertainty of the fitted parameters.

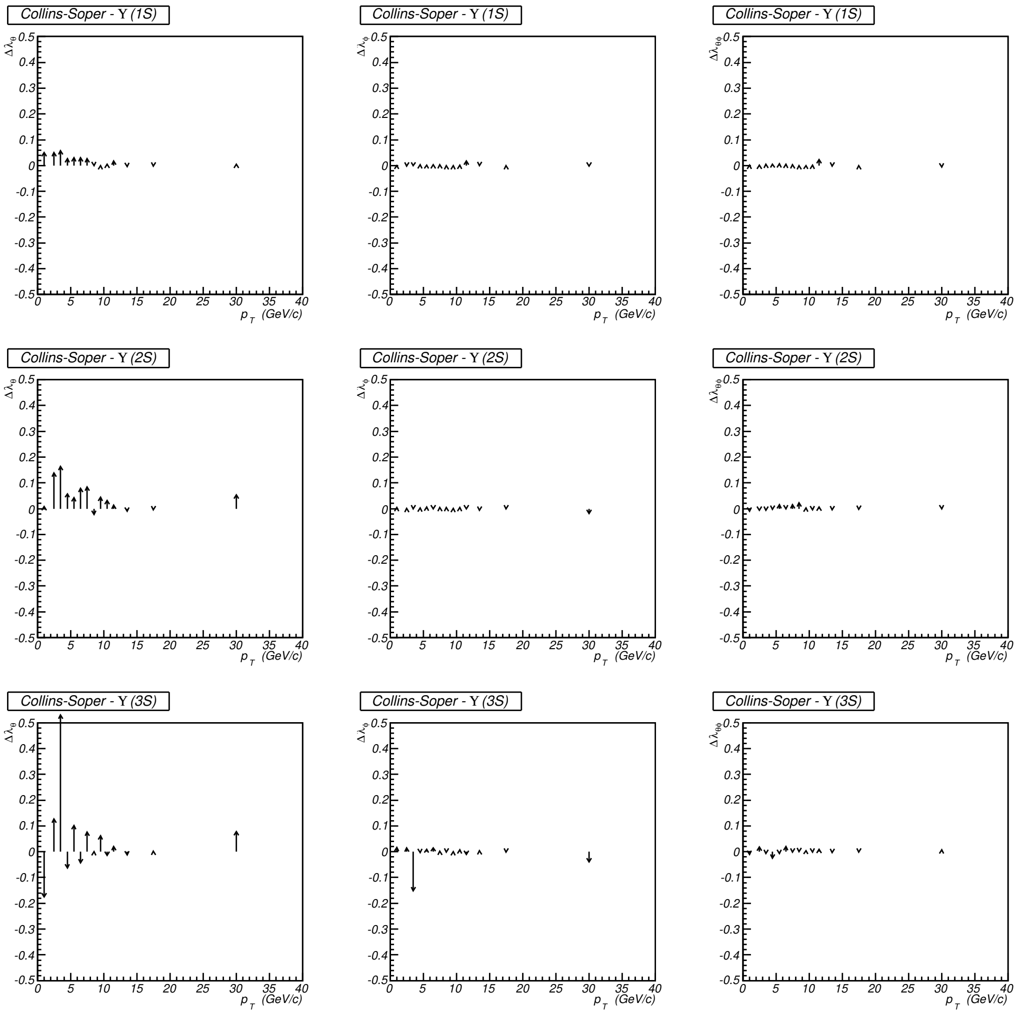

Figure 55: Changes in the parameters λ_θ, λ_φ and $\lambda_{\theta\varphi}$ resulting from the modified background parameterization in the Collins-Soper frame.

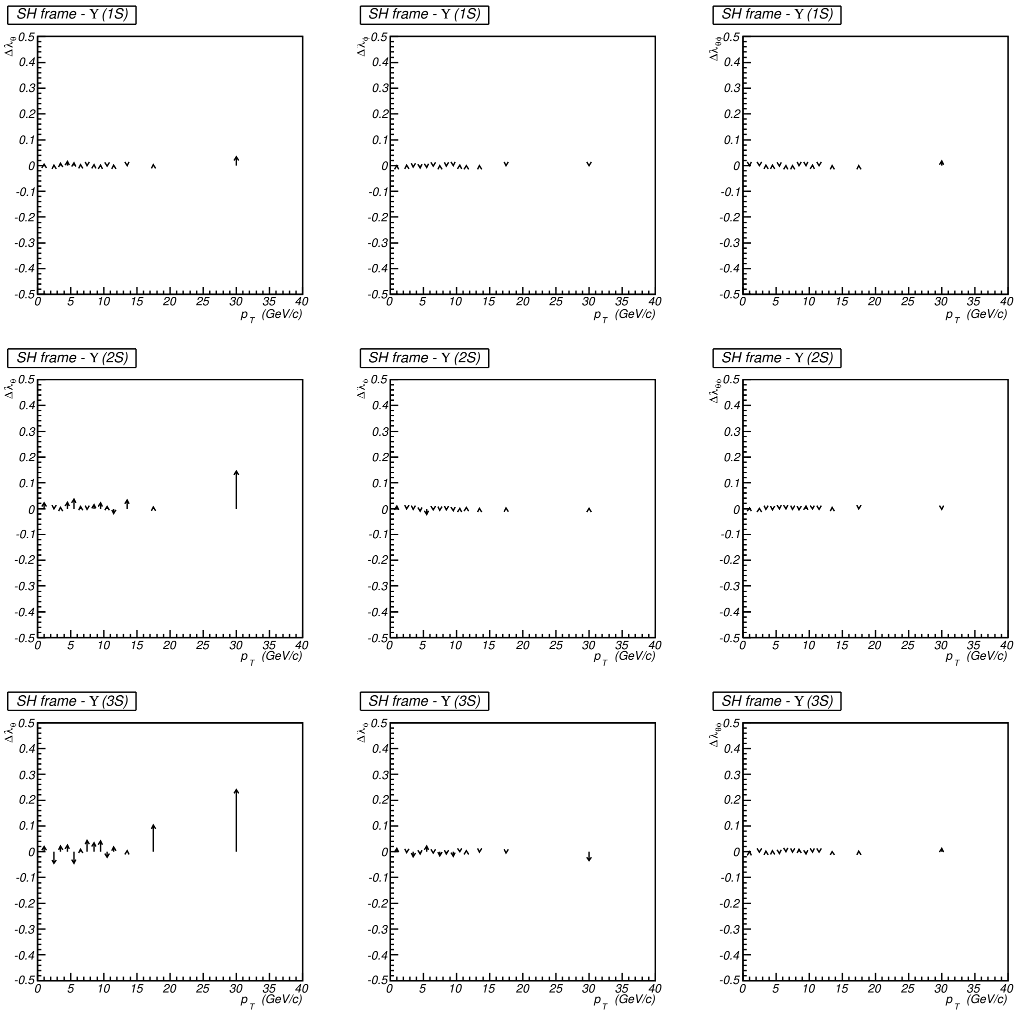

Figure 56: Changes in the parameters λ_θ, λ_φ and $\lambda_{\theta\varphi}$ resulting from the modified background parameterization in the S-channel helicity frame.

p_T [GeV/c]	CMU data/MC/bkg	CMX data/MC/bkg
$0-2$	36758/52373/34708	18898/25745/14191
$2-3$	46077/55972/37060	23365/26970/15270
$3-4$	46145/61479/38699	22377/28598/15534
$4-5$	38755/60559/41163	17728/27480/16407
$5-6$	28190/57935/40446	13149/27078/15987
$6-7$	19380/56715/38850	9804/28129/16477
$7-8$	13527/55189/37033	7210/29307/17115
$8-9$	9819/57921/38229	5441/31641/18262
$9-10$	7228/77326/51696	4253/43409/25439
$10-11$	5282/61953/39537	3219/37651/21564
$11-12$	4047/64572/41256	2547/41807/24394
$12-15$	7023/105434/64865	5071/75572/43176
$15-20$	4437/143031/73973	2872/94885/49125
$20-40$	2130/210922/120601	866/92033/47516
$2-4$	92215/102149/67977	45741/47224/27040
$4-6$	66942/100900/71644	30875/45494/27222
$6-12$	59270/140751/94849	32472/73235/41431
$12-40$	13589/233803/153868	8809/146693/85535
$6-8$	32903/76849/58817	17014/37482/24328
$8-12$	26374/63902/36032	15459/35753/17103
$12-17$	9457/159507/105200	6789/109473/64731
$17-23$	2975/57975/38019	1640/30961/17437
$23-40$	1157/16289/10692	381/6211/3319

Table 2: Statistics in the $\Upsilon(1S)$ signal mass range. The three numbers $x/y/z$ represent the number of events selected in the prompt sample in data (x), the number of selected Monte Carlo $\Upsilon(1S)$ signal events (y) and the number of Monte Carlo background events (z) for the CMUP+CMU and CMUP+CMX trigger paths.

p_T [GeV/c]	CMU data/MC/bkg	CMX data/MC/bkg
$0-2$	12573/34731/18873	7690/20164/9270
$2-3$	16265/37497/20235	9443/20101/9627
$3-4$	15838/42741/21836	8862/21941/9690
$4-5$	13844/43427/24383	7055/22048/10809
$5-6$	10765/41599/26049	5160/20500/11125
$6-7$	7666/41894/25989	3777/20911/11137
$7-8$	5142/39893/24778	2809/21126/11373
$8-9$	3800/40307/24839	2020/22334/11942
$9-10$	2670/53172/33912	1632/30137/16100
$10-11$	2017/41818/24783	1260/25476/13452
$11-12$	1547/43974/26302	983/27565/14827
$12-15$	2806/68363/41402	1983/49046/26613
$15-20$	1894/92500/48151	1265/64558/34350
$20-40$	956/131921/80647	448/62173/34157
$2-4$	32098/69400/38686	18305/35368/17068
$4-6$	24608/74645/44486	12215/36345/18765
$6-12$	22841/100798/64960	12480/52952/28646
$12-40$	5656/154614/98481	3696/97162/56005
$6-8$	12808/52875/41314	6586/26109/17386
$8-12$	10034/47923/23646	5895/26843/11260
$12-17$	3844/100676/67787	2687/68585/41364
$17-23$	1327/40238/23914	778/23023/12384
$23-40$	485/13673/6732	231/5545/2232

Table 3: Statistics in the $\Upsilon(2S)$ signal mass range. The three numbers $x/y/z$ represent the number of events selected in the prompt sample in data (x), the number of selected Monte Carlo $\Upsilon(2S)$ signal events (y) and the number of Monte Carlo background events (z) for the CMUP+CMU and CMUP+CMX trigger paths.

p_T [GeV/c]	CMU data/MC/bkg	CMX data/MC/bkg
$0-2$	9057/32866/17888	6142/20312/9108
$2-3$	11928/37412/19582	7390/21359/9537
$3-4$	11907/40872/21431	6831/22114/9986
$4-5$	10156/43297/24767	5321/22682/11450
$5-6$	8029/43938/27318	3952/22261/12065
$6-7$	5828/40514/28173	2875/20600/12631
$7-8$	3974/40940/27352	2079/21785/12712
$8-9$	2796/40421/26441	1538/22438/12771
$9-10$	1981/53478/36125	1213/29672/17285
$10-11$	1585/41437/26387	879/25172/14441
$11-12$	1242/43160/27922	676/26892/15489
$12-15$	2162/67528/43751	1450/47398/27645
$15-20$	1459/88809/52319	1003/64024/37350
$20-40$	859/133968/87636	397/64658/38837
$2-4$	23834/67037/38010	14221/35901/17391
$4-6$	18183/76300/45846	9273/38841/19920
$6-12$	17398/102229/72201	9258/53852/31814
$12-40$	4478/153520/104191	2850/97127/59743
$6-8$	9800/51441/46439	4954/25654/19493
$8-12$	7602/50788/25762	4304/28198/12321
$12-17$	2986/95904/71795	2020/65149/43867
$17-23$	1017/41412/25064	636/25291/13314
$23-40$	477/16174/7321	194/6634/2549

Table 4: Statistics in the $\Upsilon(3S)$ signal mass range. The three numbers $x/y/z$ represent the number of events selected in the prompt sample in data (x), the number of selected Monte Carlo $\Upsilon(3S)$ signal events (y) and the number of Monte Carlo background events (z) for the CMUP+CMU and CMUP+CMX trigger paths.

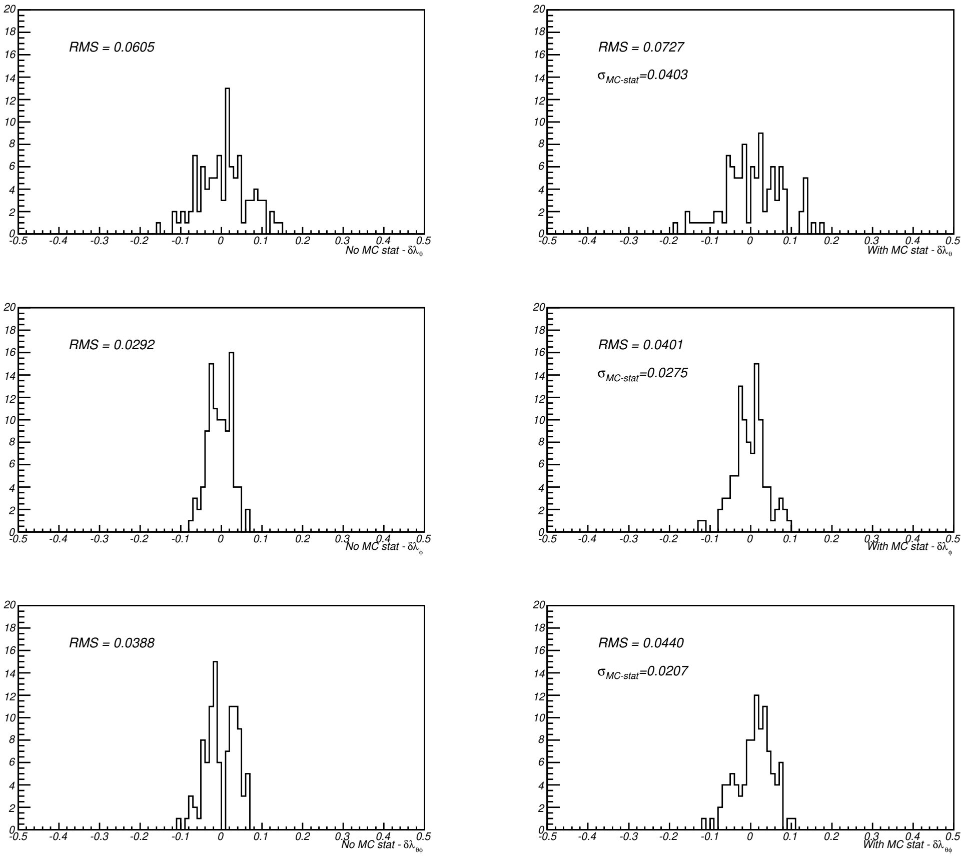

Figure 57: Distributions of the difference between fitted and generated parameters for toy $\Upsilon(1S)$ decays with $p_T = 7.5$ GeV/c. The left plots do not include statistical fluctuations in the Monte Carlo acceptance, while the right plots include fluctuations corresponding to the size of the Monte Carlo samples used in the analysis.

7.2.1 Background constrained by sidebands

The analysis as described up to this point uses the displaced track sample to constrain the shape of the background under the $\Upsilon(nS)$ signals in the prompt component of the data. An alternate approach would be to constrain the properties of the background under the signal peaks by the observed angular distribution of the sidebands. Figures 51 and 52 show examples of the fitted signal and background parameters and one could, in principle, fix the parameters that describe the angular distribution of the background to those measured in one or several background mass bins.

Unfortunately, it is clear that the angular distribution in the background can vary significantly over the range $8.3 < m(\mu^+\mu^-) < 11.7$ GeV/c^2 there is not obvious choice that might be expected to approximate the properties of the background under the signal. In particular, the sidebands below the $\Upsilon(1S)$ and between the $\Upsilon(1S)$ and $\Upsilon(2S)$ states are seen to be generally more "longitudinal" than the higher mass bins which could be a consequence of event migration due to final state radiation.

Furthermore, although the higher mass bins may be clustered together, their scatter includes a component that is quantified by the measured uncertainties on their angular distribution parameters. The fact that the fitted background parameters using the displaced track sample are in general agreement with those in the high-mass sidebands suggests that their mutual constraint might be reasonable. However, the difference in the measured angular distribution parameters obtained using the displaced track sample constraint and the high-mass sideband constraint would include a significant statistical component due to the different events used in each fit. Given the assumptions that enter into this possible cross-check and the difficulty associated with disentangling the statistical and hypothesized systematic components, we do not want to use this technique to quantify systematic uncertaineis on the $\Upsilon(nS)$ angular distribution.

7.2.2 Choice of reference frame

Unlike the previous case, imeasurements of the angular distributions in the Collins-Soper frame and the S-channel helicity frame make use of exactly the same events, both in $p\overline{p}$ collision data and in the Monte Carlo samples. Although the parameters that characterize the angular distribution are in general expected to differ, combinations of these parameters such as $\tilde{\lambda}$ are should be invariant. Therefore, the extent to which $\tilde{\lambda}$ is not invariant may be used to quantify the uncertainty on the parameters obtained from fits in either reference frame. We propose the following method to assign systematic uncertainties on λ_θ and λ_φ due to an observed variation in $\delta\tilde{\lambda} = \tilde{\lambda}_{CS} - \tilde{\lambda}_{SH}$.

In general, let $u = f(x, y)$ be a function of two variables and define the matrix

$$V = \begin{pmatrix} \partial u/\partial x & \partial u/\partial y \\ \partial u/\partial y & -\partial u/\partial x \end{pmatrix} \tag{40}$$

in which the first and second columns are orthogonal to and parallel to contours of equal values of u. A variation δu along a line perpendicular to the contours of equal u changes x and y by an amount that is characterized by the covariance matrix

$$W = V^{-1} \begin{pmatrix} \delta u^2 & 0 \\ 0 & 0 \end{pmatrix} V^{-1} \tag{41}$$

which is singular but can be added to the covariance matrix from the fit.

Applying this general case to the function $\tilde{\lambda}(\lambda_\theta, \lambda_\varphi) = (\lambda_\theta + 3\lambda_\varphi)/(1 - \lambda_\varphi)$ requires evaluating the derivatives

$$\frac{\partial\tilde{\lambda}}{\lambda_\theta} = \frac{1}{1 - \lambda_\varphi} \tag{42}$$

$$\frac{\partial\tilde{\lambda}}{\lambda_\phi} = \frac{3 + \lambda_\theta}{(1 - \lambda_\varphi)^2} \tag{43}$$

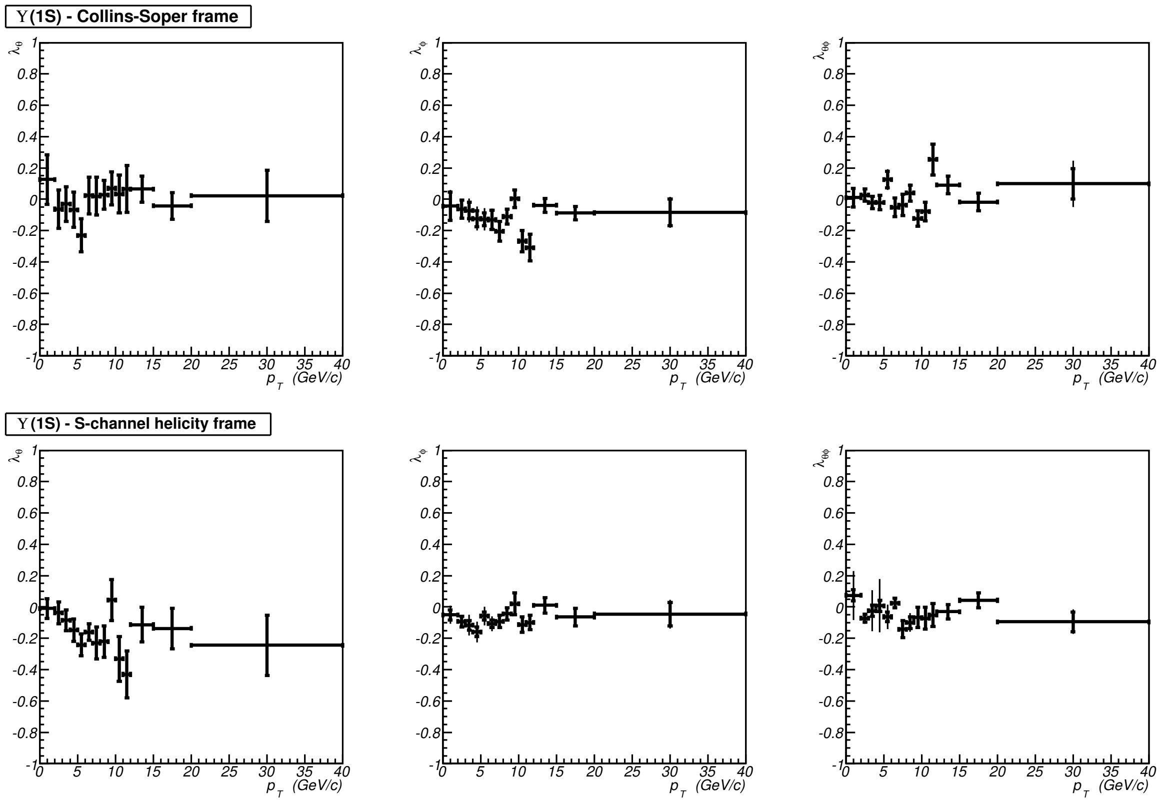

Figure 58: Values of λ_θ, λ_φ and $\lambda_{\theta\varphi}$ obtained from the fit to the $\Upsilon(1S)$ mass range. Inner error bars are statistical only, while the outer error bars include the systematic uncertainty associated with the choice of reference frame added in quadrature.

from which the matrix V is constructed and then inverted. We propose to use the difference $\delta\tilde{\lambda}$ to represent a one-sigma uncertainty associated with the choice of reference frame to obtain the resulting systematic uncertainty in λ_θ and λ_φ.

The influence on $\lambda_{\theta\varphi}$ is calculated using the correlation matrix from the fit. For simplicity, we denote λ_θ, λ_φ and $\lambda_{\theta\varphi}$ as λ_i and the elements of their covariance matrix as σ_{ij}. Then,

$$\frac{\delta\lambda_3}{\sqrt{\sigma_{33}}} = \rho_{13}\frac{\delta\lambda_1}{\sqrt{\sigma_{11}}} + \rho_{23}\frac{\delta\lambda_2}{\sqrt{\sigma_{22}}} \tag{44}$$

$$\delta\lambda_3 = \frac{\sigma_{13}}{\sigma_{11}}\delta\lambda_1 + \frac{\sigma_{23}}{\sigma_{22}}\delta\lambda_2 \tag{45}$$

where

$$\delta\lambda_i = \left(\frac{\partial\tilde{\lambda}}{\partial\lambda_i}\right)^{-1}\delta\tilde{\lambda} \tag{46}$$

The systematic uncertainty in $\lambda_{\theta\varphi}$ associated with non-zero $\delta\tilde{\lambda}$ is assigned the value of $|\delta_3|$.

Figures 58–60 show the fitted parameters with these systematic uncertainties added in quadrature to the statistical uncertainties and where the background includes a $\cos^4\theta$ term. These figures correspond to the tables listed in Appendix A.

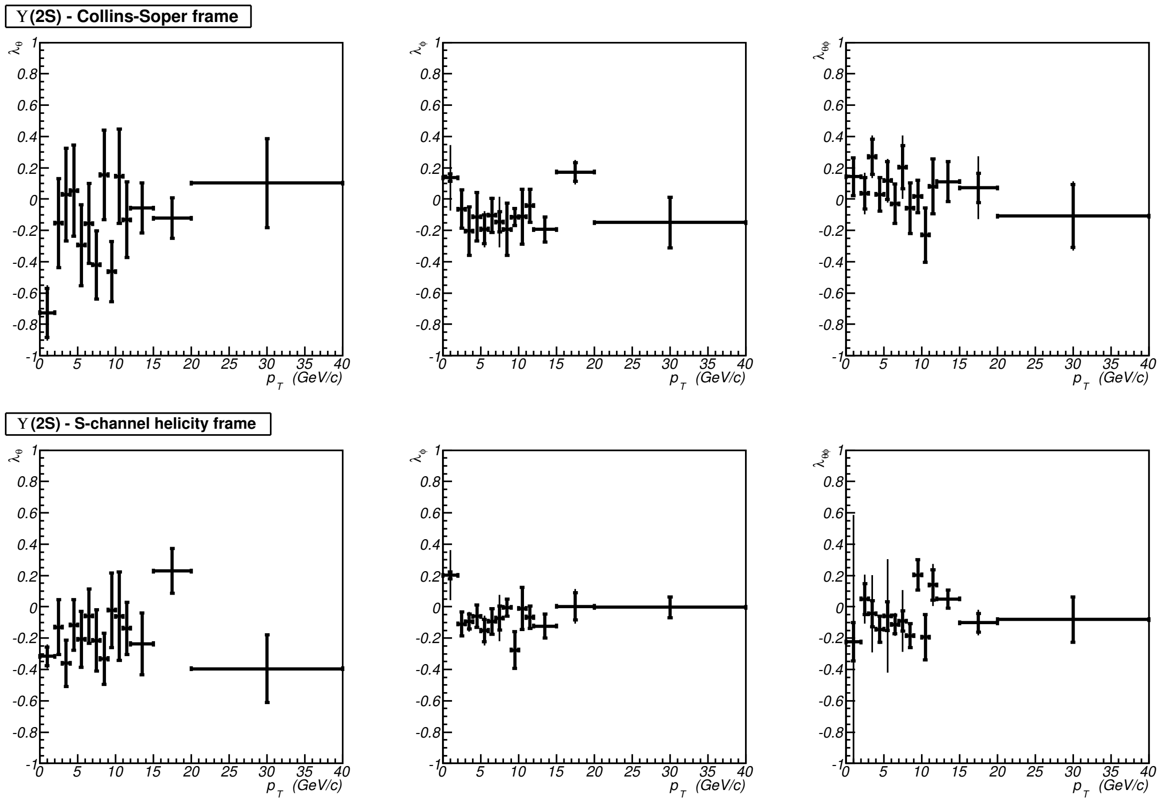

Figure 59: Values of λ_θ, λ_φ and $\lambda_{\theta\varphi}$ obtained from the fit to the $\Upsilon(2S)$ mass range. Inner error bars are statistical only, while the outer error bars include the systematic uncertainty associated with the choice of reference frame added in quadrature.

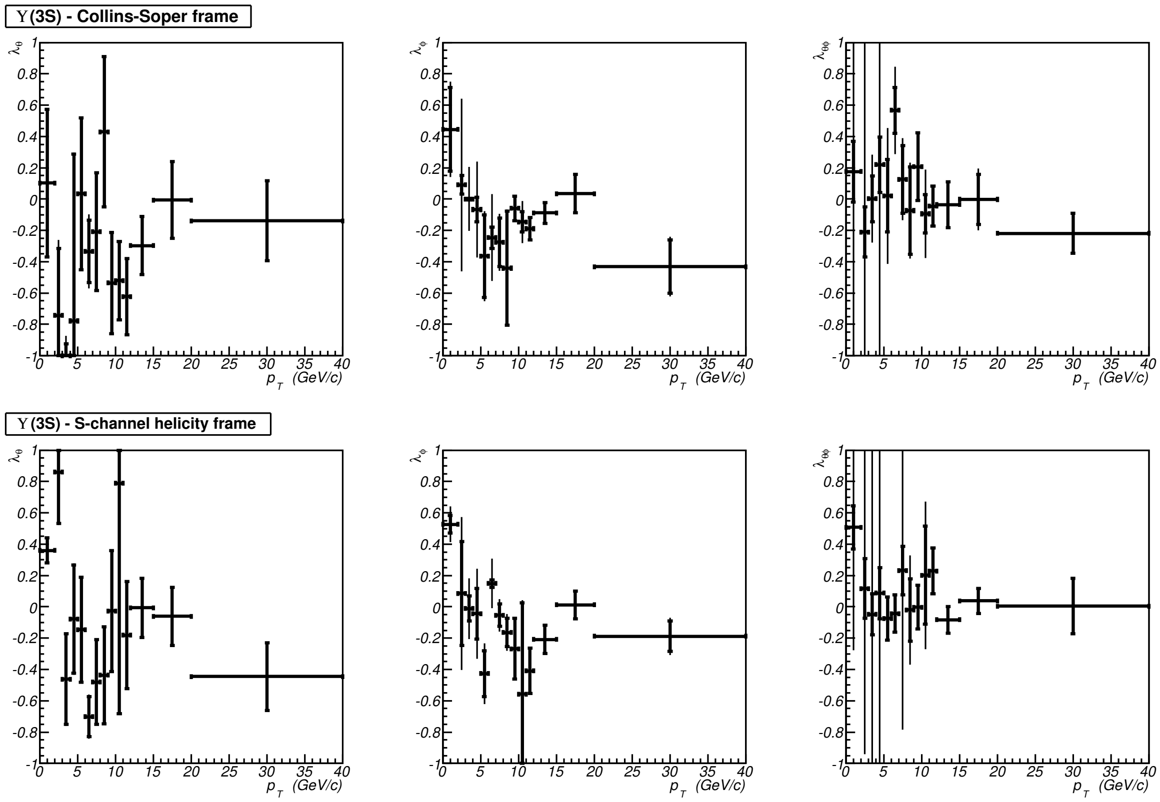

Figure 60: Values of λ_θ, λ_φ and $\lambda_{\theta\varphi}$ obtained from the fit to the $\Upsilon(3S)$ mass range. Inner error bars are statistical only, while the outer error bars include the systematic uncertainty associated with the choice of reference frame added in quadrature.

The toy Monte Carlo described in Section 7.2 was used to determine the size of statistical fluctuations in $\Delta\tilde{\lambda}$. Some of the difference between values of $\tilde{\lambda}$ measured in different reference frames is expected to be purely statistical, but in other cases the difference is too large to be explained by statistical fluctuations. Therefore, it is included as a systematic uncertainty in all p_T bins since the sizes of statistical fluctuations are generally small and do not significantly change the interpretation of the results. Larger deviations require greater care, and the systematic uncertainty quantified in this way takes this level of suspicion into account.

7.3 Alternate p_T binning

The statistical precision of measurements in individual p_T bins can be improved by using wider ranges of p_T than the ones described previously. In this case we perform the analysis in bins chosen to match those used previously[9]. The results obtained using 8 bins from $0 - 40$ GeV/c are shown in Figure 61 and the results using only 5 bins are shown in Figure 62.

7.4 Comparison with other results

Previously published results have only measured λ_θ in the S-channel helicity frame for the $\Upsilon(1S)$ and $\Upsilon(2S)$ states. Figures 63 and 64 show the comparison with the Run I CDF result and the Run II DØresults. The current result is clearly in disagreement with the DØ$\Upsilon(1S)$ result and the uncertainties on the Run I CDF result are sufficiently large that the results are not in obvious disagreement. Nevertheless, because of the different rapidity coverage used in each analysis, it may be possible that there is significant longitudinal polarization that evolves rapidly with $y(\Upsilon)$.

The measurement of λ_θ in the S-channel helicity frame is also not in good agreement with the previously blessed CDF result[9], as seen in Figure 65. However, as seen in Figure 66, it is in reasonable agreement with a newer result[10] (currently unblessed) that is intended to supercede the previously blessed result.

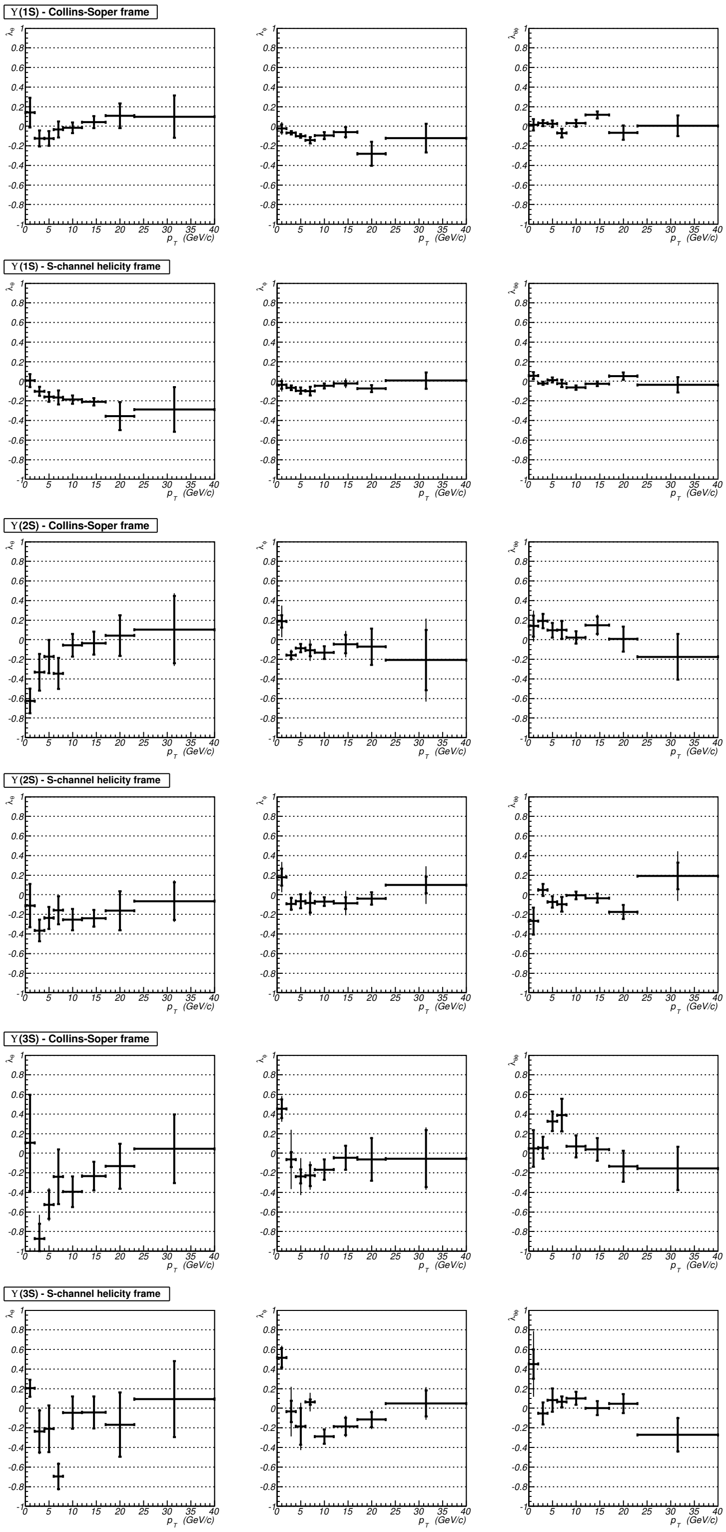

Figure 61: Fitted parameters using 8 p_T bins.

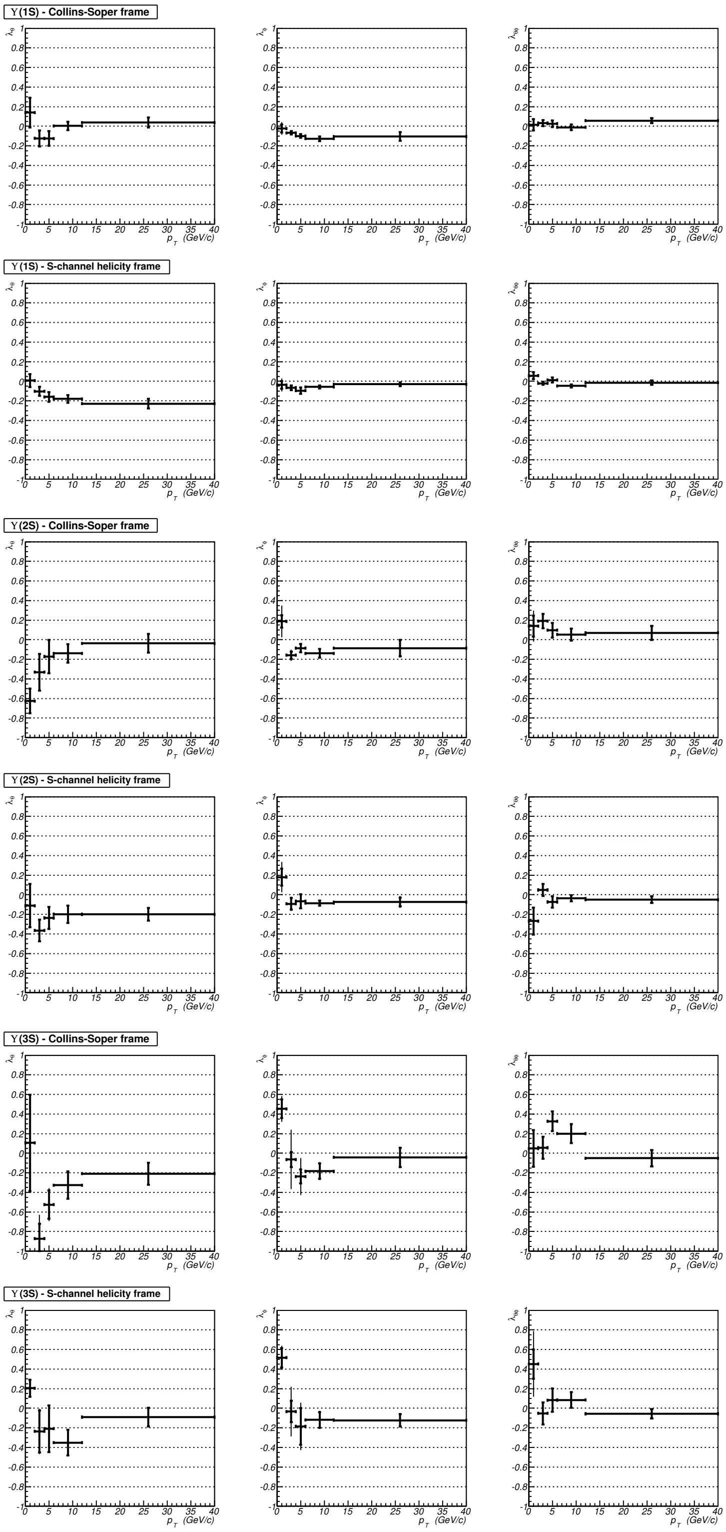

Figure 62: Fitted parameters using 5 p_T bins.

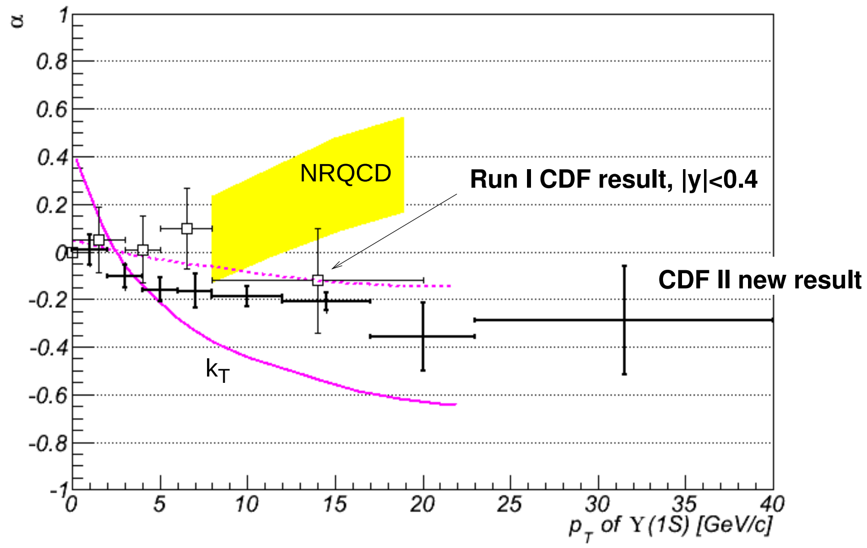

Figure 63: Comparison of current analysis with previously published CDF result from Run I. The results of this analysis are shown with thick error bars.

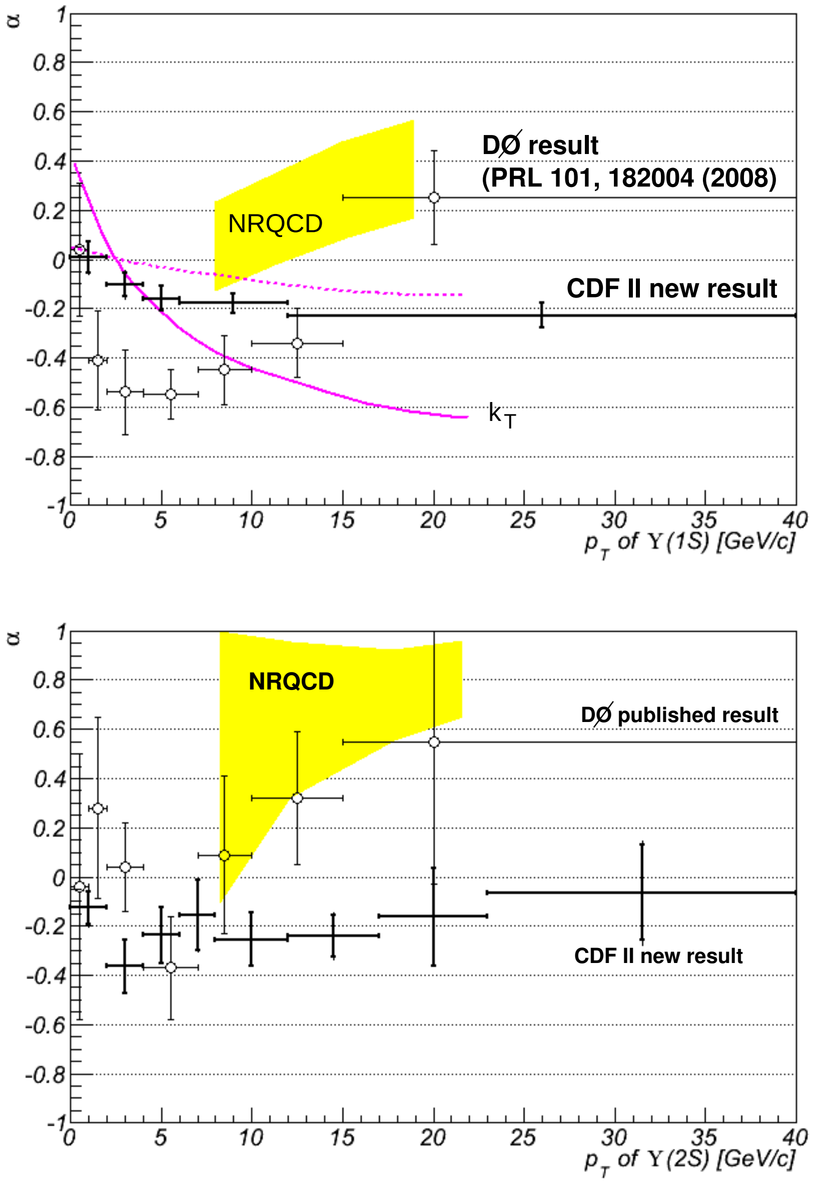

Figure 64: Comparison of current analysis with published DØresults from Run II. The results of this analysis are shown with thick error bars.

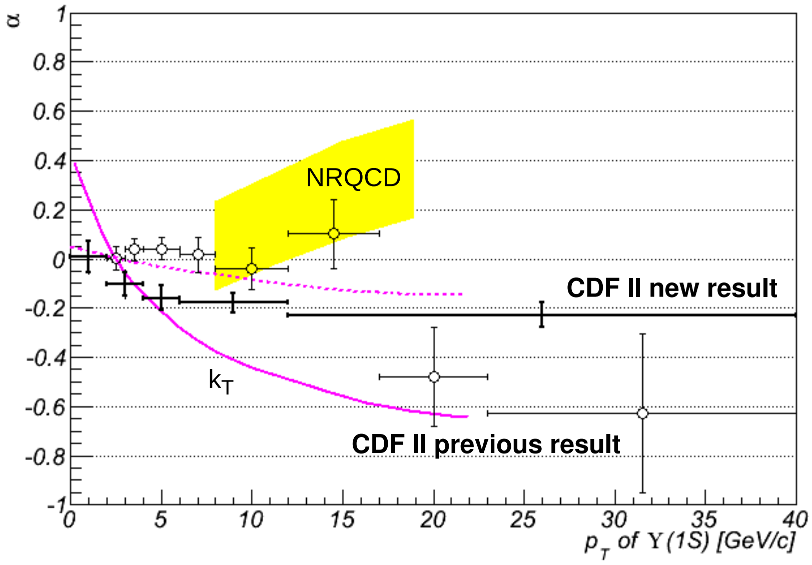

Figure 65: Comparison of current analysis with most recently blessed CDF result from Run II. The results of this analysis are shown with thick error bars.

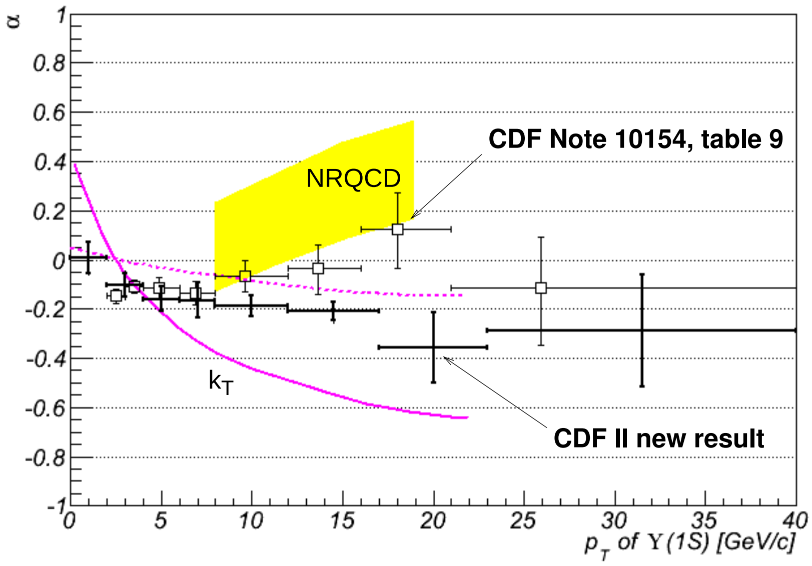

Figure 66: Comparison of current analysis with a recent result from CDF Note 10154. The results of this analysis are shown with thick error bars.

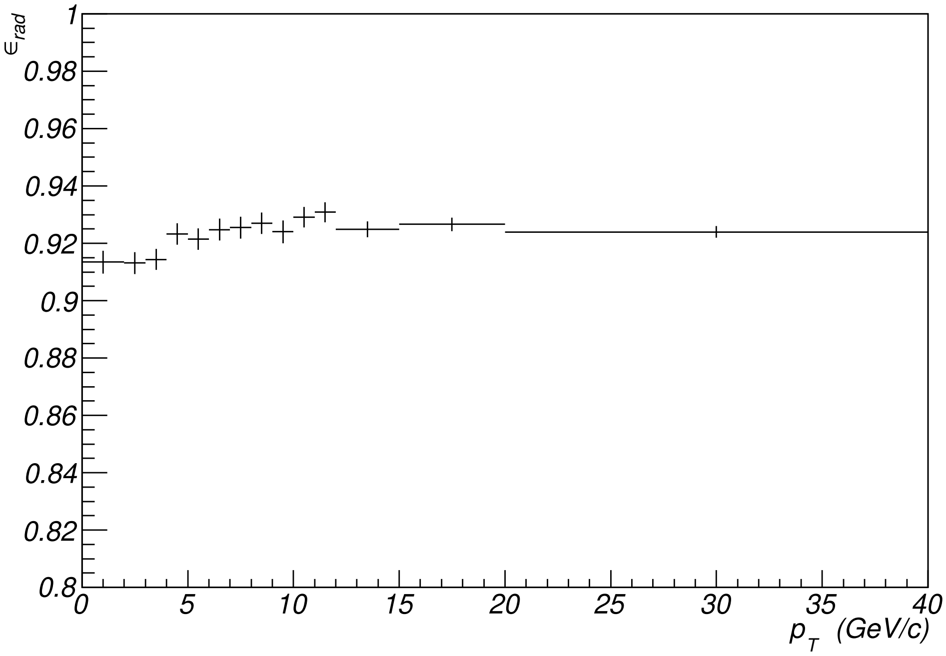

Figure 67: Ratio of fitted Gaussian area to the total number of reconstructed simulated $\Upsilon(1S)$ decays as a funciton of p_T. This ratio is used to correct the fitted cross section for the bias introduced when fitting the $\Upsilon(nS)$ signals with a single Gaussian function.

8 Differential Cross Section

Given the effective integrated luminosity, the fit determines the $\Upsilon(nS)$ production cross sections, corrected for detector acceptance, efficiency and polarization. This "raw" cross section includes the parameterized efficiencies that depend on muon p_T since these are applied to the Monte Carlo samples. The final cross section measurement scales these raw values by factors that are independent of p_T. These include the muon scale factors from Equation 15, the vertex cut efficiency from Equation 17 and a correction for final state radiation which is described below.

The cross section parameter in the fit is scaled by the fraction of the $\Upsilon(nS)$ signal that lies within the selected range of masses. This fraction is determined from the Gaussian fit to the di-muon invariant mass distribution described in Section 6.2. However, final state radiation will introduce a tail on the signal peaks that extends to lower masses. To evaluate the bias introduced by fitting the asymmetric line shape to a single Gaussian, a single Gaussian fit was applied to the the Monte Carlo sample of $\Upsilon(1S)$ decays, which was generated using PHOTOS to simulate final state radiation. Figure 67 shows the ratio of the yield determined from the single Gaussian fit to the total number of reconstructed Monte Carlo $\Upsilon(1S)$ decays in the CMUP+CMU trigger path.

An average radiation correction factor is found by fitting a constant function to the data in Figure 67 which yields $\bar{\epsilon}_{\rm rad} = 0.923 \pm 0.001$. The total correction factor applied to the raw fitted cross sections is then

$$\begin{aligned} \epsilon_{CMU} &= (S_{CMU}(\mu))^2 \cdot \epsilon_{\rm vtx} \cdot \bar{\epsilon}_{\rm rad} \\ &= 0.889^{+0.009}_{-0.014} \end{aligned} \tag{47}$$

Figure 68 shows the differential production cross sections times branching fraction for the three

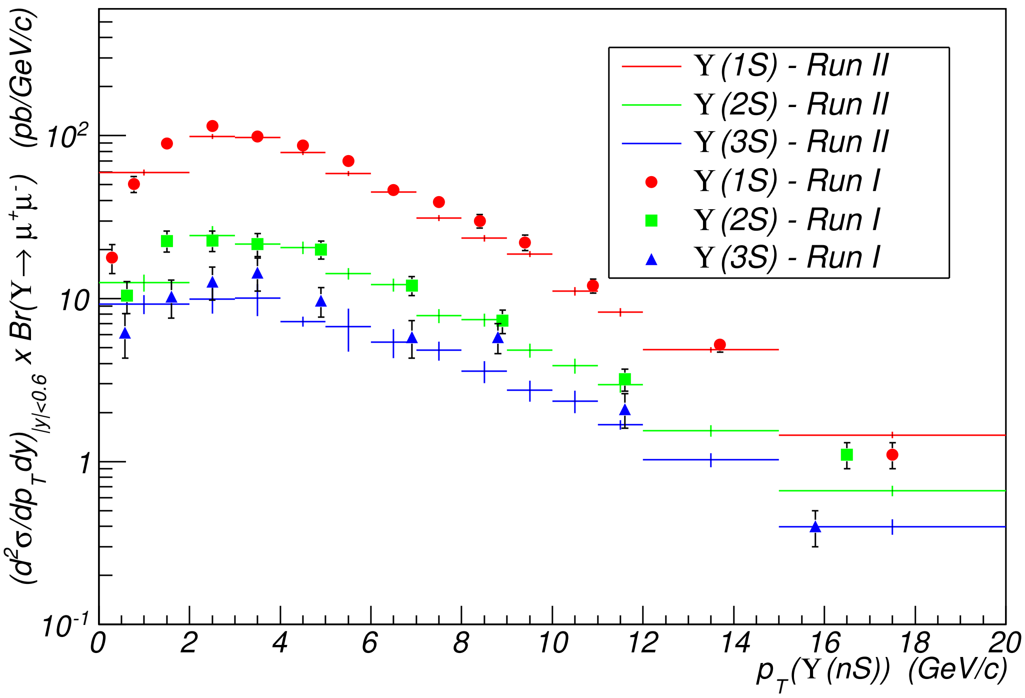

Figure 68: Differential production cross section times branching fraction as a function of p_T for the three $\Upsilon(nS)$ states, compared with previous measurements from Run I.

$\Upsilon(nS)$ states, compared with previously published results from Run I. There is generally good agreement, although the average cross section measured in Run II appears lower than in Run I by approximately 10%. Although the studies described in Section 5 found no evidence for time dependence in the trigger and reconstruction efficiency, time dependence has been observed in the high-statistics J/ψ yield in the `JPSI_CMUCMU1.5` and `JPSI_CMU1.5_CMX2` trigger paths. Figure 69 shows the fitted J/ψ yields divided by the equivalent integrated luminosity, plotted as a function of time in bins of approximately equal integrated luminosity. This figure can be compared with Figure 70 which shows the fitted $\Upsilon(1S)$ yield divided by the equivalent integrated luminosity, plotted as a fucntion of time.

9 Summary

This analysis is the first to have measured simultaneously the three parameters that characterize the angular distribution of $\Upsilon \to \mu^+\mu^-$ decays, described in Equation 2. The fitting method is simple and relies on few assumptions. Most important, this analysis is the first to provide information that can be used to perform internal checks on the consistency of the results. In particular, this analysis is the first to measure the angular invariant quantity $\tilde{\lambda}$ in both the Collins-Soper and the S-channel helicity frame. The level of agreement suggests bounds that could be placed on additional systematic uncertainties on the fitted parameters. The precision of the result is limited primarily by the available statistics, but is sufficient to demonstrate that no strong polarization is present, even at high p_T. However, one might interpret the data as suggesting that there is a trend towards slightly longitudinal polarization in the S-channel helicity frame at moderate values of p_T.

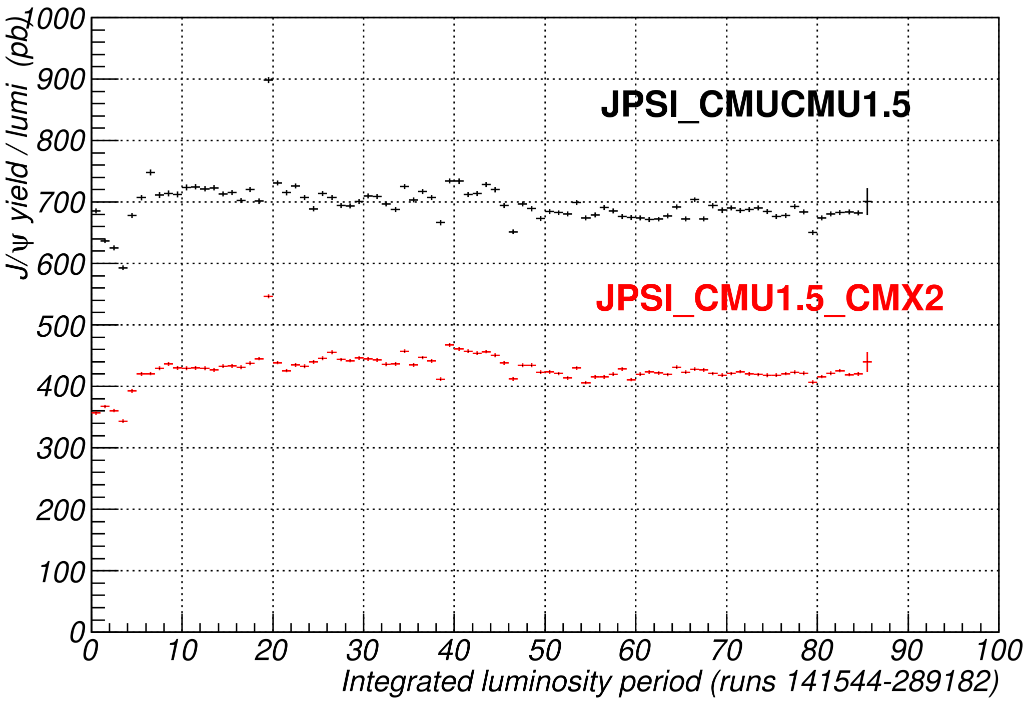

Figure 69: Fitted J/ψ yield divided by equivalent integrated luminosity as a function of time.

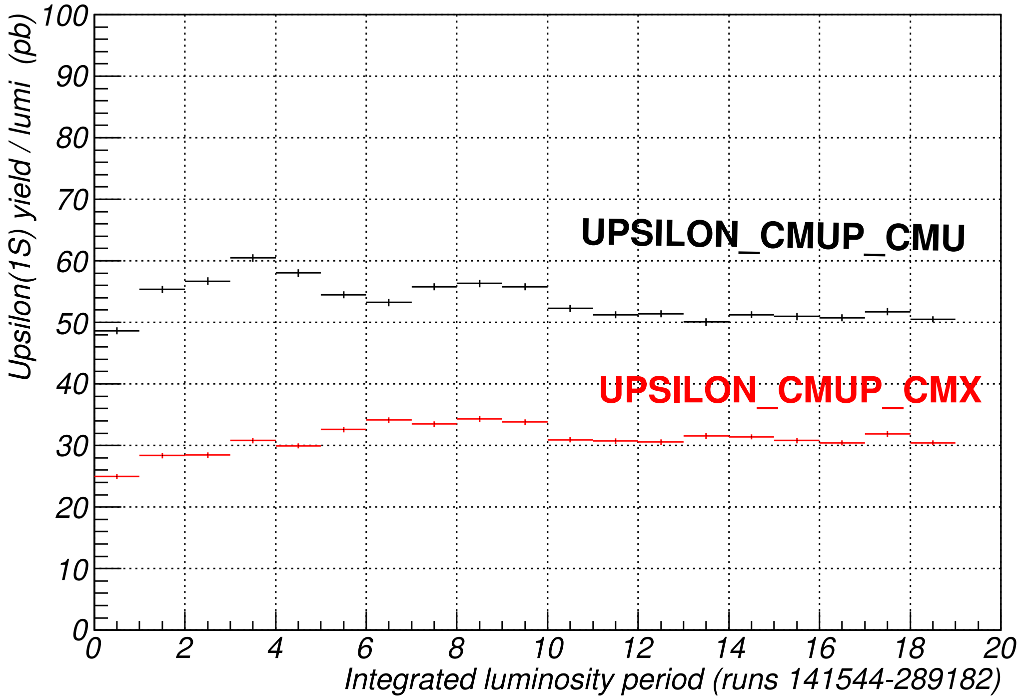

Figure 70: Fitted $\Upsilon(1S)$ yield divided by equivalent integrated luminosity as a function of time.

Appendix A Tables of fitted parameters

$\Upsilon(1S)$ — Collins-Soper frame			
p_T [GeV/c]	λ_θ	λ_φ	$\lambda_{\theta\varphi}$
0-2	$0.1265 \pm 0.1594 \pm 0.0156$	$-0.0437 \pm 0.0902 \pm 0.0467$	$0.0103 \pm 0.0598 \pm 0.0051$
2-3	$-0.0631 \pm 0.1218 \pm 0.0063$	$-0.0627 \pm 0.0573 \pm 0.0174$	$0.0267 \pm 0.0396 \pm 0.0052$
3-4	$-0.0295 \pm 0.1104 \pm 0.0198$	$-0.0721 \pm 0.0538 \pm 0.0547$	$-0.0209 \pm 0.0404 \pm 0.0169$
4-5	$-0.0672 \pm 0.1117 \pm 0.0213$	$-0.1242 \pm 0.0525 \pm 0.0556$	$-0.0206 \pm 0.0463 \pm 0.0116$
5-6	$-0.2308 \pm 0.1057 \pm 0.0240$	$-0.1265 \pm 0.0412 \pm 0.0589$	$0.1265 \pm 0.0519 \pm 0.0409$
6-7	$0.0242 \pm 0.1181 \pm 0.0150$	$-0.1312 \pm 0.0612 \pm 0.0401$	$-0.0511 \pm 0.0608 \pm 0.0060$
7-8	$0.0193 \pm 0.1214 \pm 0.0046$	$-0.2046 \pm 0.0633 \pm 0.0117$	$-0.0364 \pm 0.0683 \pm 0.0006$
8-9	$0.0281 \pm 0.0927 \pm 0.0081$	$-0.1107 \pm 0.0480 \pm 0.0221$	$0.0395 \pm 0.0518 \pm 0.0290$
9-10	$0.0697 \pm 0.1064 \pm 0.0023$	$0.0037 \pm 0.0570 \pm 0.0071$	$-0.1234 \pm 0.0488 \pm 0.0089$
10-11	$0.0337 \pm 0.1216 \pm 0.0008$	$-0.2674 \pm 0.0671 \pm 0.0019$	$-0.0783 \pm 0.0605 \pm 0.0012$
11-12	$0.0660 \pm 0.1486 \pm 0.0010$	$-0.3086 \pm 0.0848 \pm 0.0024$	$0.2545 \pm 0.0994 \pm 0.0023$
12-15	$0.0653 \pm 0.0825 \pm 0.0035$	$-0.0389 \pm 0.0442 \pm 0.0104$	$0.0917 \pm 0.0553 \pm 0.0187$
15-20	$-0.0422 \pm 0.0851 \pm 0.0037$	$-0.0878 \pm 0.0418 \pm 0.0101$	$-0.0183 \pm 0.0559 \pm 0.0268$
20-40	$0.0223 \pm 0.1635 \pm 0.0187$	$-0.0839 \pm 0.0851 \pm 0.0520$	$0.0993 \pm 0.0980 \pm 0.1099$

Table 5: Fitted parameters for the $\Upsilon(1S)$ angular distribution measured in the Collins-Soper frame. The first error is statistical and the second is the systematic uncertainty derived from the variation in $\tilde{\lambda}$ measured in different reference frames.

$\Upsilon(2S)$ — Collins-Soper frame			
p_T [GeV/c]	λ_θ	λ_φ	$\lambda_{\theta\varphi}$
0-2	$-0.7267 \pm 0.1567 \pm 0.0790$	$0.1367 \pm 0.0239 \pm 0.2081$	$0.1440 \pm 0.1208 \pm 0.0015$
2-3	$-0.1531 \pm 0.2837 \pm 0.0115$	$-0.0640 \pm 0.1219 \pm 0.0307$	$0.0366 \pm 0.0995 \pm 0.0872$
3-4	$0.0295 \pm 0.2962 \pm 0.0173$	$-0.2031 \pm 0.1551 \pm 0.0435$	$0.2707 \pm 0.1127 \pm 0.0737$
4-5	$0.0542 \pm 0.2900 \pm 0.0031$	$-0.1132 \pm 0.1553 \pm 0.0086$	$0.0303 \pm 0.1059 \pm 0.0113$
5-6	$-0.2937 \pm 0.2592 \pm 0.0302$	$-0.1925 \pm 0.0934 \pm 0.0686$	$0.1180 \pm 0.1202 \pm 0.0712$
6-7	$-0.1562 \pm 0.2556 \pm 0.0164$	$-0.1028 \pm 0.1095 \pm 0.0424$	$-0.0297 \pm 0.1259 \pm 0.0301$
7-8	$-0.4193 \pm 0.2177 \pm 0.0653$	$-0.1457 \pm 0.0653 \pm 0.1472$	$0.2039 \pm 0.1365 \pm 0.1495$
8-9	$0.1550 \pm 0.2848 \pm 0.0018$	$-0.1933 \pm 0.1676 \pm 0.0047$	$-0.0576 \pm 0.1617 \pm 0.0027$
9-10	$-0.4629 \pm 0.1936 \pm 0.0100$	$-0.1144 \pm 0.0545 \pm 0.0227$	$0.0184 \pm 0.1036 \pm 0.0086$
10-11	$0.1459 \pm 0.3006 \pm 0.0094$	$-0.1116 \pm 0.1753 \pm 0.0267$	$-0.2295 \pm 0.1735 \pm 0.0293$
11-12	$-0.1321 \pm 0.2412 \pm 0.0082$	$-0.0420 \pm 0.1062 \pm 0.0225$	$0.0816 \pm 0.1747 \pm 0.0302$
12-15	$-0.0564 \pm 0.1602 \pm 0.0007$	$-0.1941 \pm 0.0794 \pm 0.0017$	$0.1116 \pm 0.1273 \pm 0.0031$
15-20	$-0.1212 \pm 0.1304 \pm 0.0151$	$0.1723 \pm 0.0595 \pm 0.0525$	$0.0725 \pm 0.0938 \pm 0.1772$
20-40	$0.1028 \pm 0.2848 \pm 0.0141$	$-0.1496 \pm 0.1605 \pm 0.0380$	$-0.1078 \pm 0.2007 \pm 0.0912$

Table 6: Fitted parameters for the $\Upsilon(2S)$ angular distribution measured in the Collins-Soper frame. The first error is statistical and the second is the systematic uncertainty derived from the variation in $\tilde{\lambda}$ measured in different reference frames.

$\Upsilon(3S)$ — Collins-Soper frame			
p_T [GeV/c]	λ_θ	λ_φ	$\lambda_{\theta\varphi}$
0-2	$0.1024 \pm 0.4701 \pm 0.0259$	$0.4455 \pm 0.2684 \pm 0.1447$	$0.1763 \pm 0.1944 \pm 2.1683$
2-3	$-0.7434 \pm 0.4287 \pm 0.2207$	$0.0909 \pm 0.0591 \pm 0.5478$	$-0.2104 \pm 0.1605 \pm 12.6426$
3-4	$-1.0000 \pm 0.0772 \pm 0.1021$	$0.0000 \pm 0.0046 \pm 0.2042$	$0.0029 \pm 0.1467 \pm 0.2389$
4-5	$-0.7778 \pm 1.0669 \pm 0.1427$	$-0.0666 \pm 0.0783 \pm 0.2974$	$0.2200 \pm 0.1763 \pm 6.2760$
5-6	$0.0346 \pm 0.4858 \pm 0.0516$	$-0.3637 \pm 0.2633 \pm 0.1148$	$0.0211 \pm 0.2317 \pm 0.3675$
6-7	$-0.3340 \pm 0.1993 \pm 0.1256$	$-0.2461 \pm 0.0677 \pm 0.2687$	$0.5671 \pm 0.1472 \pm 0.2365$
7-8	$-0.2083 \pm 0.3773 \pm 0.0447$	$-0.2755 \pm 0.1551 \pm 0.0978$	$0.1272 \pm 0.2160 \pm 0.1479$
8-9	$0.4303 \pm 0.4795 \pm 0.0385$	$-0.4408 \pm 0.3631 \pm 0.0916$	$-0.0733 \pm 0.2806 \pm 0.1263$
9-10	$-0.5350 \pm 0.3231 \pm 0.0029$	$-0.0590 \pm 0.0782 \pm 0.0068$	$0.2066 \pm 0.2156 \pm 0.0120$
10-11	$-0.5203 \pm 0.2493 \pm 0.0539$	$-0.1455 \pm 0.0656 \pm 0.1168$	$-0.0936 \pm 0.1232 \pm 0.2544$
11-12	$-0.6222 \pm 0.2435 \pm 0.0001$	$-0.1889 \pm 0.0700 \pm 0.0002$	$-0.0444 \pm 0.1290 \pm 0.0000$
12-15	$-0.2969 \pm 0.1849 \pm 0.0007$	$-0.0885 \pm 0.0673 \pm 0.0017$	$-0.0345 \pm 0.1465 \pm 0.0057$
15-20	$-0.0058 \pm 0.2444 \pm 0.0114$	$0.0345 \pm 0.1229 \pm 0.0355$	$-0.0017 \pm 0.1590 \pm 0.1161$
20-40	$-0.1381 \pm 0.2565 \pm 0.0428$	$-0.4309 \pm 0.1707 \pm 0.0856$	$-0.2183 \pm 0.1270 \pm 0.0000$

Table 7: Fitted parameters for the $\Upsilon(3S)$ angular distribution measured in the Collins-Soper frame. The first error is statistical and the second is the systematic uncertainty derived from the variation in $\tilde{\lambda}$ measured in different reference frames.

$\Upsilon(1S)$ — S-channel helicity frame			
p_T [GeV/c]	λ_θ	λ_φ	$\lambda_{\theta\varphi}$
0-2	$-0.0100 \pm 0.0637 \pm 0.0172$	$-0.0504 \pm 0.0315 \pm 0.0489$	$0.0742 \pm 0.0362 \pm 0.1517$
2-3	$-0.0373 \pm 0.0704 \pm 0.0067$	$-0.0922 \pm 0.0339 \pm 0.0181$	$-0.0718 \pm 0.0251 \pm 0.0270$
3-4	$-0.0849 \pm 0.0672 \pm 0.0228$	$-0.1165 \pm 0.0307 \pm 0.0596$	$-0.0242 \pm 0.0346 \pm 0.1273$
4-5	$-0.1474 \pm 0.0717 \pm 0.0243$	$-0.1592 \pm 0.0306 \pm 0.0598$	$0.0077 \pm 0.0359 \pm 0.1660$
5-6	$-0.2424 \pm 0.0703 \pm 0.0203$	$-0.0573 \pm 0.0266 \pm 0.0530$	$-0.0631 \pm 0.0317 \pm 0.0729$
6-7	$-0.1601 \pm 0.0518 \pm 0.0158$	$-0.1069 \pm 0.0227 \pm 0.0404$	$0.0239 \pm 0.0307 \pm 0.0071$
7-8	$-0.2305 \pm 0.1022 \pm 0.0041$	$-0.0927 \pm 0.0395 \pm 0.0105$	$-0.1425 \pm 0.0548 \pm 0.0245$
8-9	$-0.2209 \pm 0.1000 \pm 0.0079$	$-0.0428 \pm 0.0390 \pm 0.0211$	$-0.0994 \pm 0.0371 \pm 0.0455$
9-10	$0.0448 \pm 0.1316 \pm 0.0022$	$0.0196 \pm 0.0690 \pm 0.0070$	$-0.0669 \pm 0.0655 \pm 0.0089$
10-11	$-0.3316 \pm 0.1419 \pm 0.0007$	$-0.1128 \pm 0.0490 \pm 0.0017$	$-0.0727 \pm 0.0703 \pm 0.0004$
11-12	$-0.4305 \pm 0.1498 \pm 0.0009$	$-0.0991 \pm 0.0457 \pm 0.0021$	$-0.0515 \pm 0.0737 \pm 0.0019$
12-15	$-0.1137 \pm 0.1109 \pm 0.0034$	$0.0107 \pm 0.0492 \pm 0.0100$	$-0.0300 \pm 0.0453 \pm 0.0051$
15-20	$-0.1370 \pm 0.1295 \pm 0.0037$	$-0.0642 \pm 0.0569 \pm 0.0100$	$0.0425 \pm 0.0474 \pm 0.0017$
20-40	$-0.2448 \pm 0.1932 \pm 0.0198$	$-0.0447 \pm 0.0752 \pm 0.0523$	$-0.0945 \pm 0.0636 \pm 0.0453$

Table 8: Fitted parameters for the $\Upsilon(1S)$ angular distribution measured in the S-channel helicity frame. The first error is statistical and the second is the systematic uncertainty derived from the variation in $\tilde{\lambda}$ measured in different reference frames.

$\Upsilon(2S)$ — S-channel helicity frame			
p_T [GeV/c]	λ_θ	λ_φ	$\lambda_{\theta\varphi}$
0-2	$-0.3163 \pm 0.0604 \pm 0.0472$	$0.2011 \pm 0.0219 \pm 0.1586$	$-0.2239 \pm 0.1233 \pm 0.8026$
2-3	$-0.1303 \pm 0.1749 \pm 0.0127$	$-0.1090 \pm 0.0764 \pm 0.0328$	$0.0496 \pm 0.0990 \pm 0.1217$
3-4	$-0.3607 \pm 0.1490 \pm 0.0169$	$-0.0940 \pm 0.0478 \pm 0.0408$	$-0.0435 \pm 0.0835 \pm 0.2315$
4-5	$-0.1162 \pm 0.1608 \pm 0.0030$	$-0.0604 \pm 0.0713 \pm 0.0082$	$-0.1442 \pm 0.0832 \pm 0.0392$
5-6	$-0.2067 \pm 0.1782 \pm 0.0261$	$-0.1517 \pm 0.0709 \pm 0.0633$	$-0.0587 \pm 0.0914 \pm 0.3504$
6-7	$-0.0587 \pm 0.1738 \pm 0.0151$	$-0.0924 \pm 0.0819 \pm 0.0406$	$-0.1130 \pm 0.0586 \pm 0.0448$
7-8	$-0.2149 \pm 0.1964 \pm 0.0479$	$-0.0717 \pm 0.0776 \pm 0.1244$	$-0.0913 \pm 0.0650 \pm 0.1866$
8-9	$-0.3319 \pm 0.1623 \pm 0.0015$	$-0.0046 \pm 0.0545 \pm 0.0039$	$-0.1850 \pm 0.0771 \pm 0.0297$
9-10	$-0.0219 \pm 0.2397 \pm 0.0110$	$-0.2770 \pm 0.1177 \pm 0.0256$	$0.2040 \pm 0.0959 \pm 0.0043$
10-11	$-0.0604 \pm 0.2824 \pm 0.0082$	$-0.0113 \pm 0.1345 \pm 0.0238$	$-0.1931 \pm 0.1444 \pm 0.0400$
11-12	$-0.1369 \pm 0.1669 \pm 0.0087$	$-0.0664 \pm 0.0717 \pm 0.0235$	$0.1398 \pm 0.0977 \pm 0.0910$
12-15	$-0.2367 \pm 0.1975 \pm 0.0007$	$-0.1228 \pm 0.0754 \pm 0.0016$	$0.0497 \pm 0.0575 \pm 0.0005$
15-20	$0.2295 \pm 0.1423 \pm 0.0207$	$0.0030 \pm 0.0878 \pm 0.0671$	$-0.1018 \pm 0.0588 \pm 0.0570$
20-40	$-0.3949 \pm 0.2145 \pm 0.0131$	$-0.0029 \pm 0.0655 \pm 0.0341$	$-0.0808 \pm 0.1440 \pm 0.0367$

Table 9: Fitted parameters for the $\Upsilon(2S)$ angular distribution measured in the S-channel helicity frame. The first error is statistical and the second is the systematic uncertainty derived from the variation in $\tilde{\lambda}$ measured in different reference frames.

$\Upsilon(3S)$ — S-channel helicity frame			
p_T [GeV/c]	λ_θ	λ_φ	$\lambda_{\theta\varphi}$
0-2	$0.3601 \pm 0.0796 \pm 0.0139$	$0.5269 \pm 0.0558 \pm 0.0984$	$0.5083 \pm 0.1378 \pm 0.7746$
2-3	$0.8611 \pm 0.3280 \pm 0.0845$	$0.0852 \pm 0.3318 \pm 0.3568$	$0.1172 \pm 0.1893 \pm 1.0409$
3-4	$-0.4618 \pm 0.2896 \pm 0.0707$	$-0.0110 \pm 0.0794 \pm 0.1774$	$-0.0478 \pm 0.1321 \pm 2.8887$
4-5	$-0.0782 \pm 0.3469 \pm 0.0845$	$-0.0442 \pm 0.1633 \pm 0.2365$	$0.0871 \pm 0.1625 \pm 2.1184$
5-6	$-0.1459 \pm 0.3359 \pm 0.0643$	$-0.4270 \pm 0.1463 \pm 0.1286$	$-0.0737 \pm 0.1382 \pm 0.0001$
6-7	$-0.7015 \pm 0.1289 \pm 0.0576$	$0.1492 \pm 0.0244 \pm 0.1557$	$-0.0428 \pm 0.1198 \pm 0.0073$
7-8	$-0.4805 \pm 0.2697 \pm 0.0318$	$-0.0535 \pm 0.0711 \pm 0.0760$	$0.2317 \pm 0.1548 \pm 1.0058$
8-9	$-0.4369 \pm 0.3097 \pm 0.0354$	$-0.1637 \pm 0.0897 \pm 0.0780$	$-0.0202 \pm 0.1986 \pm 0.2863$
9-10	$-0.0272 \pm 0.3859 \pm 0.0035$	$-0.2675 \pm 0.1926 \pm 0.0081$	$-0.0025 \pm 0.1390 \pm 0.0022$
10-11	$0.7887 \pm 1.4706 \pm 0.0603$	$-0.5575 \pm 0.5821 \pm 0.1467$	$0.2010 \pm 0.3132 \pm 0.3535$
11-12	$-0.1814 \pm 0.3425 \pm 0.0001$	$-0.4089 \pm 0.1448 \pm 0.0003$	$0.2295 \pm 0.1472 \pm 0.0000$
12-15	$-0.0065 \pm 0.1890 \pm 0.0008$	$-0.2077 \pm 0.0918 \pm 0.0019$	$-0.0832 \pm 0.0836 \pm 0.0034$
15-20	$-0.0611 \pm 0.1847 \pm 0.0126$	$0.0122 \pm 0.0873 \pm 0.0375$	$0.0386 \pm 0.0798 \pm 0.0033$
20-40	$-0.4459 \pm 0.2173 \pm 0.0316$	$-0.1881 \pm 0.0978 \pm 0.0680$	$0.0047 \pm 0.1774 \pm 0.0245$

Table 10: Fitted parameters for the $\Upsilon(3S)$ angular distribution measured in the S-channel helicity frame. The first error is statistical and the second is the systematic uncertainty derived from the variation in $\tilde{\lambda}$ measured in different reference frames.

p_T [GeV/c]	$\tilde{\lambda}_{CS}$	$\tilde{\lambda}_{SH}$
0-2	-0.0044 ± 0.1840	-0.1534 ± 0.0746
2-3	-0.2364 ± 0.1338	-0.2874 ± 0.0367
3-4	-0.2293 ± 0.1164	-0.3892 ± 0.0760
4-5	-0.3912 ± 0.1114	-0.5392 ± 0.0807
5-6	-0.5418 ± 0.1173	-0.3920 ± 0.0411
6-7	-0.3265 ± 0.1338	-0.4344 ± 0.0368
7-8	-0.4935 ± 0.1379	-0.4654 ± 0.1345
8-9	-0.2736 ± 0.0837	-0.3351 ± 0.0491
9-10	0.0812 ± 0.0854	0.1056 ± 0.1873
10-11	-0.6063 ± 0.0660	-0.6020 ± 0.1712
11-12	-0.6570 ± 0.1925	-0.6622 ± 0.1721
12-15	-0.0496 ± 0.1549	-0.0826 ± 0.1427
15-20	-0.2810 ± 0.1635	-0.3097 ± 0.1469
20-40	-0.2115 ± 0.2754	-0.3626 ± 0.2354

Table 11: Comparison of $\tilde{\lambda}$ calculated in the Collins-Soper frame and the S-channel helicity frame for the $\Upsilon(1S)$ state.

p_T [GeV/c]	$\tilde{\lambda}_{CS}$	$\tilde{\lambda}_{SH}$
0-2	-0.3668 ± 0.4244	0.3595 ± 0.3343
2-3	-0.3243 ± 0.2840	-0.4124 ± 0.2105
3-4	-0.4820 ± 0.2755	-0.5875 ± 0.1795
4-5	-0.2563 ± 0.2937	-0.2803 ± 0.1971
5-6	-0.7305 ± 0.2445	-0.5745 ± 0.2127
6-7	-0.4214 ± 0.2787	-0.3074 ± 0.1017
7-8	-0.7475 ± 0.2585	-0.4011 ± 0.1074
8-9	-0.3560 ± 0.3117	-0.3442 ± 0.1548
9-10	-0.7233 ± 0.2790	-0.6679 ± 0.0816
10-11	-0.1699 ± 0.4012	-0.0934 ± 0.3969
11-12	-0.2478 ± 0.4127	-0.3151 ± 0.2459
12-15	-0.5348 ± 0.2555	-0.5390 ± 0.2248
15-20	0.4780 ± 0.3767	0.2392 ± 0.1784
20-40	-0.3009 ± 0.4776	-0.4024 ± 0.2305

Table 12: Comparison of $\tilde{\lambda}$ calculated in the Collins-Soper frame and the S-channel helicity frame for the $\Upsilon(2S)$ state.

p_T [GeV/c]	$\tilde{\lambda}_{CS}$	$\tilde{\lambda}_{SH}$
0-2	2.5952 ± 4.9307	4.1019 ± 1.5139
2-3	-0.5178 ± 1.7349	1.2207 ± 0.6785
3-4	-1.0000 ± 0.0037	-0.4895 ± 0.3058
4-5	-0.9166 ± 0.2440	-0.2018 ± 0.4078
5-6	-0.7747 ± 0.4432	-1.0000 ± 0.0009
6-7	-0.8606 ± 0.1121	-0.2984 ± 0.3580
7-8	-0.8112 ± 0.3778	-0.6084 ± 0.3741
8-9	-0.6192 ± 0.4654	-0.7973 ± 0.4132
9-10	-0.6723 ± 0.4459	-0.6545 ± 0.1203
10-11	-0.8352 ± 0.1165	-0.5674 ± 0.4911
11-12	-1.0000 ± 0.0008	-0.9995 ± 0.0160
12-15	-0.5168 ± 0.3289	-0.5214 ± 0.1431
15-20	0.1011 ± 0.4756	-0.0247 ± 0.3774
20-40	-1.0000 ± 0.0016	-0.8504 ± 0.1424

Table 13: Comparison of $\tilde{\lambda}$ calculated in the Collins-Soper frame and the S-channel helicity frame for the $\Upsilon(3S)$ state.

Appendix B CMP efficiency fits

The CMP efficiency is parametrized as a function of $1/p_T$ and the run range. The efficiency is parameterized separately in east and west ends of the chambers, but is otherwise treated as being constant, even though there is some evidence that the efficiency is slightly position dependent in some chambers. It is natural to assume that the p_T distribution of muons is not correlated to the run range, so the efficiency parametrization is factored into the form

$$\epsilon_i(1/p_T, R) = \bar{\epsilon}_i(1/p_T)\frac{\bar{\epsilon}'_i(R)}{\langle\epsilon'_i(R)\rangle} \tag{48}$$

where $\bar{\epsilon}_i(1/p_T)$ is the efficiency in region i as a function of $1/p_T$, averaged over the range of runs and other term scales this p_T dependent efficiency by the ratio of the efficiency in the particular run range by the run-averaged efficiency.

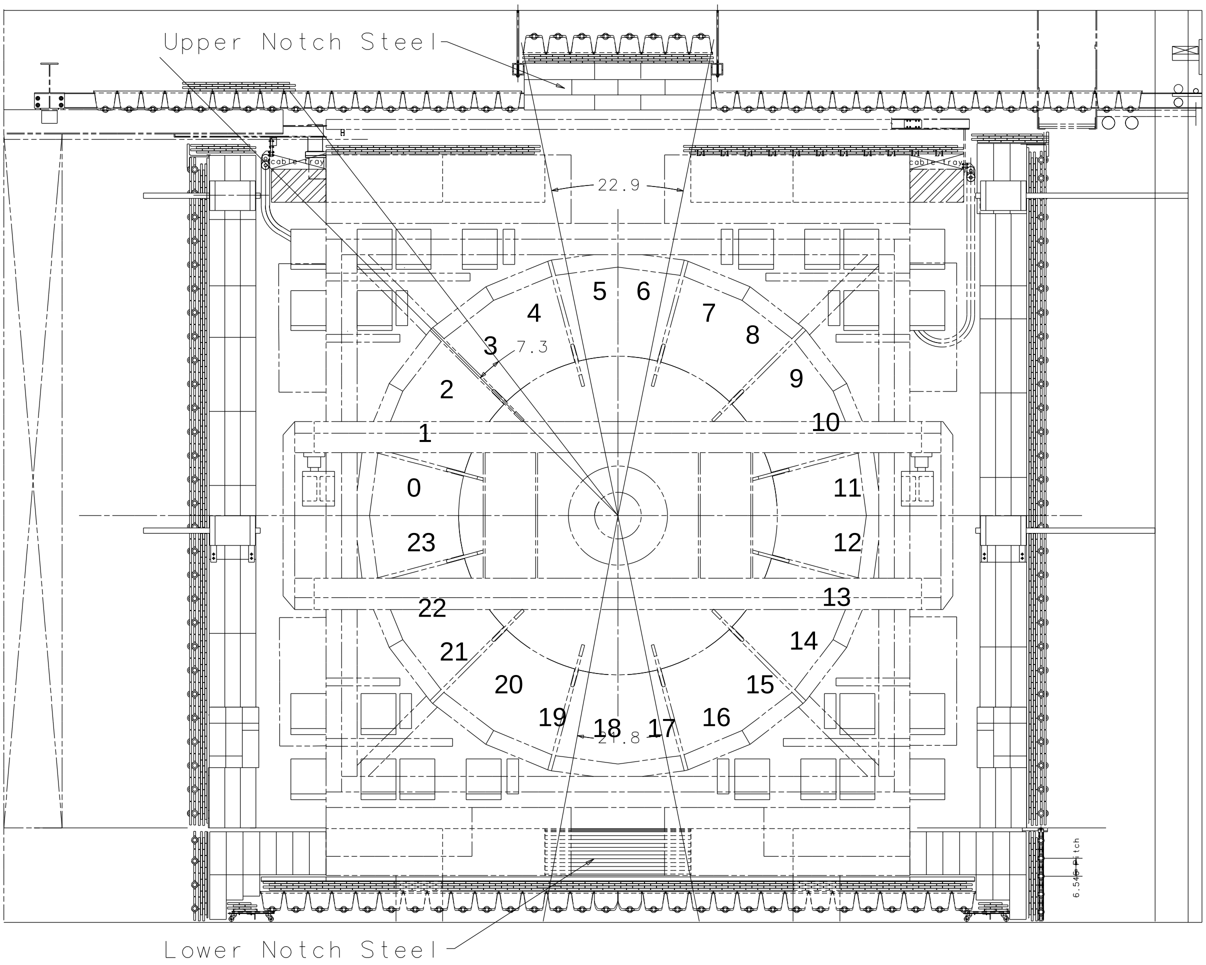

Figure 71: CMP geometry described in the technical design report.

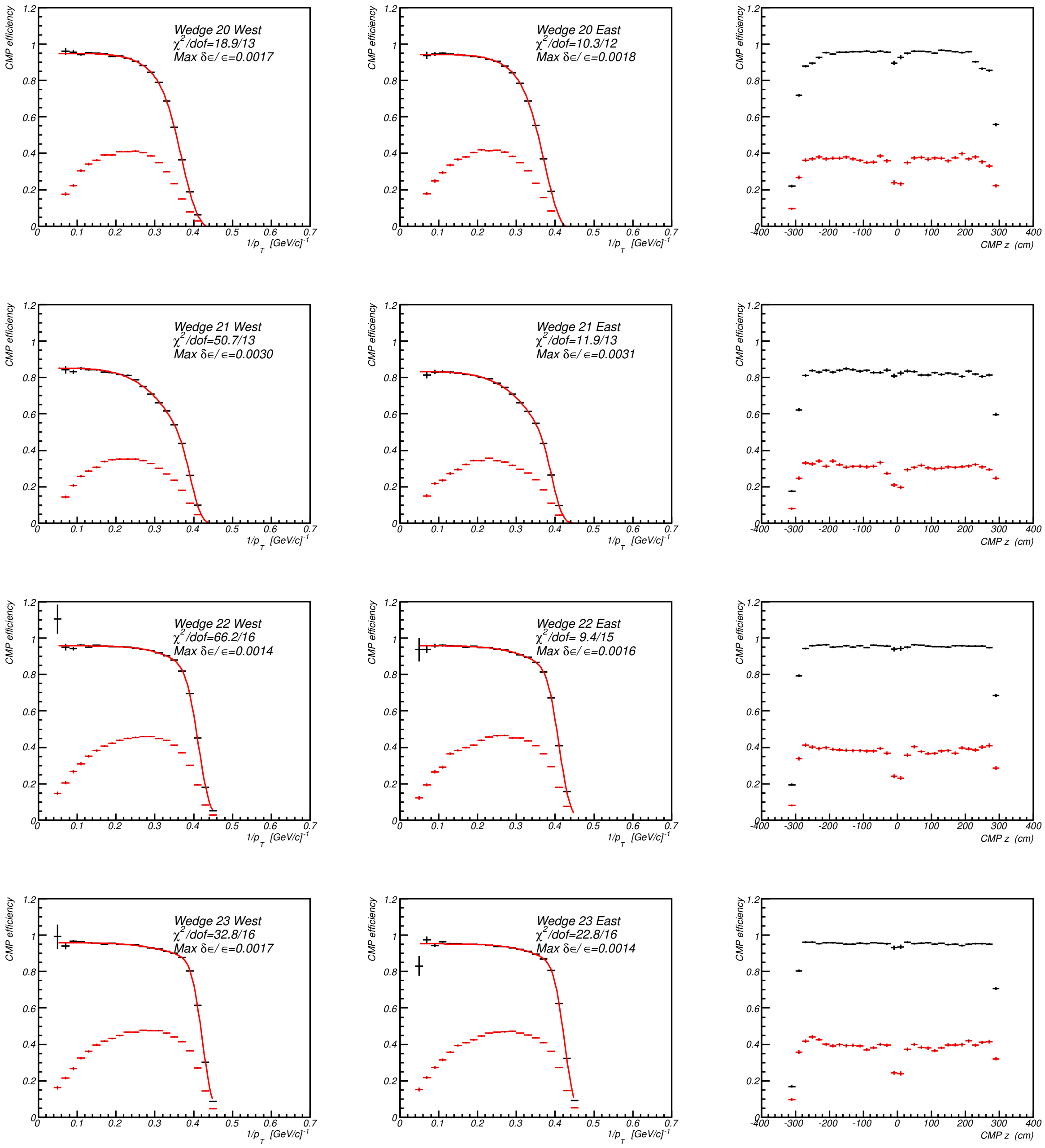

Figure 72: CMP efficiency fits - wedges 0-3. Black points are obtained from the ratio of J/ψ yields, red points are from the ratio of background level in the di-muon mass distributions.

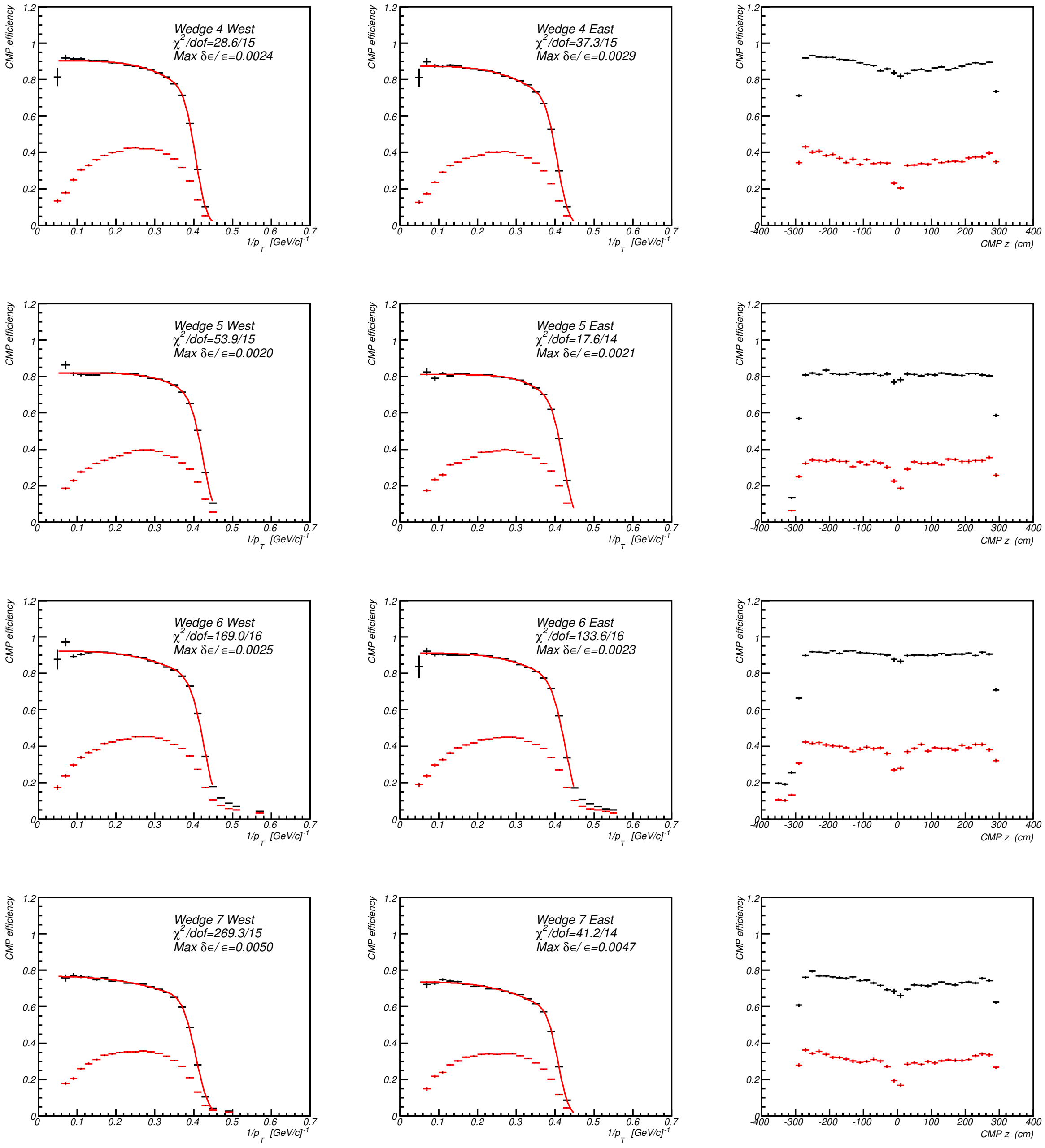

Figure 73: CMP efficiency fits - wedges 4-7.

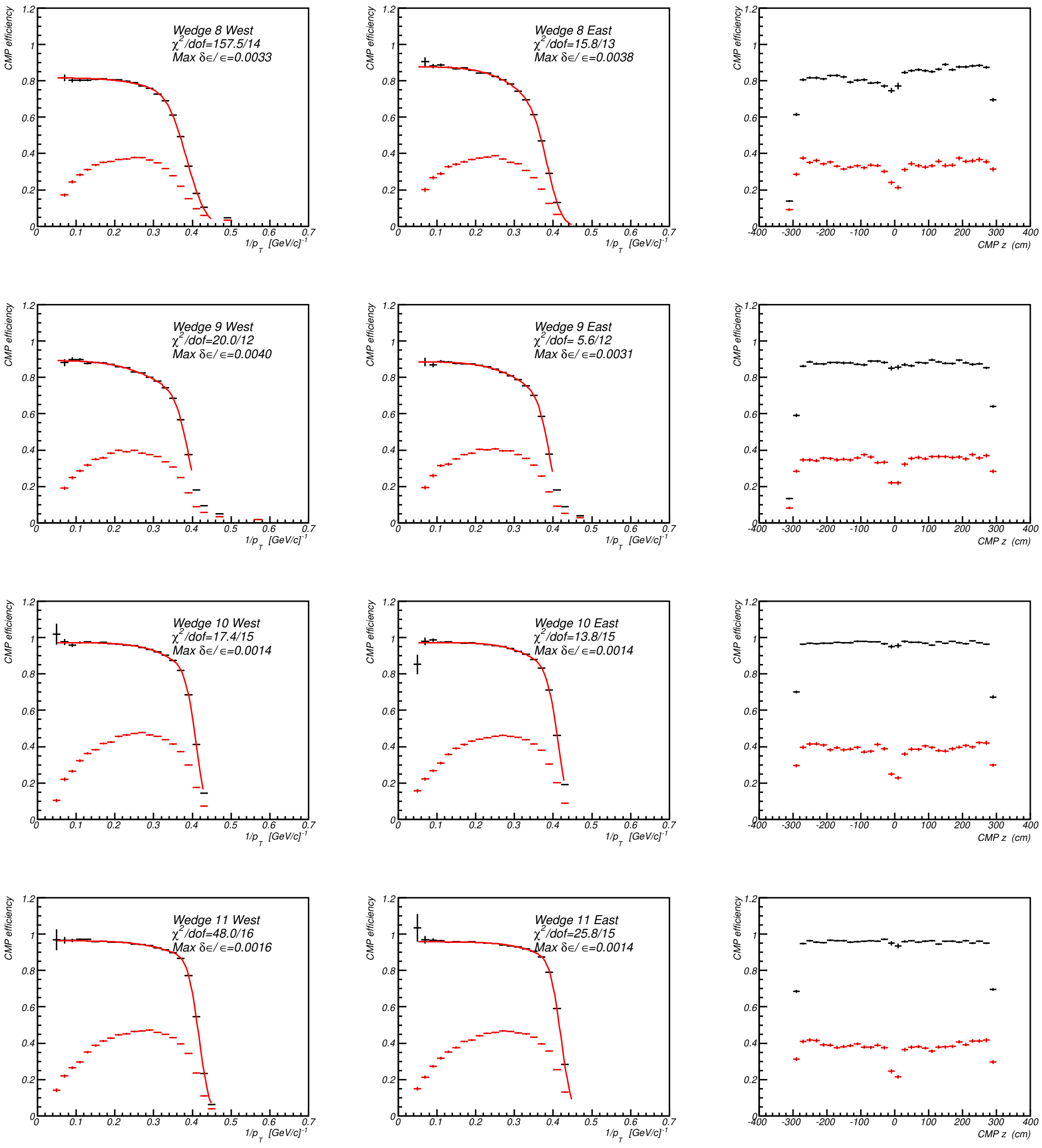

Figure 74: CMP efficiency fits - wedges 8-11.

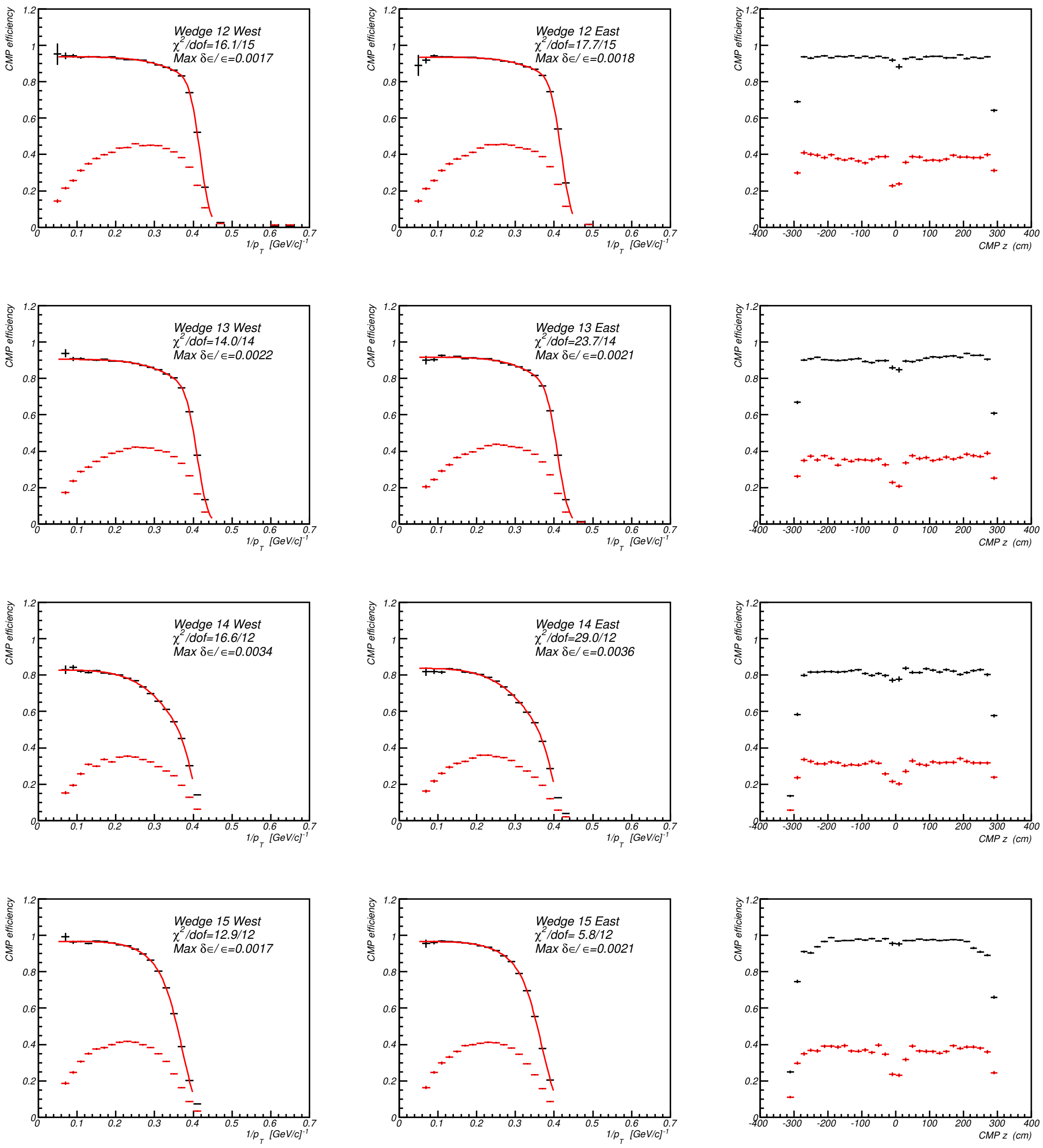

Figure 75: CMP efficiency fits - wedges 12-15.

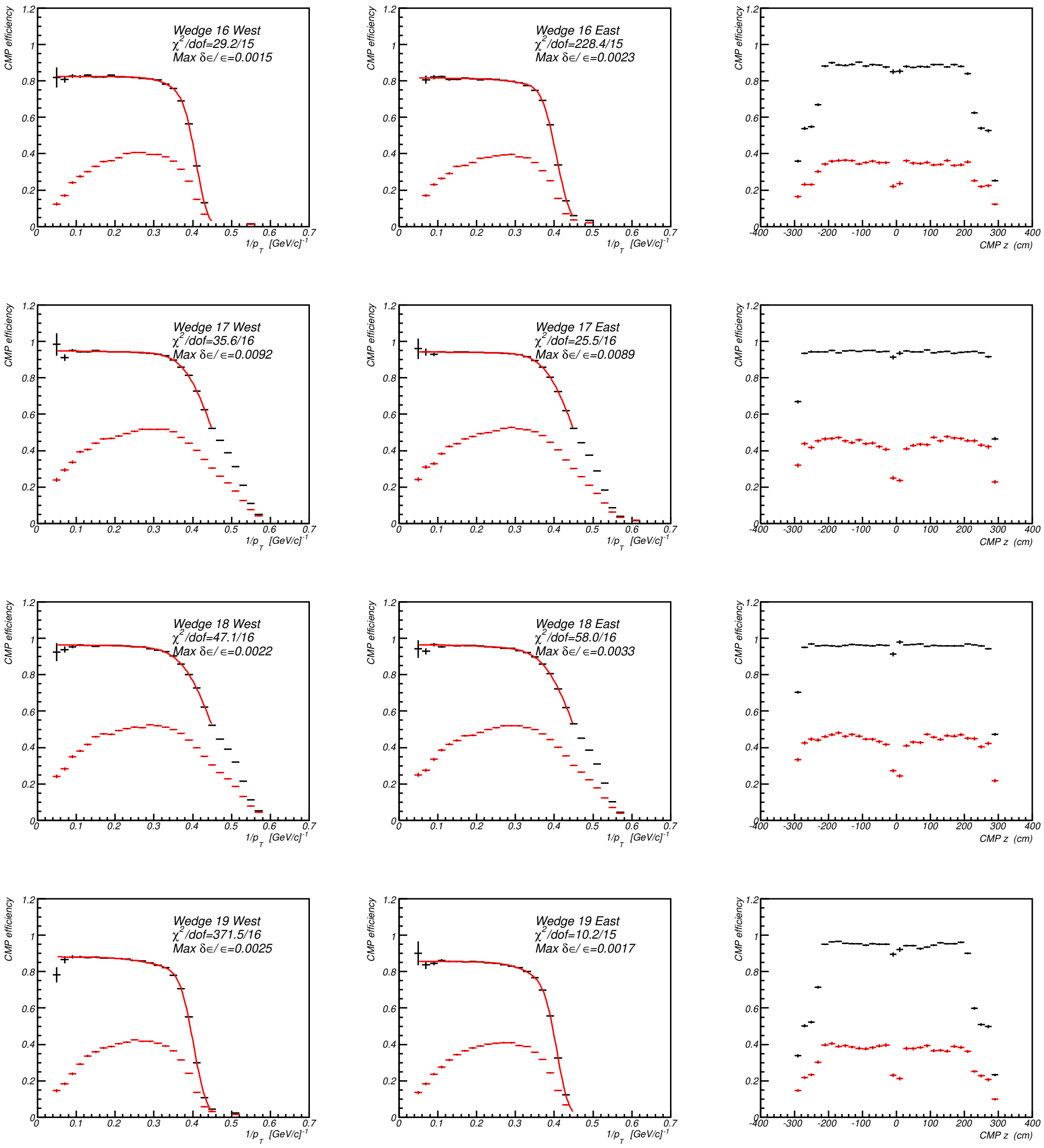

Figure 76: CMP efficiency fits - wedges 16-19.

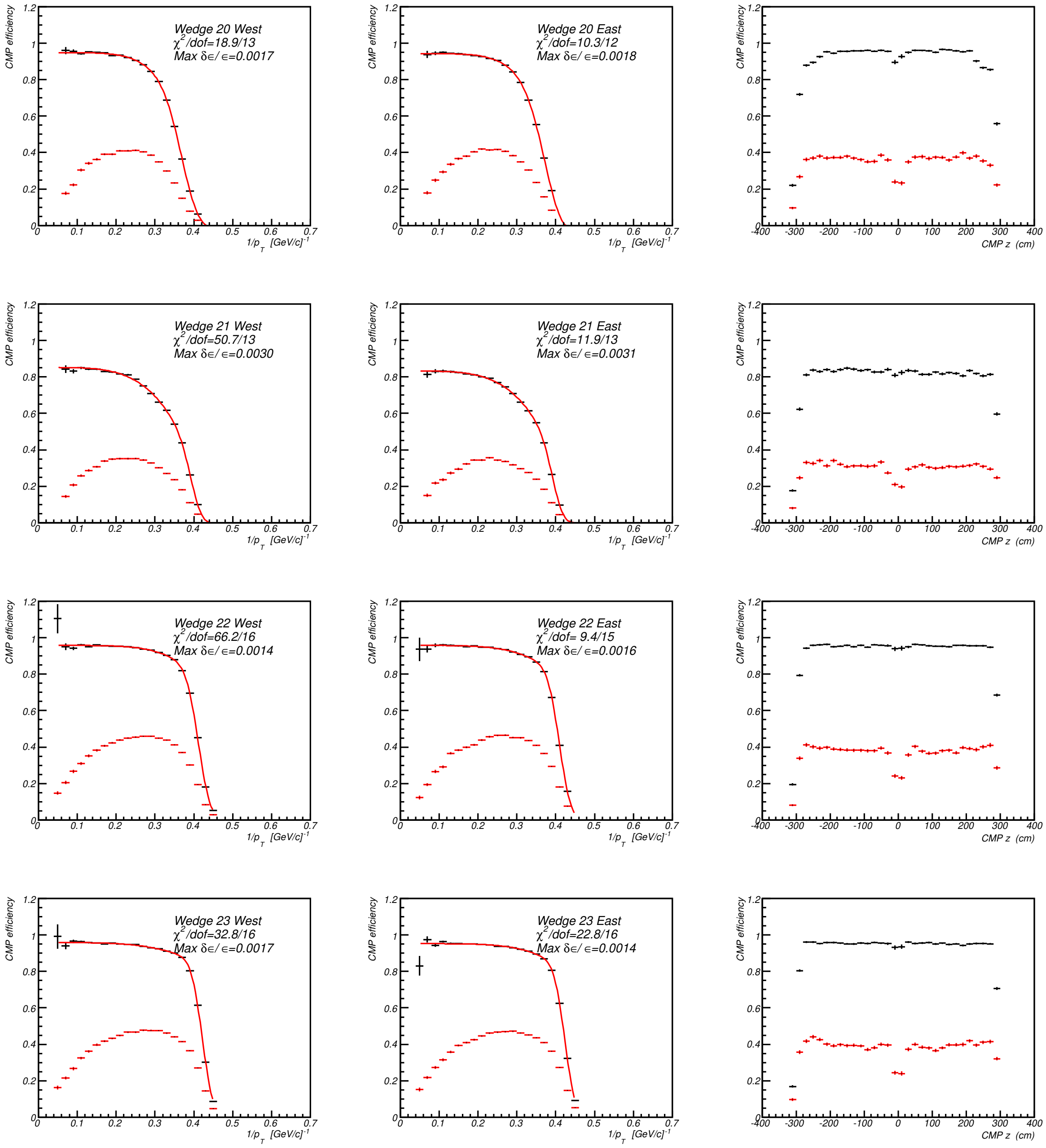

Figure 77: CMP efficiency fits - wedges 20-23.

References

[1] D. Glenzinski, *et al.*, *Measurement of Level 1, 2 and 3 low p_T dimuon efficiencies for the $B_s \to \mu\mu$ analysis*, CDF Note 7314, ver 4.4, July 18, 2008.

[2] K. Nakamura, *et al.* (Particle Data Group), *The Review of Particle Properties*, J. Phys. G **37**, 075021 (2010).

[3] M. Jones, *Determination of Polarization Parameters in Decays of Heavy Quarkonium*, CDF Note 10385, January 24, 2011.

[4] C. Chen, *et al.*, *Measurement of the Track Reconstruction Efficiency in the Central Outer Tracker Using a Monte Carlo Track Embedding Technique*, CDF Note 6394, version 4.0, October 28, 2003.

[5] V. Drollinger, *et al.*, *Identification of soft Muons with a χ^2 based Track Stub Matching Procedure*, CDF Note 6201, January 29, 2003.

[6] W.K. Sakumoto, *Event $Z_{\rm vtx} \leq 60$ cm Cut Acceptance for Run II*, CDF Note 7935, November 11, 2005.

[7] R.-S. Lu, *et al.*, *Search for η_b at CDF*, CDF Note 8289, June 22, 2006.

[8] R.D. Field, *The sources of b-quarks at the Tevatron and their Correlations*, Phys. Rev. **D65**, 094006 (2002).

[9] J. Thome and J. Russ, *Template for CDF Public Note*, CDF Note 9966, October 28, 2009.

[10] J. Thome and J. Russ, *A Measurement of the $\Upsilon(1S)$, $\Upsilon(2S)$ and $\Upsilon(3S)$ Spin Alignment at CDF*, CDF Note 10154, draft 1.3, August 8, 2011.